COMPUTATIONAL STUDIES OF LIPID AUTOXIDATION AND SOLVENT-MEDIATED ANTIOXIDANT ACTIVITY
AND
A KINETIC STUDY OF A HALOGENASE IN THE PYRROLNITRIN BIOSYNTHETIC PATHWAY

by

Di Hu

A thesis submitted to the Department of Chemistry

In conformity with the requirements for

the degree of Master of Science

Queen's University

Kingston, Ontario, Canada

(February, 2010)

Abstract

Chapter 1

Hydrocarbon autoxidation, a free radical chain reaction, is believed to play a key role in the onset and developments of most degenerative diseases and disorders. The two propagating steps: 1) H-atom abstraction from the hydrocarbon by a hydrocarbon-derived peroxyl radical, and 2) addition of oxygen to the resultant alkyl radical to form a new peroxyl, play a role in determining the rate of hydrocarbon autoxidation, as well as the regio- and stereochemistry of the product hydroperoxides. In the current study, we carried out a set of calculations to provide a detailed framework for understanding the mechanism of the first two steps of autoxidation.

Chapter 2

Radical-trapping chain-breaking antioxidants inhibit hydrocarbon autoxidation. Phenols are the prototypical radical-trapping antioxidants and are employed in nature, as well as in industry, to inhibit the autoxidation of hydrocarbons. The mechanism of inhibiting radical chain propagation has recently been suggested to be a PCET on the basis of theoretical calculations. It has been demonstrated that the antioxidant activitiy of phenols is increased in the presence of either protic acids or alcohols, but the basis of this acceleration is not well understood. In the current study, we used computational methods to investigate the effects of acids and alcohols on the PCET pathway for the reaction of phenol with a peroxyl radical.

Chapter 3

The antibiotic pyrrolnitrin [3-chloro-4-(2’-nitro-3’-chlorophenyl) pyrrole] (PRN) is biosynthesized from L-tryptophan in four steps, catalyzed by the enzymes PrnA, B, C and D encoded by the *prn* operon. Two of the four gene products, PrnA and PrnC, are flavin-dependent halogenases, a recently discovered and highly interesting class of enzymatic halogenation catalysts. Their activities have never been unequivocally demonstrated by reconstitution of the activity from a recombinant protein. Herein, we report the results of our efforts to clone the genes encoding PrnA and PrnC, and overexpress, isolate and purify the proteins from *E. coli*. We were able to successfully reconsistute halogenation activity of both and have obtained the first kinetic data for PrnC, which shows kinetics similar to other flavin-dependent halogenases, along with substrate inhibition.

Acknowledgements

First and foremost, I would like to thank Dr. Derek Pratt, my supervisor for the past two years for being a knowledgeable, fun and extremely helpful advisor with the deepest respect. Dr. Pratt's enthusiasm for science, chemistry in particular, helped to motivate and focus me, and everyone in the lab, to try as hard as they can to reach their goals for the projects at hand. Being a very meticulous and hard working scientist, he is a gifted exemplar for me to look up to. Personally, I have to thank him for the consistent support and understanding while I went through some exceptionally difficult and frustrating times in life.

I would also like to thank Dr. David Zechel for providing useful suggestions to the experiments, the encouragement he gave me over the two years and his kindness for reading my thesis in such a short time. I have to thank all the members from the Zechel lab and Pratt lab: Dr. Anupam Bhattacharya, Shumei He, Katie Groom, Meagan Perry, Ryan Laimer, Fern McSorley, Dr. Daria Trofimova, Jason Hanthorn, Johan Brinkhorst, Rami Dhanoa, Matthew Morrison, Susheel Nara, Mukund Jha, Vipraja Vaidya, Alaina McGrath, Graham Garrett, Alex Yang and Phil Lyett. Thank you all for the friendship, the fun times and the "true western life style" I was able to experience. This is definitely a memorable two years of my life.

A thank you also goes to my dearest family. Thank you, dad, for being so strong for me and supportive over the hard time. I am very proud of you. Thank you, Aunt Mona, for treating me as your own daughter. You always make me feel like being at home whenever I visit. I really appreciate everything you have done for me.

The best saves to the last, I would like to thank my mom for the endless love you gave me. You were the most wonderful person I have ever seen. Your inner strength against all the unfortunate events and being so selfless while you were the person needed help the most gained all my respect. Thank you for bringing me up to the way I am now. I am so proud and fortunate to have you as my mom. Without you, there is no possible way of me achieving anything I have right now. I cannot possibly express how much I miss you. I love you.

Statement of Originality

Except the calculations relating to the allylperoxyl rearrangement, which were carried out by my supervisor, Professor Derek Pratt, I hereby certify that the rest of the work described within this thesis is my original work. Any published (or unpublished) ideas and/or techniques from the work of others are fully acknowledged in accordance with the standard referencing practices.

(Di Hu)

(January, 2010)

Table of Contents

List of Schemes

List of Figures

List of Tables

List of Abbreviations

ROS	reactive oxygen species
LDL	low density lipoprotein
HDL	high density lipoprotein
VLDL	very low density lipoprotein
BDE	bond dissociation enthalpy
$^1O_2$	Singlet oxygen
TS	Transition state
MP2	Second order Møller-Plesset perturbation theory
B3LYP	Becke, three-parameter, Lee-Yang-Parr
DFT	Density functional theory
CCSD(T)	Coupled cluster theory
SOMO	singly occupied molecular orbital
HOMO	highest occupied molecular orbital
U	unrestricted shell
RO	restricted open shell
ALOO	allylperoxyl radical
PDOO	pentadienylperoxyl radical
CX	complex
PCET	Proton-coupled electron transfer
HAT	H-atom transfer
SPLET	Sequential proton loss electron transfer
ArOH	Phenolic antioxidant

ArO•	Aryloxyl radical
PSII	Photosystem (II)
BHT	Butylated hydroxytoluene
AIM	Atoms in molecules
HBA	Hydrogen bond acceptor
L-Trp	L-tryptophan
PRN	Pyrrolnitrin
7-Cl-Trp	7-Chlorotryptophan
MDA	Monodechloroaminopyrrolnitrin
APRN	Aminopyrrolnitrin
5’-FDAS	5‘-Fluoro-5’-deoxyadenosine synthase
AdoMet	*S*-Adenosyl-L-methionine
5’-FDA	5’-Deoxy-5’-fluoroadenosine
CPO	Chloroperoxidase
V-CPOs	Vanadium-dependent chloroperoxidase
V-BrPOs	Vanadium-dependent bromoperoxidase
α-KG	α-Ketoglutarate
Asp	Aspartic acid
Glu	Glutamic acid
CIAP	Calf intestine alkaline phosphatase
Kan	Kanamycin
LB	Luria Bertani
IPTG	Isopropyl β-D-1-thiogalactopyranoside

CV	Column volume
SDS-PAGE	Sodium dodecyl sulfate polyacrylamide gel lectrophoresis
FPLC	Fast Performance Liquid Chromatography
5-BDPA	5-Bromo-*N*,*N*-dimethylpyrimidin-2-amine
4-DCMA	4-(*N*,*N*-Dimethylamino)cinnamaldehyde
M-M	Michaelis-Menten
SI	Substrate inhibition

Chapter 1

Introduction

1.1 Introduction of Computational Studies of the Propagation Steps of Lipid Peroxidation

1.1.1 Background and Significance

The origin of rancidity of meat, milk and other organic materials remained unknown until 1804 when Nicolas Théodore de Saussure discovered that rancidity is actually derived from the oxygen-dependent deterioration of lipids.[1] Experiments carried out by de Saussure using walnut oil clearly demonstrated that, in the presence of oxygen, the walnut oil became more viscous and delivered a bad smell over time, whereas in its absence, the walnut oil remained unchanged.[1] This process, which is very familiar now, is commonly called autoxidation, and is simply defined as oxidation by oxygen gas at normal temperature and pressure. At the beginning of the 20th century, Carl Engler and co-workers[2] found that in the absence of water, the autoxidation of hydrocarbon substrates generated substrate-derived peroxides as the primary products. The general scheme of autoxidation of substrate A by O_2 is shown below (Scheme 1.1).

$$A + O_2 \longrightarrow AO_2$$

$$AO_2 + A \longrightarrow 2AO$$

Scheme 1.1 Autoxidation of hydrocarbon substrates (A).

Autoxidation has been most extensively studied on olefins, dating back to the early 1900s,[3, 4] but it was not until the 1940's that Bateman and Bolland at the British Rubber Producers Research Association first carried out carefully-controlled studies of hydrocarbon autoxidation. The initial motivation of this study was to understand the degradation process of natural compounds, such as rubber, waxes and other lipids.[5-8] Within their study, the role of radicals in the autoxidation process was recognized and this discovery led to the general mechanism that accounts for the experimental findings (Scheme 1.2).[5-8] This autoxidation mechanism is believed to be able to explain the oxidative degradation of rubber, oil, fuels, polymers and other organic substance.

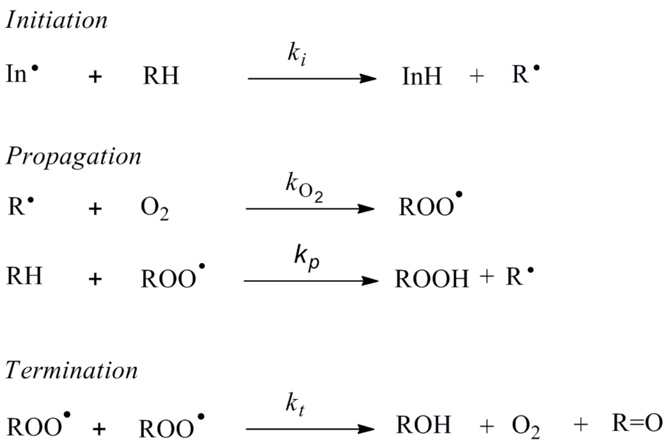

Scheme 1.2 Hydrocarbon autoxidation, a radical chain reaction.

The general mechanism for hydrocarbon autoxidation, as well as for other radical chain reactions, has three steps: initiation, propagation and termination. In the initiation step, a substrate-derived alkyl radical (R•) is generated via H-atom abstraction from the substrate by an initiating radical (In•), which can be generated thermally or photochemically from various sources, such as diazo compounds or peroxides. The propagation stage of the sequence involves two chemical steps. The first step is the addition of molecular oxygen (O_2) to the substrate-derived radical (R•) to form a peroxyl radical (ROO•). The second step involves the reaction of a peroxyl radical (ROO•) with another hydrocarbon substrate (RH) to form a hydroperoxide (ROOH) and another alkyl radical (R•). Thus, the alkyl radical and peroxyl radical are the chain-carrying radicals. Since the reaction of O_2 with alkyl radicals occurs at or very close to the diffusion-controlled limit,[9, 10] the kinetics for chain propagation (and propagation rate constant k_p) reflect the rate of H-atom abstraction from the substrate by the substrate-derived peroxyl radical. The chain reaction is terminated when two substrate-derived peroxyl radicals react with each other to give non-radical products (generally carbonyl compounds and alcohols) according to the termination reaction (Scheme 1.2), the so-called Russell termination reaction.[11, 12]

Lipid peroxidation is the autoxidation of biological lipids, such as fatty acids and steroids. Lipids are generally grouped into three categories depending on the number of double bonds in the hydrocarbon chain: saturated, monounsaturated and polyunsaturated. As shown in Scheme 1.3, stearic and palmitic acids are examples of saturated lipids because they contain the maximum number of hydrogens and have no double bond. Saturated lipids are usually solid fat at room temperature because they are linear and easy to pack. Cholesterol and oleic acid are monounsaturated lipids because they contain one double bond. Linoleic and arachadonic acids are polyunsaturated lipids as they have multiple double bonds in the structures. The *cis* geometries of the double bonds of unsaturated lipids tend to make their molecular structures non-linear and therefore they usually appear as oils at room temperature.

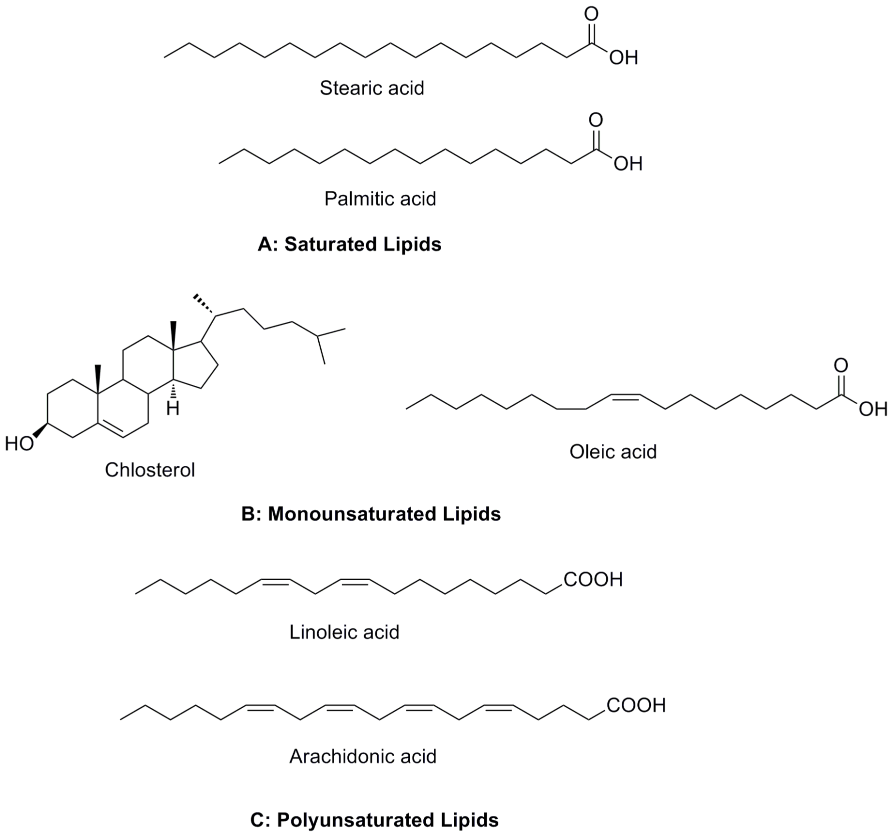

Scheme 1.3 Examples of saturated, monounsaturated and polyunsaturated lipids.

In aerobic organisms, it is normal to generate reactive oxygen species (ROS), such as $O_2^{\bullet -}$, HOO•, HO•, H_2O_2 and $^1O_2$ as part of normal metabolism, via processes like mitochondrial respiration, cyclooxygenase activation and phagocytic activity, and these ROS can initiate lipid peroxidation.[13] The primary peroxidation products, lipid hydroperoxides, are generally not directly harmful to the tissues in which they are produced. In fact, they are intermediates in the biosynthesis of important signaling molecules, e.g., prostaglandins and leukotrienes.[14] However, the further conversion of lipid hydroperoxides to carbonyl compounds can be highly detrimental to the cell.[14] In particular, α,β-unsaturated aldehydes (e.g. acrolein, malondialdehyde and 4-hydroxy-2-nonenal), which result from the oxidative cleavage of polyunsaturated lipid hydroperoxides, are highly cytotoxic. These aldehydes are good Michael acceptors and are able to react very rapidly with good nucleophiles.[15] Amines and thiols of DNA and proteins are two target nucleophiles for α,β-unsaturated aldehydes, and can result in the cross-linking of DNA and/or protein, leading to mutations, protein misfolding or aggregation (Scheme 1.4).[16]

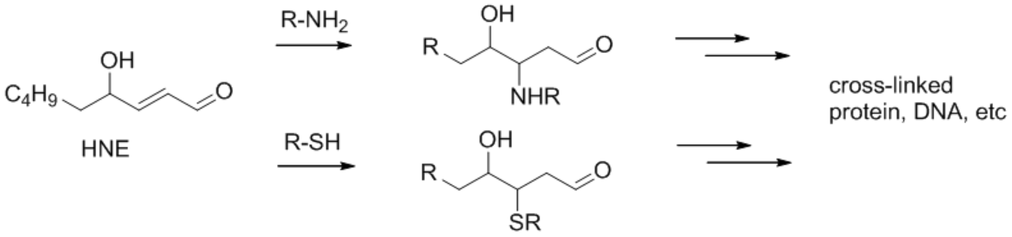

Scheme 1.4 Example of undesired reactions of biomacromolecular amines and thiols with 4-hydroxy-2-nonenal.[16]

When there is an imbalance between the formation of ROS and the ability of the cell's antioxidant systems (see Chapter 2) to neutralize them, the accumulation of lipid-derived cytoxic compounds and their reactions with biological molecules can lead to numerous degenerative diseases and disorders, including aging,[17] Alzheimer's and Parkinson's Diseases[18] and atherosclerosis.[13] Atherosclerosis, the foremost cause of death in Western Society, is believed to be initiated by the oxidation of cholesterol esterified fatty acids in the bloodstream. The characteristic morphological feature of the disease is the formation of fatty streaks on the interior walls of arteries, which progressively narrow and harden the arteries over time, leading to increased risk of heart attack and stroke.[19-22] The main components of the streaks are macrophages that are laden with peroxidized low-density lipoprotein (LDL) particles, which are known as the carriers of cholesterol.[23] Cholesterol is a steroid essential for human because it is the precursor for several hormones[13]. These hormones are required to be transported to different locations in cells. Therefore there are several types of lipoproteins, including high density lipoprotein (HDL), very low density lipoprotein (VLDL), intermediate density lipoprotein (IDL) and LDL, that are responsible for transporting cholesterol to various compartments of cells.[13] LDL is the carrier of cholesterol in blood, therefore it is known as "bad cholesterol", especially in its oxidized or partly oxidized form.[23] The LDL is particularly susceptible to oxidation owing to its high content of cholesteryl esters of two polyunsaturated fatty acids: linoleic acid (80%) and arachidonic acid (20%).[13]

1.1.2 Mechanistic Coniderations

The rate-limiting step in the propagation sequence of lipid peroxidation is H-atom abstraction from the lipid. Indeed, the main reason that makes lipids a good target for autoxidation is a weak C-H bond. The bond dissociation enthalpy (BDE) is especially low at the allylic and bis-allylic positions of mono- and polyunsaturated lipids, respectively (see above in Scheme 1.3), since upon H-atom abstraction from these positions, resonance stabilized allyl and pentadienyl radicals are formed, respectively. The greater the stability of the resultant radical species, the lower the C-H BDE is and consequently, the higher the oxidizability of the lipid (Scheme 1.5).

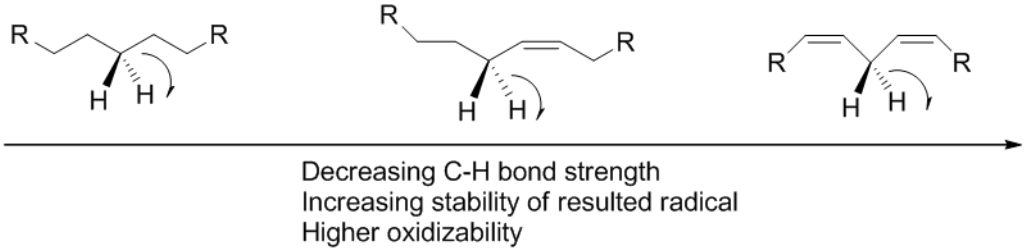

Scheme 1.5 Differing reactivities of saturated, monounsaturated and polyunsaturated lipids.

Studies have shown that the propagation rate constant (k_p) for peroxidation of saturated lipids (e.g. stearic acid and palmitic acid) is ~0.01$M^{-1}s^{-1}$, while those of monounsaturated lipids (e.g. oleic acid and cholesterol) is ~1$M^{-1}s^{-1}$,[24] and polyunsaturated lipids (e.g. linoleic and arachidonic acid) is ~60 $M^{-1}s^{-1}$.[25] The trend in these rate constants parallels that of the corresponding C-H BDEs for saturated (~98 kcal/mol),[26] monounsaturated (~82 kcal/mol)[26, 27] and polyunsaturated hydrocarbons(~73 kcal/mol)[27], respectively.

As mentioned above, the autoxidation of an unsaturated lipid is initiated by H-atom abstraction from where the lipid has the weakest C-H bond, which in part determines the regiochemistry of oxidation – at least, in cases where more than one type of labile C-H bond is found. The regiochemistry is also determined by where molecular oxygen adds to the resonance stabilized (delocalized) radical, and whether the addition is reversible under the reaction conditions. The product distributions that arise in the autoxidation of unsaturated lipids can therefore be highly complicated, depending on the reactions conditions, as has been illustrated by Porter and co-workers.[25, 28] For example, the autoxidation of the monounsaturated lipid methyl oleate can yield a racemic mixture of up to six regioisomeric lipid hydroperoxides: three derived from H-atom abstraction from C11: 9-*trans*, 11-*cis* and 11-*trans* (shown in Scheme 1.6); and three derived from H-atom abstraction from C8: 10-*trans*, 8-*cis* and 8-*trans* (not shown).

The products arise from H-atom abstraction at either C11 or C8, followed by O_2 addition at each face of either end of each allylic radical to yield a racemic mixture of four distinct peroxyl radical intermediates. Since this step is reversible, the rate of β−fragmentation, k_β, is important in determining the product distribution arising in the autoxidation. In the absence of a good H-atom donor (e.g. phenolic antioxidant, see Chapter 2), the racemic 9-*trans* and 11-*trans* diene hydroperoxides are produced following H-atom abstraction at C11, and the racemic 8-*trans* and

10-*trans* diene hydroperoxides are produced following H-atom abstraction at C8 since reduction of the 11-*cis* and 8-*cis* peroxyl radicals is slower than β-fragmentation and C-C bond rotation. These are the thermodynamically favored products. In the presence of a good H-atom donor, the racemic 11-*cis* and 9-*trans* diene hydroperoxides are the major products from H-atom abstraction at C11, and the racemic 8-*cis* and 10-*trans* diene hydroperoxides are the major products from H-atom abstraction at C8 since reduction of the 11-*cis* and 8-*cis* peroxyl radicals is faster than β-fragmentation and C-C bond rotation. These are the kinetically favoured products.

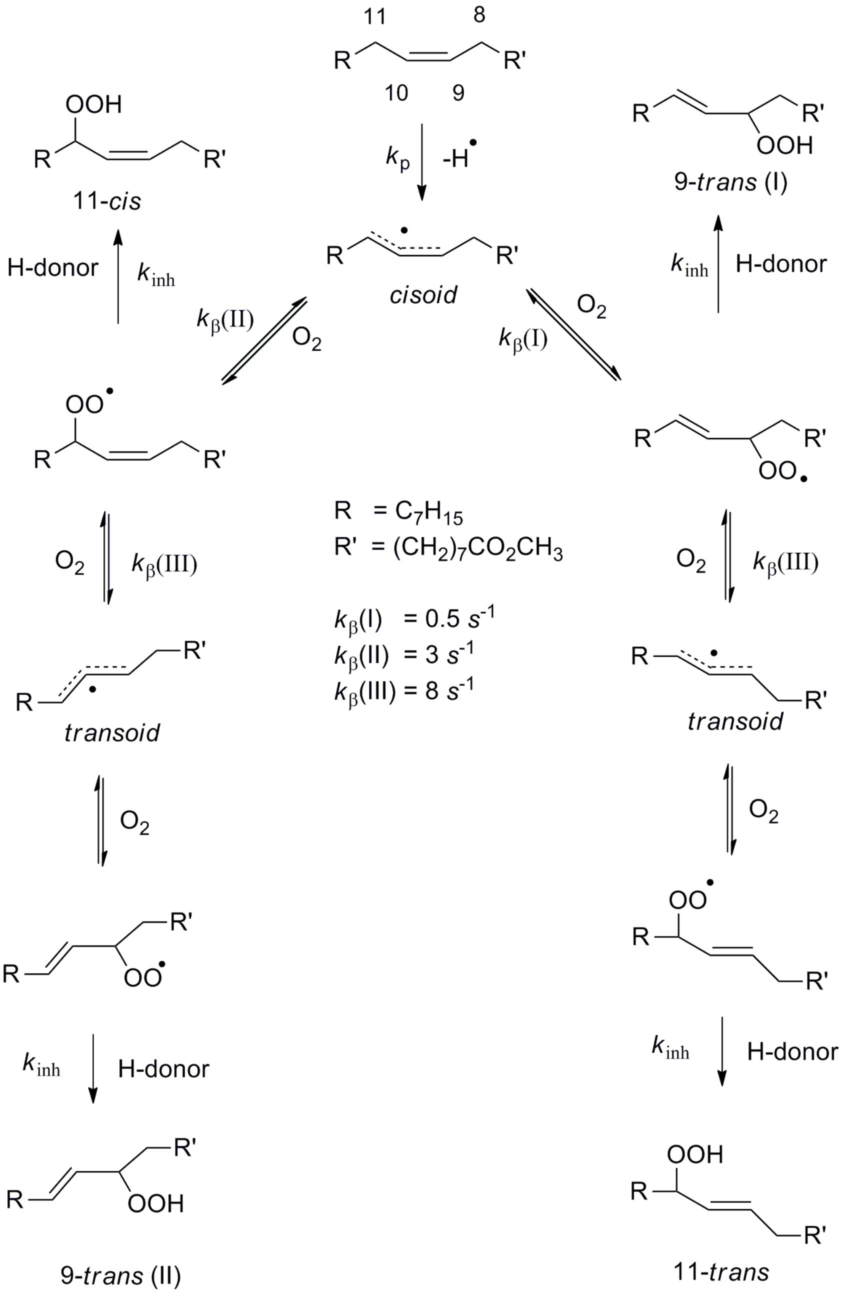

Scheme 1.6 Mechanism of methyl oleate autoxidation, where k_p is the rate constant of H-atom abstraction, k_β is the rate constant of β fragmentation of intermediate peroxyl radicals and k_{inh} is the rate constant of peroxyl radical-trapping by antioxidants.[24]

A similar mechanism can be drawn for the autoxidation of the polyunsaturated lipid methyl linoleate, which can yield a racemic mixture of up to five regioisomeric lipid hydroperoxides: 9-*t,c*, 13-*t,c*, 13-*t,t*, 9-*t,t* and 11-*c,c*-hydroperoxyoctadienoates (Scheme 1.7) and therefore 10 unique products.[13]

These products arise first because removal of the bisallylic H-atom from C11 yields a pentadienyl radical from carbons 9-13 with unpaired electron spin density at positions 9, 11 and 13 to which oxygen can add. Addition can occur to either face of the pentadienyl radical yielding a racemic mixture of 3 regioisomeric peroxyl radical intermediates. Since this step is reversible, the rate of the β-fragmentation of the peroxyl, k_β, should figure prominently in determining the product distribution arising in the autoxidation, as does k_p of the substrate. In the absence of a good H-atom donor (e.g. phenolic antioxidant, see Chapter 2), the 9- and 13-*trans,trans* diene hydroperoxides are the major products (thermodynamically favored), which arise due to rotation of the C-C bond adjacent to the allyl moiety, from which fragmentation occurrs. In the presence of a good H-atom donor, the 9- and 13-*trans,cis* diene hydroperoxides are the major products, since reduction of the 9- and 13-*trans,cis* diene peroxyls is faster than rotation and β-fragmentation. In the presence of large concentrations of good H-atom donors, the 11-*cis,cis*-hydroperoxide is observed, since now the reduction of the 11-*cis,cis*-peroxyl radical is competitive with its fragmentation. For example, when a high concentration (0.1M) of good H-donors (e.g. α-tocopherol, $k_{inh} = 3 \times 10^6$ $M^{-1}s^{-1}$) is present, the non-conjugated diene hydroperoxide can be trapped in competition with its rapid β-fragmentation ($k_\beta \sim 2 \times 10^6$ s^{-1}) to yield the bis-allylic hydroperoxide.[29] Recently, Porter et al. reported that increasing the size of substituents on C13 and C9 of the pentadienyl moiety favors the kinetic product formation due to the majority of O_2 addition occuring at the least steric hindered C11 position. Also, the substituents of C13 and C9 influence the product distribution of the conjugated hydroperoxide to favor less steric hindered product formation.[29]

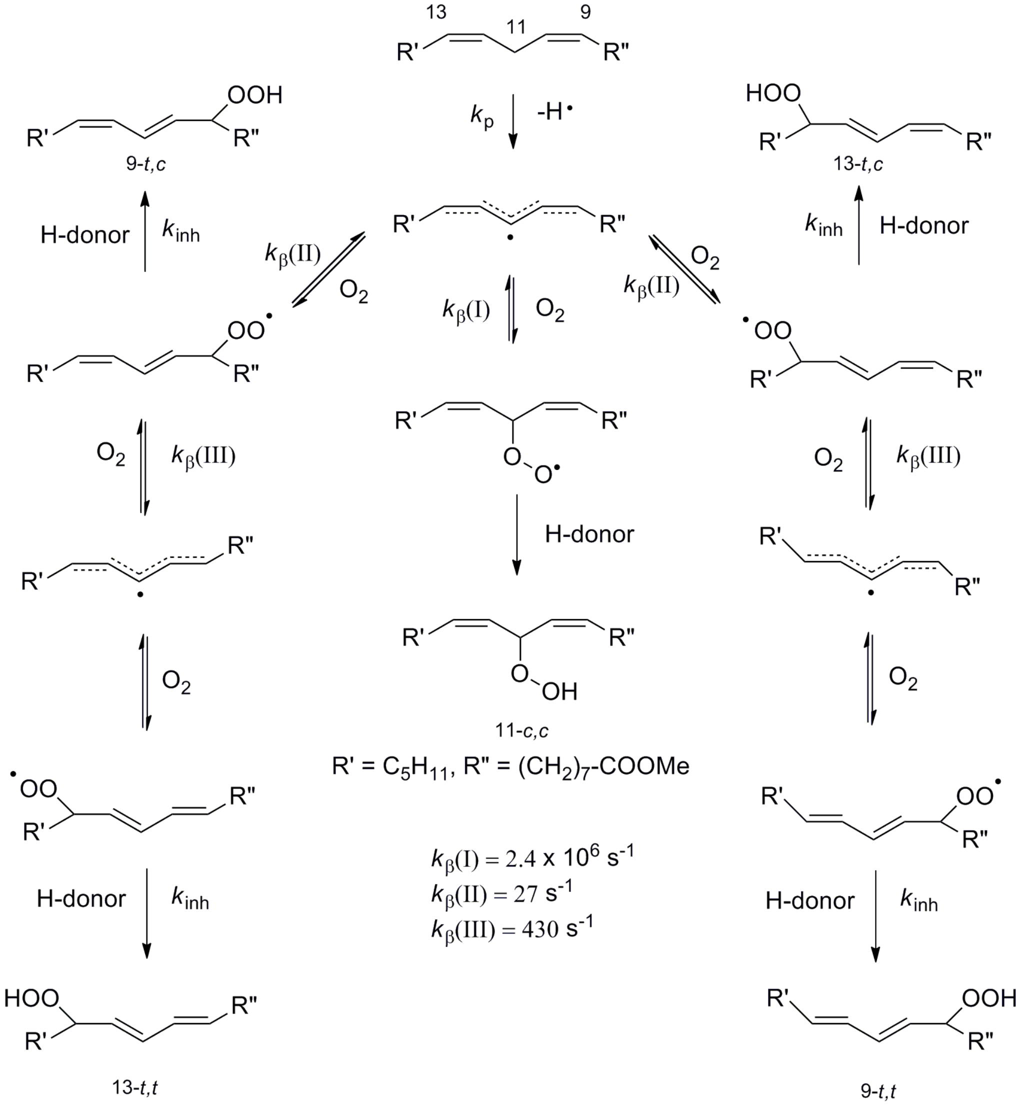

Scheme 1.7 Mechanism of methyl linoleate autoxidation, where k_p is the rate constant of H-atom abstraction, k_β is the rate constant of β fragmentation of intermediate peroxyl radicals and k_{inh} is the rate constant of peroxyl radical-trapping by antioxidants.

1.1.3 The Allylperoxyl Rearrangement

As it is shown in Schemes 1.6 and 1.7, the mono-ene peroxyl and dieneperoxyl radicals, respectively, can interconvert by β-fragmentation followed by oxygen addition. However, there is another possibility: the interconversions take place by one or more formal [2,3]-sigmatropic rearrangements, also known as the Schenk Rearrangement.[30] The most famous example of such a rearrangement involves cholesterol. [31-36] It was found experimentally that upon standing in air, the major product of cholesterol oxidation with singlet oxygen ($^1O_2$), cholesterol 5α-OOH, rearranges to cholesterol 7α-OOH (Scheme 1.8), and eventually epimerizes to a racemic mixture of the 7α and 7β-OOH's.[37]

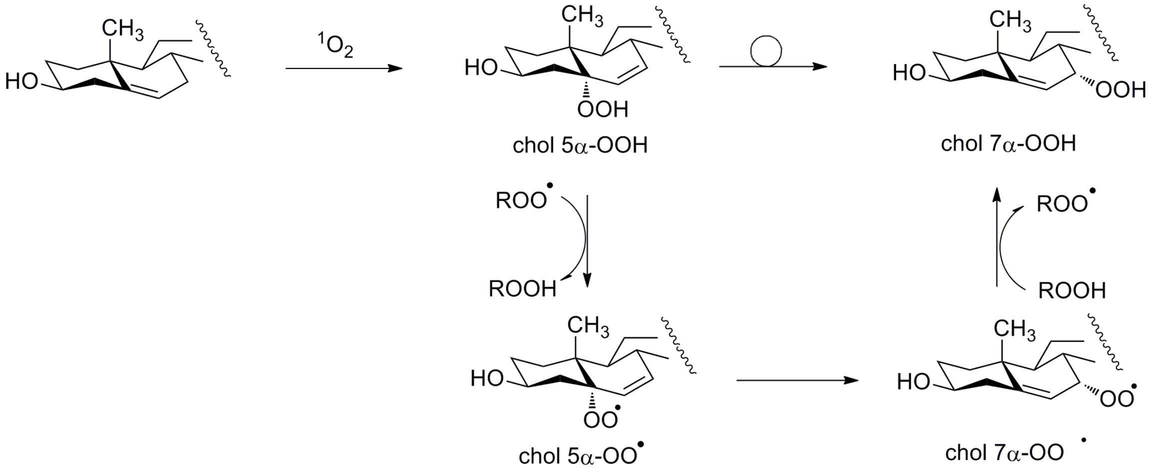

Scheme 1.8 Products of the singlet oxygen oxidation of cholesterol. The major product is initially cholesterol 5α-OOH, but it rearranges over time to a racemic mixture of both cholesterol 7α- and 7β-OOH.[37]

Although the Schenk Rearrangement has been known since the 1950s, the mechanism is still under debate.[38] Three mechanisms have been proposed, shown in Scheme 1.9.[31-36]: a two-step rearrangement via a dioxolanyl radical intermediate (path *a*), a concerted process involving no intermediate (path *b*), and a step-wise process via an allyl:dioxygen complex (path *c*).

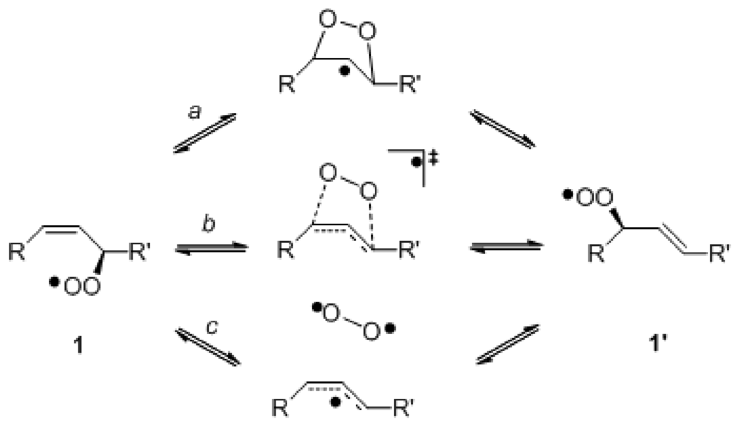

Scheme 1.9 Proposed three mechanisms for peroxyl rearrangement.

Porter and co-workers[34, 39] suggested that if a carbon radical were present during the allylic peroxyl rearrangement, this radical species would be trapped by oxygen. However, there was no dioxolanyl-derived hydroperoxide species found, suggesting that path *a* could not be the mechanism for allylperoxyl rearrangement. In 1989, Beckwith, et al.[31] demonstrated that only a small amount of ^{18}O-exchange happened when the reaction was carried out under 99.5% $^{18}O_2$, but that more $^{18}O_2$ was incorporated into the rearranged hydroperoxide from the atmosphere than the unrearranged hydroperoxide. In 1997, Porter and coworkers[40] successfully incorporated ^{18}O at the terminal oxygen position of the hydroperoxide shown in Scheme 1.10, and minimal ^{16}O exchange for ^{18}O was found under $^{16}O_2$ atmosphere. Kinetic experiments clearly demonstrated a difference in rate between transfer of the terminal peroxyl radical to the product proximal position and fragmentation of peroxyls to give the allyl radical and oxygen. This, combined with Beckwith et al's results and demonstrations of the stereoselectivity of the rearrangement,[41, 42] suggest that either a concerted rearrangement or step-wise rearrangement via an allyl:dioxygen complex may take place, but it is unclear which.

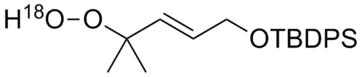

TBDPS = tert-Butyl(chloro)diphenylsilane

Scheme 1.10 Schematic picture of TBDPS

To help delineate which mechanism is operating, computational work has also been carried out on the mechanism of allylperoxyl rearrangement. Early work using simple Hartree-Fock theory and a small basis set excluded path *a* (in agreement with the experiments), but were unable to distinguish between the other two paths. More recently, Olivella and Sole[43] studied the allylperoxyl rearrangement using a combination of second order Møller-Plesset perturbation theory (MP2) and coupled cluster theory (CCSD(T)). Their results support path *c*, a step-wise process, because the calculated $\Delta H^{\ddagger}$ for the step-wise path was 21.7 kcal/mol, 1.9 kcal/mol lower than calculated $\Delta H^{\ddagger}$ = 23.6 kcal/mol for the concerted process (path *b*). Unfortunately, several errors have subsequently been identified in the work of Olivella and Sole, calling into question the validity of these conclusions. Therefore, what theory has to say about this rearrangement remains an open question.

1.2 Objective

Unsaturated lipids in cell membranes, including phospholipids and cholesterol, are well known targets for oxidative modification. From previous studies, rates of H-atom abstraction from various lipids, as well as rates of β-fragmentation of the peroxyl radical intermediates have been obtained, and have proved useful in predicting the product distribution of lipid autoxidation. However, speculation still exists on the mechanisms of these reactions, as well as the important rearrangements of the intermediate peroxyl radicals. Therefore, the objective of this chapter is to establish a detailed computational framework for understanding the mechanism of autoxidation of lipids using propene and pentadiene as models for mono- and polyunsaturated lipids, respectively. In particular, in the propagation step involving the formal H-atom abstraction from the lipid, we are interested in the geometries and relative energetics of the transition states (TS) of the reactions and how they contribute to the product distributions arising in lipid peroxidation. The subsequent addition of O_2 and rearrangements of the peroxyl radicals are also of interest, in particular in light of the contradicting results provided by previous studies.

1.3 Methodology

For all of the calculations reported here, propene was used as a model compound for monounsaturated lipids and 1,3- and 1,4-pentadiene were used a model compounds for conjugated and non-conjugated polyunsaturated lipids, respectively. The simplest alkylperoxyl radical – methylperoxyl – was used as a model compound for the chain-carrying lipid peroxyl radicals in calculations of the first chain propagation step; H-atom abstraction. For the monounsaturated lipid model system, the structures of the starting materials and the transition states were optimized using both density functional theory at the B3LYP level and second order Møller-Plesset perturbation theory (MP2) with a 6-311+G(3df,2p) basis set. For the poly-unsaturated model system, the structures of the starting materials and the transition states were also optimized using both B3LYP and MP2, but with a slightly smaller 6-311+G(2df,p) basis set. All stationary points were characterized as minima (all positive frequencies) or transition states (single negative frequency with appropriate atomic displacements) on the potential energy surface by vibrational frequency calculations. Single point energy calculations were then performed on these structures using both unrestricted and restricted open-shell coupled-cluster theory (UCCSD(T) and ROCCSD(T), respectively) with 6-311+G(3df,2p) and 6-311+G(d) basis sets for the monounsaturated and polyunsaturated lipid model systems, respectively.

The second propagation step, oxygen addition to the substrate derived alkyl radicals (allyl as a model for monounsaturated lipids and pentadienyl as a model for polyunsaturated lipids, respectively) and their subsequent rearrangements, were also studied using both B3LYP and MP2 with 6-311+G(3df,2p) and 6-311+G(2d,p) basis sets, respectively. All stationary points were characterized as minima or transition states on the potential surface by vibrational frequency calculations. Single point energy calculations were then performed on these structures again using both UCCSD(T) and ROCCSD(T) with 6-311+G(3df,2p) and 6-311+G(2d,p) basis sets for the monounsaturated and polyunsaturated models, respectively.

All calculations were performed with the Gaussian 03 suite of programs compiled to run on Sun Microsystems SunFire 25000 or Enterprise M9000 servers with UltraSPARC-IV+ or Sparc64 VII CPUs, respectively except the ROCCSD(T) calculations, which were performed with the Gaussian 09 suite of programs compiled to run on HP Linux XC 3.1 system with interconnect Quadrics Elan4.

1.4 Results

1.4.1 Propagation Step 1: H-Atom Abstraction From Unsaturated Lipids

The B3LYP and MP2 optimized geometries of the individual starting materials for our studies of the first propagation step are shown below in Figure 1.1. The corresponding B3LYP and MP2 calculated enthalpies at 298 K are provided together with enthalpies obtained from the

UCCSD(T) and ROCCSD(T) single point calculations (combined with the enthalpy corrections from the respective B3LYP and/or MP2 calculations) in Table 1.1.

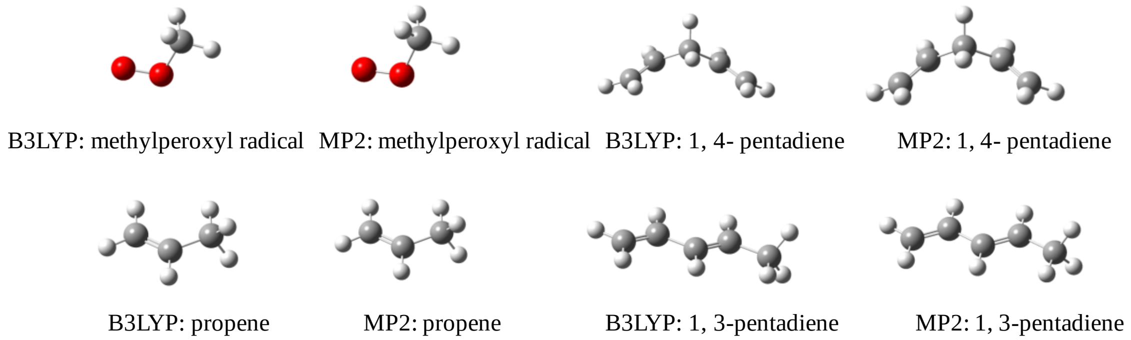

B3LYP: methylperoxyl radical MP2: methylperoxyl radical B3LYP: 1, 4- pentadiene MP2: 1, 4- pentadiene

B3LYP: propene MP2: propene B3LYP: 1, 3-pentadiene MP2: 1, 3-pentadiene

Figure 1.1 B3LYP and MP2 optimized structures of relevant participants in model studies of the first propagation in the autoxidation of monounsaturated (6-311+G(3df,2p)) and polyunsaturated (6-311+G(2df,p)) lipids.

Table 1.1 Enthalpies (in Hartree) of starting materials optimized using both B3LYP and MP2, and the corresponding enthalpies obtained using single point CCSD(T) electronic energies.

	B3LYP	***CCSD(T)***	***MP2***	***CCSD(T)***
Propene[a]	-117.869348	-117.470951	-117.869348	-117.869348
Methylperoxyl radical[a]	-190.243957	-189.757520	-190.243957	-190.243958
1, 3-pentadiene[b]	-195.2468512	-194.7485647	-194.702654	-194.789263
1, 4-pentadiene[b]	-195.2606852	-194.7385696	-194.690808	-194.778282
Methylperoxyl radical[b]	-190.2411418	-189.8051984	-189.824453	-189.877613

[a] 6-311+G(3df,2p). [b] 6-311+G(2df,p).

1.4.1.1 Monounsaturated Lipid Model

Two transition state (TS) structures were identified for the abstraction of an H-atom from propene by the methylperoxyl radical by B3LYP and MP2, and are shown in Figure 1.2 along with some key geometrical features. In addition, the most relevant molecular orbitals (MOs), namely the highest (doubly)-occupied MO (HOMO) and singly-occupied MO (SOMO), calculated using the same methods are shown alongside.

The lowest energy transition state we denote as *cisoid*, since the substituents on the carbon and oxygen between which the H-atom is being transferred are *syn* to each other (making the dihedral angle between A and D close to zero in Figure 1.2). In contrast, we denote the second transition structure *transoid*, since the substituents on the carbon and oxygen between which the H-atom is being transferred are *anti* to each other (making the dihedral angle between A and D closer to 180^{o} in Figure 1.2). For each of the TS structures, B3LYP predicts a longer distance between the carbon and oxygen between which the H-atom is being transferred and a more planar arrangement of these atoms and the heavy atoms directly bonded to them.

According to each of the calculated activation energies (E_a), H-atom abstraction from propene via the *cisoid* TS is consistently preferred over the *transoid* TS. The differences are 1.1 kcal/mol and 2 kcal/mol from UCCSD(T) calculations on the B3LYP and MP2 optimized structures, respectively (Table 1.2). The interaction between the π HOMO of propene and the π* SOMO of the methylperoxyl radical would appear to be key in lending stability to the *cisoid* TS structure.

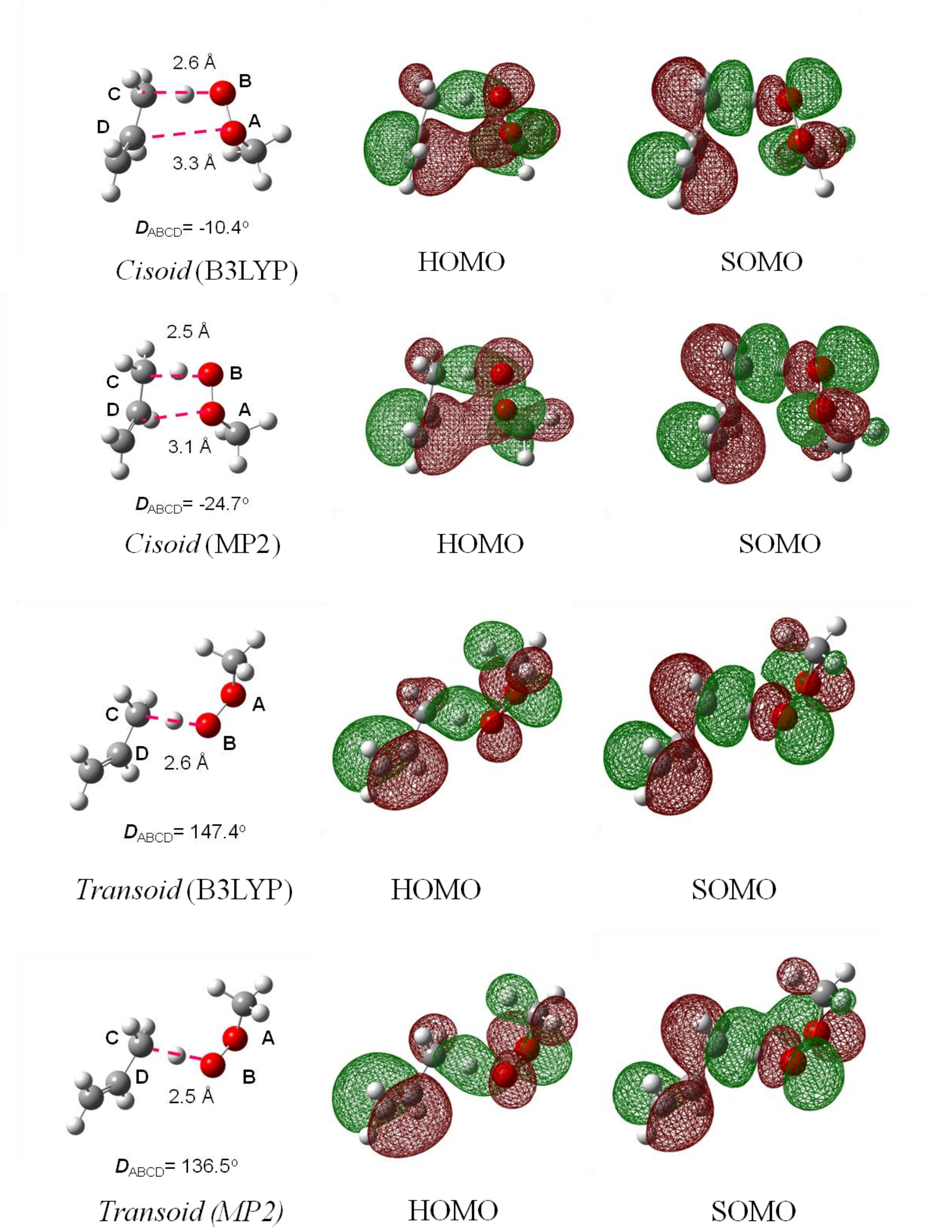

Figure 1.2 B3LYP/6-311+G(3df,2p)) and MP2/6-311+G(3df,2p)) structures of relevant transition states in model studies of the first propagation step in the autoxidation of monounsaturated lipids.

Table 1.2 Activation energies (E_a in kcal/mol) of H-atom abstraction from propene determined by UCCSD(T)/6-311+G(3df,2p) single point calculations at MP2/6-311+G(3df,2p) and B3LYP/6-311+G(3df,2p) optimized geometries. ($E_a = \Delta H^{\ddagger} + 2RT$, where R=1.9859 kcal/K.mol and T=298 K).

	UB3LYP	***UCCSD(T)***	***UMP2***	***UCCSD(T)***
***Cisoid* TS**	15.1	18.7	21.8	19.0
***Transoid* TS**	15.4	19.8	22.9	21.0

1.4.1.2 Polyunsaturated Lipid Model

Similarly to the monounsaturated lipid model above, two transition state (TS) structures were identified for the abstraction of a H-atom from 1,3-pentadiene, the conjugated polyunsaturated lipid model, by the methylperoxyl radical using both B3LYP and MP2, shown in Figure 1.3. In addition, the most relevant molecular orbitals (MOs), namely the HOMO and SOMO, calculated using the same methods are again shown alongside.

Again, we have denoted one TS as *cisoid* and one as *transoid* based on the orientation of the substituents on the carbon and oxygen between which the H-atom is being transferred. Also, consistent with the results obtained with the monounsaturated model, for each of the TS structures, B3LYP predicts a longer distance between the carbon and oxygen between which the H-atom is being transferred and a more planar arrangement of these atoms and the heavy atoms directly bonded to them.

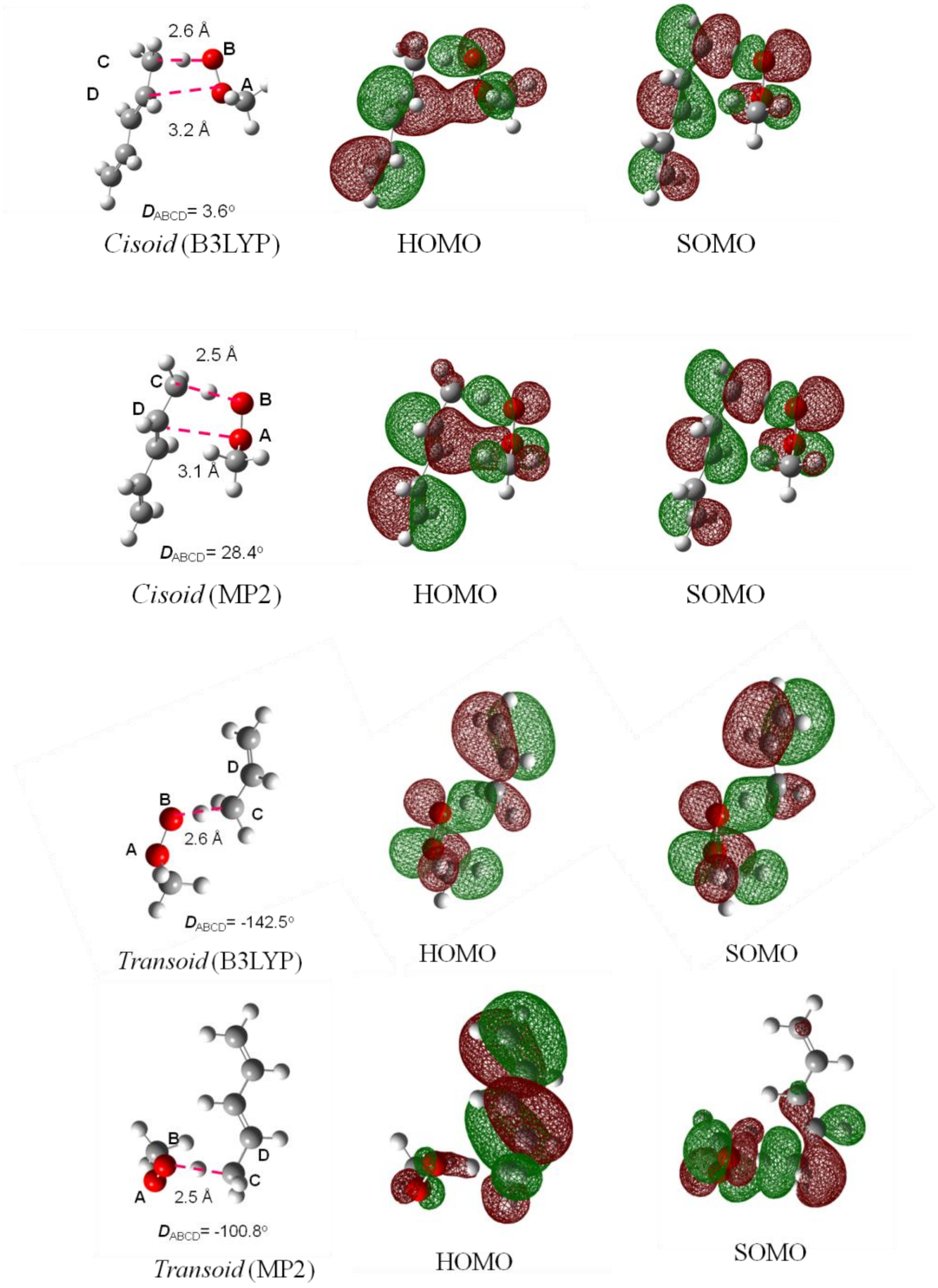

Figure 1.3 B3LYP/6-311+G(2df,p) and MP2/6-311+G(2df,p) structures of relevant transition states in model studies of the first propagation step in the autoxidation of conjugated polyunsaturated lipids.

Due to the symmetry of 1,4-pentadiene, the model compound for the first propagation step in the autoxidation of non-conjugated polyunsaturated lipids, a single TS for H-atom abstraction by methylperoxyl was found by both B3LYP and MP2. These are shown in Figure 1.4 alongside the most relevant molecular orbitals (MOs), namely the HOMO and SOMO, calculated using the same methods.

Similar to the other calculated TS structures, B3LYP predicts a longer distance between the carbon and oxygen between which the H-atom is being transferred. However, in this case, MP2 predicts a much more planar arrangement of these atoms and the heavy atoms directly bonded to them, with the dihedral angle differing only by 1.6^o from that predicted by B3LYP.

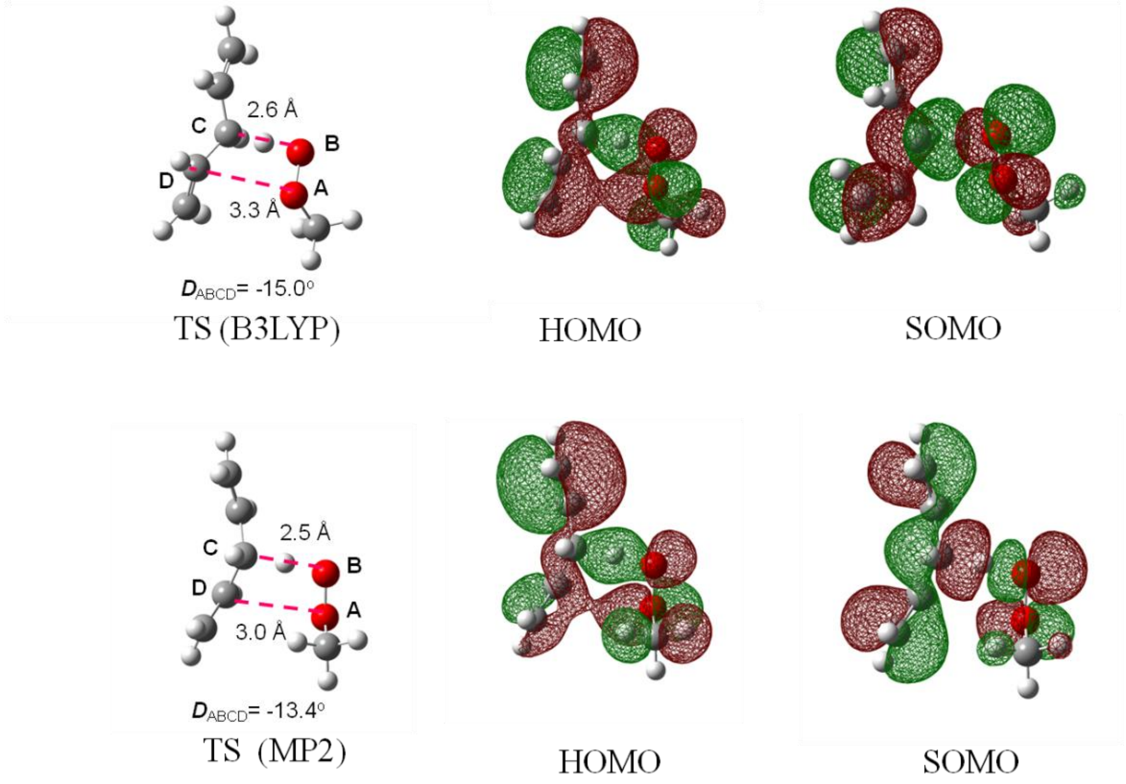

Figure 1.4 B3LYP/6-311+G(2df,p) and MP2/6-311+G(2df,p) structures of relevant transition states in model studies of the first propagation step in the autoxidation of non-conjugated polyunsaturated lipids.

The calculated E_a for these reactions are given in Table 1.3. With the exception of the result predicted by MP2, the calculations again predict that the formal H-atom transfer occurs preferentially by a *cisoid* TS, as can be seen when 1,3-pentadiene is the substrate. Similar to the calculated TS's for H-atom abstraction from propene, it would appear that the interaction between the π HOMO of the 1,3-pentadiene and the π* SOMO of the methylperoxyl radical is key in lending stability to the *cisoid* TS structure. The preference for the *cisoid* TS over the *transoid* TS is slightly larger when 1,3-pentadiene is the substrate compared to propene, perhaps because the diene HOMO is higher-lying and better able to interact with the peroxyl SOMO. The spurious MP2 result is likely due to significant spin contamination in the reference HF wavefunction.

Table 1.3 Activation energies (E_a in kcal/mol) of H-atom abstraction from 1,3- and 1,4-pentadiene determined by UCCSD(T)/6-311+G(2df,p) single point calculations at MP2/6-311+G(2df,p) and B3LYP/6-311+G(2df,p) optimized geometries. ($E_a = \Delta H^{\ddagger} + 2RT$, where R=1.9859 kcal/K.mol and T=298 K).

	UB3LYP	***UCCSD(T)***	***UMP2***	***UCCSD(T)***
Propene *cisoid* TS	15.1	18.7	21.9	20.9
Propene *transoid* TS	15.4	19.9	23.0	21.4
1,3-pentadiene *cisoid* TS	12.0	17.7	28.2	21.8
1,3-pentadiene *transoid* TS	12.4	19.3	21.6	22.9
1,4-pentadiene	9.0	12.5	20.7	17.1

Not unexpectedly, the calculated E_a values for H-atom abstraction from 1,4-pentadiene are lower than for the conjugated isomer. The UCCSD(T)-calculated differences are 5.2 kcal/mol at the UB3LYP geometry and 4.7 kcal/mol at the UMP2 geometry.

1.4.1.3 Calculated C-H BDEs for Model Unsaturated Lipids

In order to compare the predicted kinetics of these reactions (in terms of E_a) with thermodynamics, we also calculated the BDEs of the C-H bonds which are broken in the reaction using the same methods. The results are shown in Table 1.4.

Table 1.4 Calculated C-H BDEs (kcal/mol) for H-atom abstraction from propene, 1,3-pentadiene and 1,4-pentadiene. All values shown were obtained with the 6-311+G(2df,p) basis set. Differences from the calculated BDE in propene are given in parentheses.

	B3LYP	*UCCSD(T)*	*ROCCSD(T)*	*MP2*	*UCCSD(T)*	*ROCCSD(T)*
Propene[a]	83.4	85.2	85.9	89.8	85.7	85.3
	(0.0)	(0.0)	(0.0)	(0.0)	(0.0)	(0.0)
1,3-Pentadiene	77.8	80.6	79.8	91.3	82.0	81.3
	(-5.6)	(-4.6)	(-6.1)	(+0.5)	(-3.7)	(-4.0)
1,4-Pentadiene	69.1	73.7	72.9	83.9	75.1	74.4
	(-14.3)	(-11.5)	(-13.0)	(-5.9)	(-10.6)	(-10.9)

[a] Calculated C-H BDEs with the 6-311+G(3df,2p) basis set in the order in which they appear across the row are: 83.9, 86.2, 85.9, 90.9, 86.7 and 86.3 kcal/mol.

1.4.1.4 Calculated k_p for H-Abstraction from Model Lipids

The propagation rate constants corresponding to H-atom abstraction from propene, 1,3-pentadiene and 1,4-pentadiene by methylperoxyl were calculated using conventional transition state theory (Eq. 1.1)[44], with the MP2 and DFT-calculated partition functions and the UCCSD(T) electronic energies corrected with the MP2 and DFT zero-point energies. In Eq. 1.1, k_B is the Boltzmann constant 1.38 x 10^{-23} J·K^{-1}, h is the Planck constant 6.62 x 10^{-34} J·s, Q is the partition function of DFT or MP2 optimized structures the and ΔE_0 is the zero point energy difference between the TS and the separated reactants.

$$k = \frac{RT}{p}\frac{k_B T}{h}\frac{Q_{TS}}{Q_{SM1}Q_{SM2}}e^{\frac{-\Delta E_0}{RT}} \qquad \text{Eq. 1.1}$$

Table 1.5 Calculated rate constants for H-atom abstration from propene, 1,3-pentadiene and 1,4-pentadiene by the methylperoxyl radical and the corresponding experimental rate constants for the analogous mono- and polyunsaturated lipids for comparison.[1]

Calculated Rate Constant ($M^{-1}s^{-1}$)			Experimental Rate Constant ($M^{-1}s^{-1}$)	
	B3LYP	MP2		
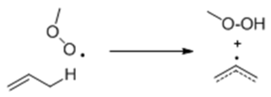	8×10^{-8} (*syn*) 1.5×10^{-8} (*anti*)	4.8×10^{-8} (*syn*) 2.2×10^{-9} (*anti*)	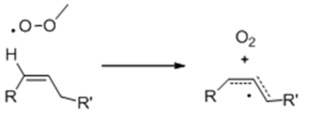	~1
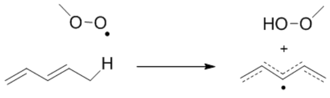	4.7×10^{-7} (*syn*) 4.6×10^{-8} (*anti*)	1.7×10^{-10} (*syn*) 3.3×10^{-11} (*anti*)	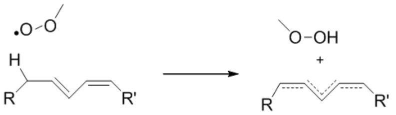	N/A
	1.5×10^{-4}	3.4×10^{-7}	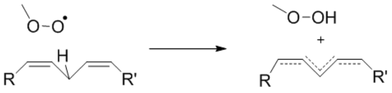	62

[1] Propagation rate constants k_p for oleate (~1 $M^{-1}s^{-1}$) and linoleate (62 $M^{-1}s^{-1}$). [24, 45]

1.4.2 Propagation Step 2: Reversible Addition of O_2 to Radicals Derived From Unsaturated Lipids

The B3LYP and MP2 optimized geometries of the individual starting materials for our studies of the second propagation step are shown below in Figure 1.5. Alongside are presented isodensity surfaces which display the distribution of the unpaired electron spin density in each of the delocalized radicals. The corresponding B3LYP and MP2 calculated enthalpies at 298 K are provided together with enthalpies obtained from the U/RO CCSD(T) single point calculations (combined with the enthalpy corrections from the B3LYP/MP2 calculations) in Table 1.5.

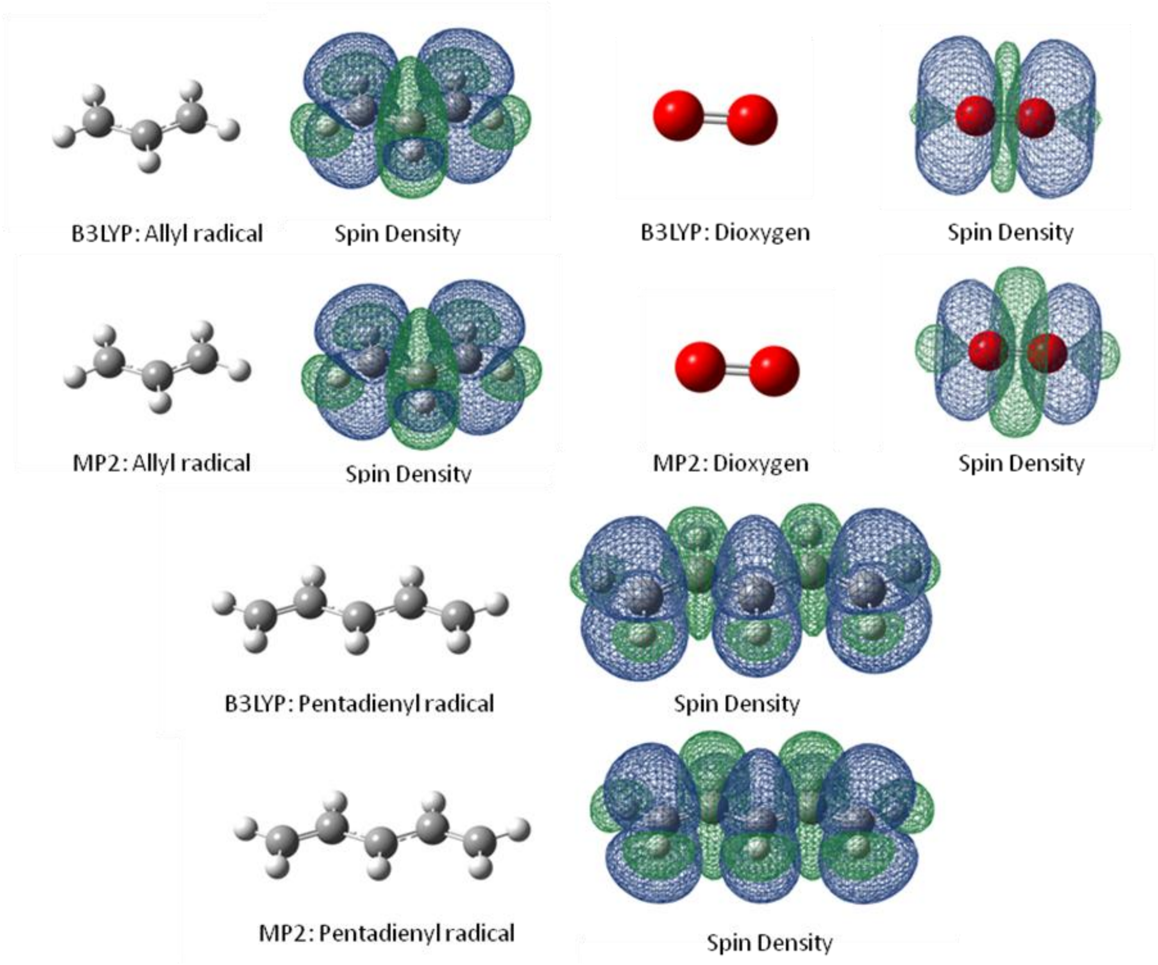

Figure 1.5 B3LYP and MP2 optimized allyl, pentadienyl radical and di-oxygen, along with their spin density surfaces.

Table 1.6 Enthalpies (in Hartree) of starting materials optimized using both B3LYP and MP2, and the corresponding enthalpies obtained using single point CCSD(T) electronic energies.

	B3LYP	***UCCSD(T)***	***ROCCSD(T)***
Oxygen[a]	-150.3724325	-150.121193	-150.121159
Allyl[a]	-116.8892802	-116.955011	-116.955597
Oxygen[b]	-150.371449	-150.037755	-150.071603
Pentadienyl[b]	-194.636878	-194.010372	-194.103825
	MP2	***UCCSD(T)***	***ROCCSD(T)***
Oxygen[a]	-150.1014555	-150.121438	-150.121399
Allyl[a]	-116.8892802	-116.953381	-150.121399
Oxygen[b]	-150.0948961	-150.038054	-150.072201
Pentadienyl[b]	-194.059700	-194.006577	-194.100412

[a] 6-311+G(3df,2p)

[b] 6-311+G(2df,p)

1.4.2.1 Monounsaturated Lipid Model

Two transition state (TS) structures for the addition of O_2 to the allyl radical were identified using B3LYP, and are shown in Figure 1.6 along with some key geometrical features and an isodensity plot of the HOMO of each structure, calculated using the same methods.

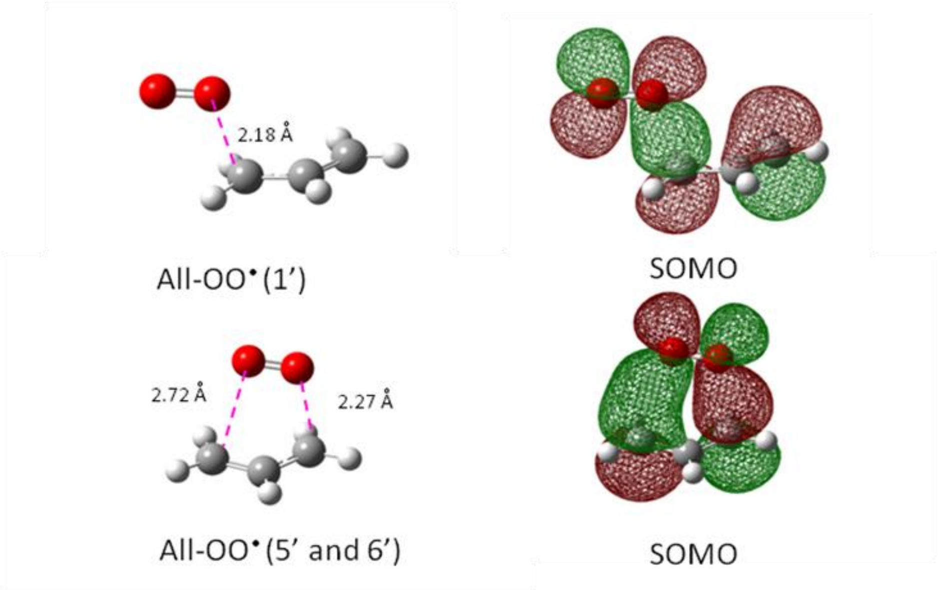

Figure 1.6 B3LYP/6-311+G(3df,2p)-optimized TS structures for addition of O_2 to the allyl radical in the *anti* conformation (**1'**) and *syn* conformation (**5'** and **6'**).

The first TS structure we denote *anti*, since the dioxygen moiety and carbon framework have an *anti* relationship with respect to the incipient peroxyl C-O bond, and the second is *syn*. Conversely, only a single mode of O_2 addition to the allyl radical was identified using MP2, that which possesses an *anti* geometry. A TS structure similar to the B3LYP *syn* structure was identified, but the atomic displacements are consistent with a concerted rearrangement of the allylperoxyl radical. These are shown in Figure 1.7.

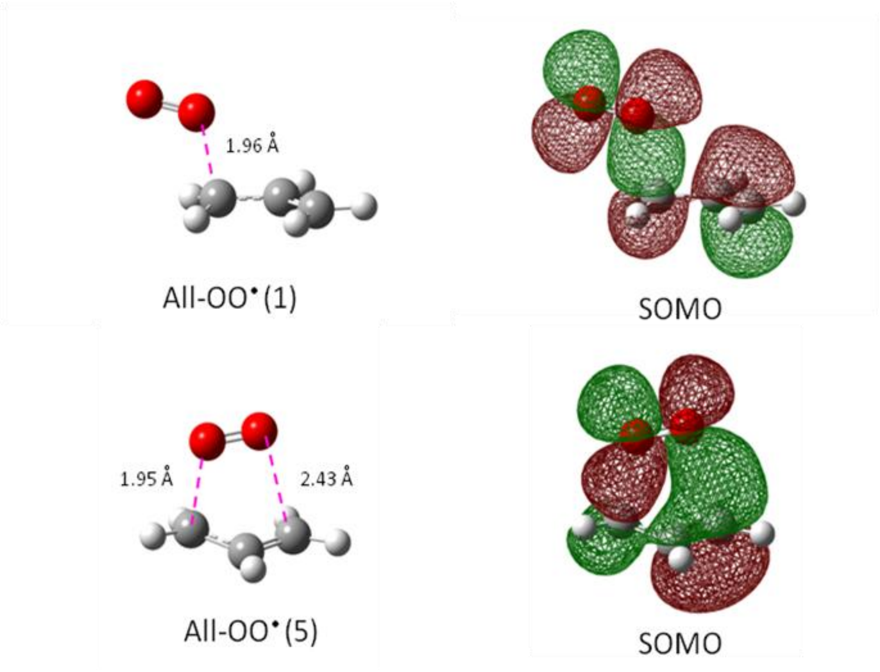

Figure 1.7 MP2/6-311+G(3df,2p)-optimized TS structures for the addition of O_2 to the allyl radical in the *anti* conformation (**1**) and the concerted allylperoxyl rearrangement (**5**).

Previous studies have shown that the allyl radical and dioxygen are predicted to form a bound complex at the MP2/6-311+G(3df,2p) level of theory.[43] We therefore calculated this structure using the same method, as well as by using the B3LYP/6-311+G(3df, 2p) level of theory, and followed these by CCSD(T) single point calculations with both an unrestricted (U) and restricted open shell (RO) reference wavefunction. The structures are shown in Figure 1.8 along with some key geometrical features and an isodensity plot of the HOMO of each structure, calculated using the same methods.

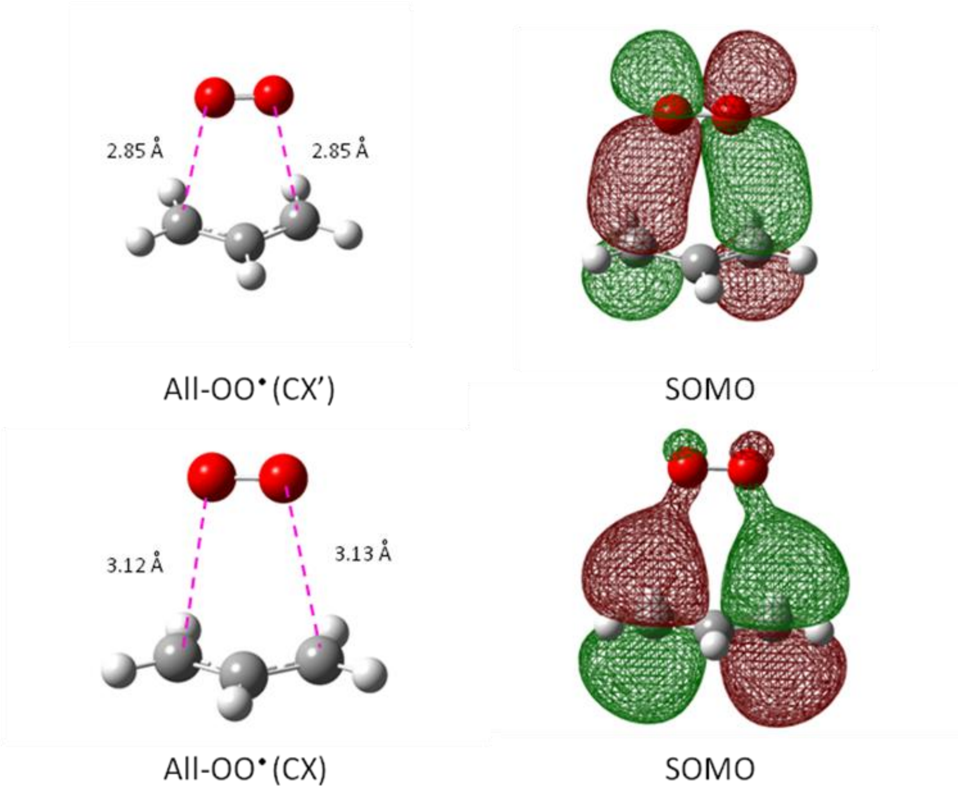

Figure 1.8 B3LYP/6-311+G(3df,2p)-optimized complex All-OO•(**CX'**) and MP2/6-311+G(3df,2p)-optimized complex All-OO•(**CX**).

In order to construct a complete potential energy surface for the addition of O_2 and the interconversion of the resultant allylperoxyl radicals, we also calculated the structures and energetics of the possible product allylperoxyl radical conformations, and these are shown below in Figures 1.9 and 1.10.

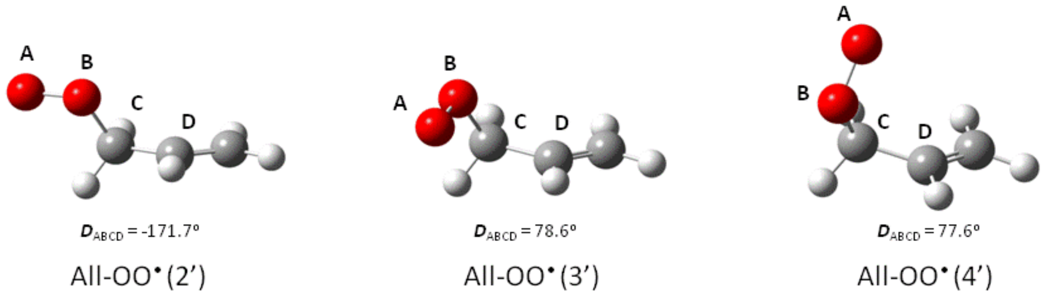

D_{ABCD} = -171.7° All-OO• (2′)

D_{ABCD} = 78.6° All-OO• (3′)

D_{ABCD} = 77.6° All-OO• (4′)

Figure 1.9 B3LYP/6-311+G(3df,2p)-optimized structures of the low energy conformers of the allylperoxyl radical.

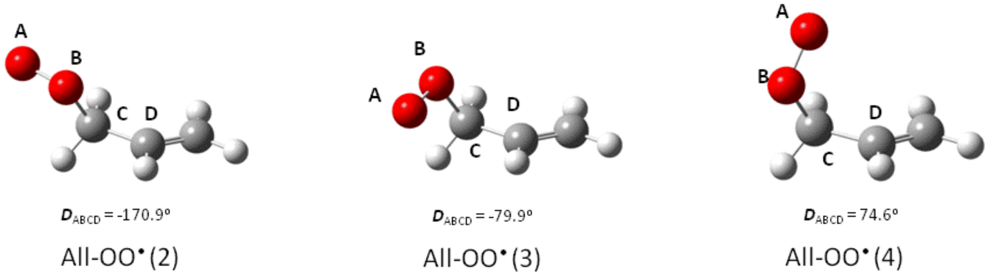

D_{ABCD} = -170.9° All-OO• (2)

D_{ABCD} = -79.9° All-OO• (3)

D_{ABCD} = 74.6° All-OO• (4)

Figure 1.10 MP2/6-311+G(3df,2p)-optimized structures of the low energy conformers of the allylperoxyl radicals.

The overall potential energy surface for *anti* and *syn* addition of O_2 to the allyl radical, and the interconversion of the allylperoxyl isomers is depicted in Figure 1.11 and the relative enthalpies at all levels of theory studied here are included in Table 1.7.

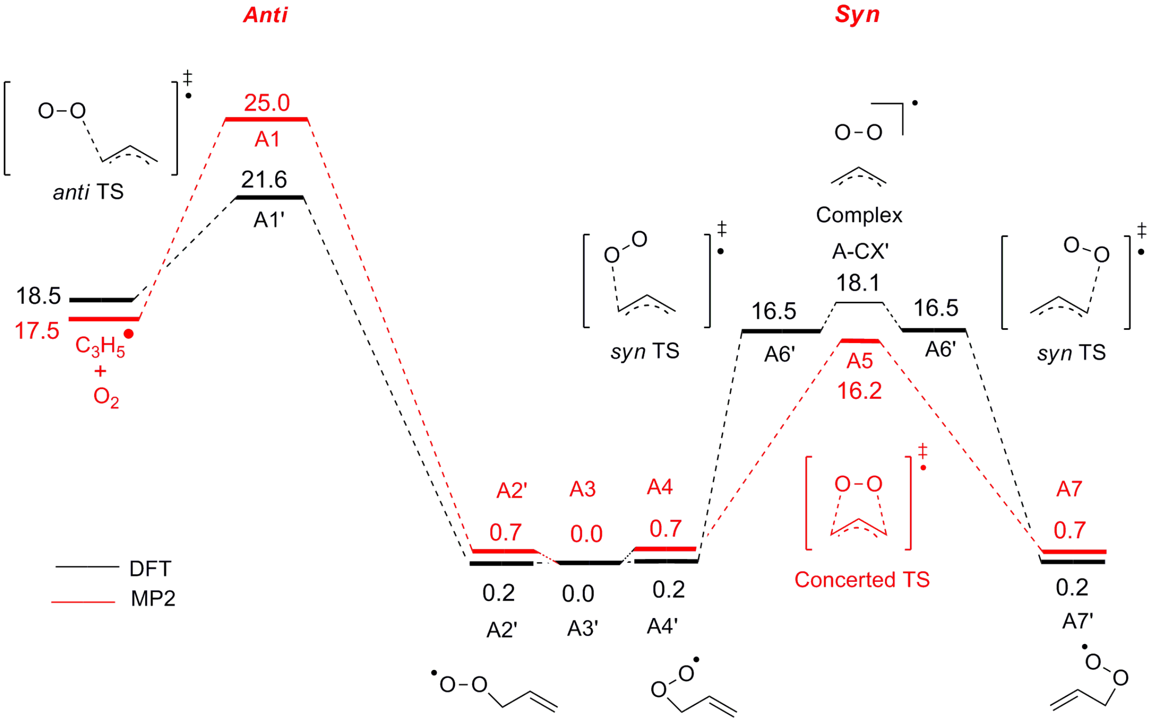

Figure 1.11 Schematic enthalpy profile for the addition of oxygen to the allyl radical, and the degenerated rearrangement of the resulting allylperoxyl radical (values in kcal/mol, determined by UCCSD(T)/6-311+G(3df,2p) calculations at UMP2/6-311+G(3df,2p) and UB3LYP/6-311+G(3df,2p) geometries.

Table 1.7 Relative enthalpies (Δ*H*) in kcal/mol of the relevant stationary points shown in Figure 1.11 calculated using UCCSD(T) and ROCCSD(T) with a 6-311+G(3df,2p) basis set on structures optimized using both B3LYP and MP2 with a 6-311+G(3df,2p) basis set.

Structures	***B3LYP***	***UCCSD(T)***	***RO CCSD(T)***	***Structures***	***MP2***	***UCCSD(T)***	***RO CCSD(T)***
C_3H_5•+ O_2	13.7	18.5	18.2	C_3H_5•+ O_2	17.9	17.5	17.2
A1’	16.8	21.6	21.9	A1	36.4	25.0	20.7
A2’	0.1	0.2	0.2	A2	0.7	0.7	0.7
A3’	0.0	0.0	0.0	A3	0.0	0.0	0.0
A4’	0.3	0.2	0.2	A4	0.9	0.7	0.7
A5’and A6’	14.4	16.5	16.7	A5	17.4	16.2	16.0
A-CX’	13.9	18.1	18.5	A-CX	17.4	16.9	45.9
A7’	0.3	0.2	0.2	A7	0.9	0.7	0.7

1.4.2.2 Polyunsaturated Lipid Model

Three transition state (TS) structures for the addition of O_2 to the pentadienyl radical were identified using B3LYP, and are shown in Figure 1.12 along with some key geometrical features and an isodensity plot of the HOMO of each structure, calculated using the same methods.

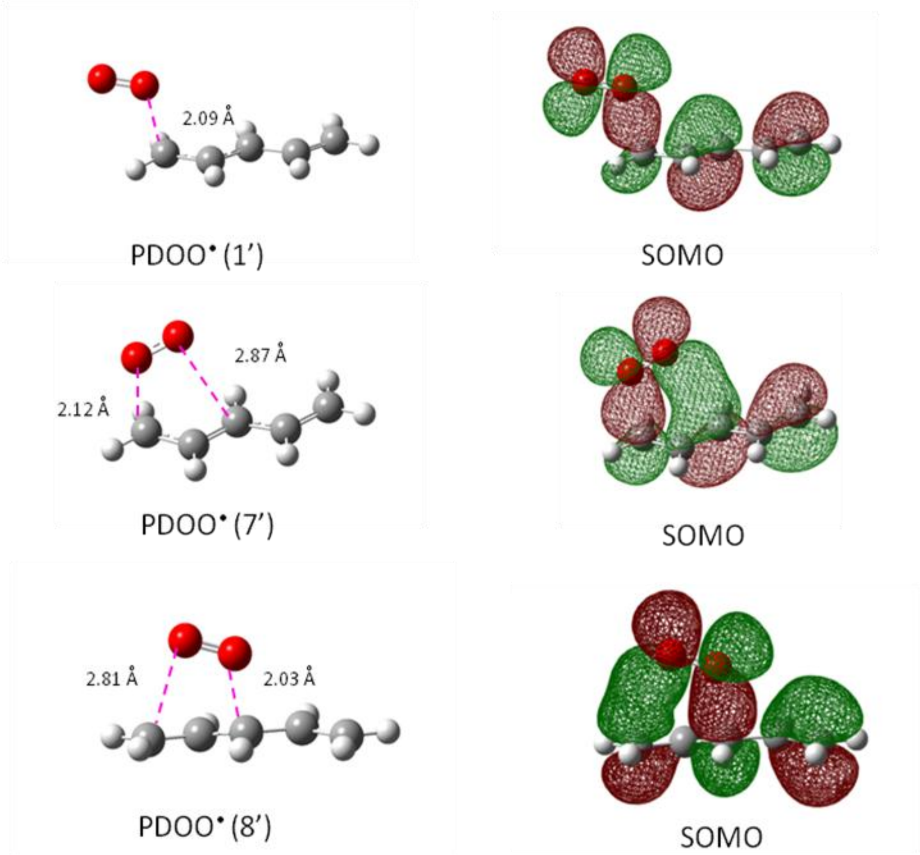

Figure 1.12 B3LYP/6-311+G(2df,p)-optimized TS structures for addition of O_2 to the terminal carbon of the pentadienyl radical in the *anti* conformation (**1'**) and the *syn* conformation (**7'**) as well as to the central position of the pentadienyl radical (**8'**).

The first and second TS structures (P1' and P7') correspond to the addition of O_2 to the terminal carbon atoms of the symmetrical pentadienyl radical. Again, we denote them *anti* and *syn* analogous to the TS structures for addition of O_2 to the allyl radical described above. Since the pentadienyl radical also has positive unpaired electron spin density at the central carbon, we were also able to locate a TS structure corresponding to the addition of O_2 at the central carbon atom. In contrast with the allyl/O_2 model, both B3LYP and MP2 methods are able to predict the

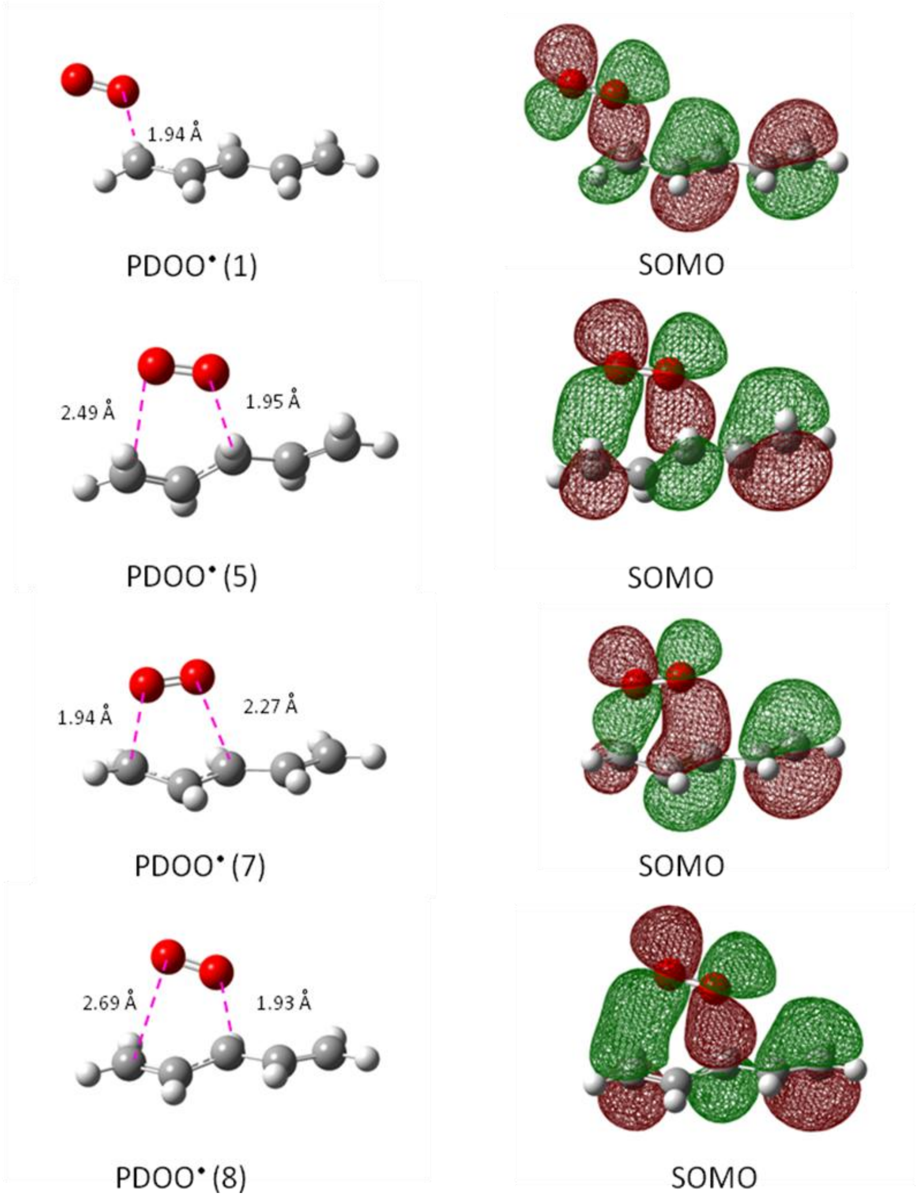

Figure 1.13 MP2/6-311+G(2df,p)-optimized TS structures for addition of O_2 to the terminal carbon of the pentadienyl radical in the *anti* conformation (**1**) and the *syn* conformation (**7**) as well as to the central position of the pentadienyl radical (**8**). The TS structure for the concerted rearrangement of the pentadienylperoxyl radical (**5**) is also shown.

syn and *anti* modes of O_2 addition to the pentadienyl radical. The MP2 structures, as well as some key geometrical features and calculated HOMOs are shown in Figure 1.13. Also shown is a fourth TS structure which has atomic displacements that are consistent with a concerted rearrangement of the pentadienylperoxyl radical.

Previous studies and our own calculations have shown that the allyl radical and dioxygen are predicted to form a bound complex.[43] We therefore performed calculations to evaluate whether the pentadienyl radical and dioxygen are also predicted to form bound complexes. complex using both MP2 and B3LYP with a 6-311+G(2df,p) basis set, and followed it with CCSD(T) single point calculations with both an unrestricted and restricted open shell reference wavefunction. The structures are shown in Figure 1.14 along with some key geometrical features and an isodensity plot of the HOMO of each structure, calculated using the same methods.

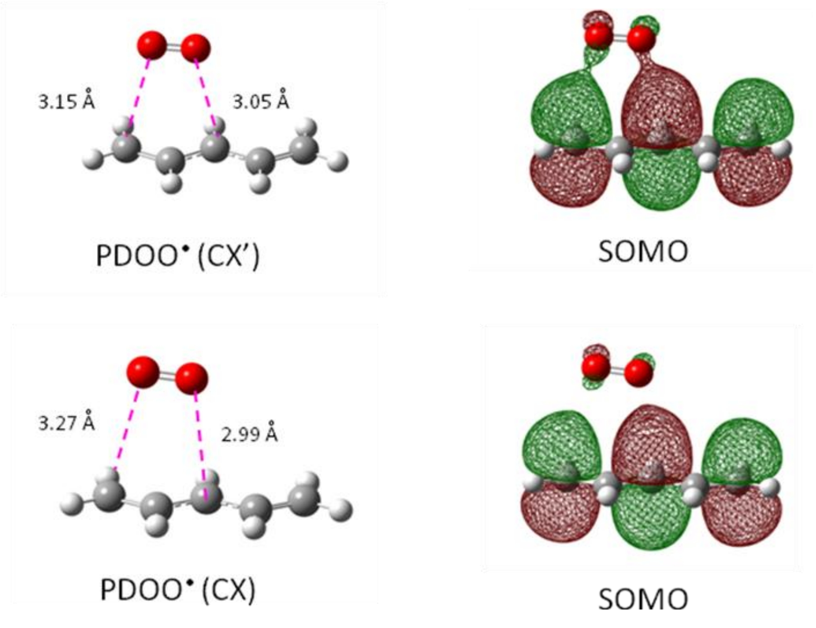

Figure 1.14 B3LYP/6-311+G(2df,p)-optimized complex $PDOO^{\bullet}$(**CX'**) and MP2/6-311+G(2df,p)-optimized complex $PDOO^{\bullet}$(**CX**).

In order to construct a complete potential energy surface for the addition of O_2 to the pentadienyl radical and the interconversion of the resultant pentadienylperoxyl radicals, we also calculated the structures and energies of the possible product pentadienylperoxyl radical conformations, and these are shown below in Figures 1.15 and 1.16.

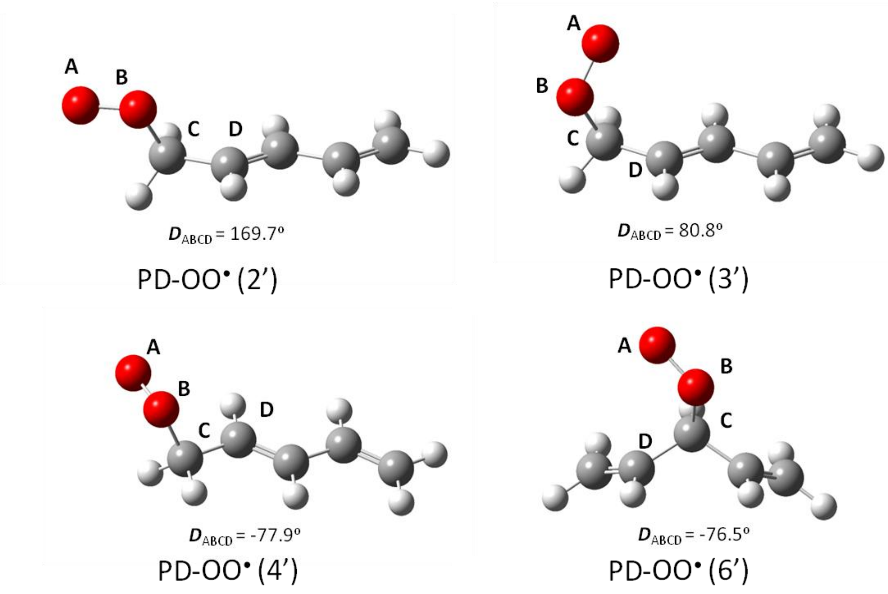

PD-OO• (2′) PD-OO• (3′)

PD-OO• (4′) PD-OO• (6′)

Figure 1.15 B3LYP/6-311+G(2df,p)-optimized structures of the low energy conformers of the pentadienyl radicals.

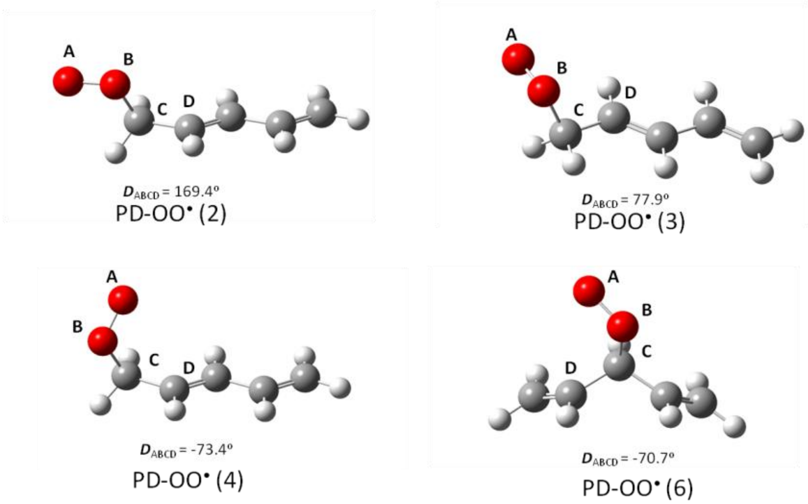

Figure 1.16 MP2/6-311+G(2df,p)-optimized structures of the low energy conformers of the pentadienyl radicals.

The overall potential energy surface for *anti* and *syn* addition of O_2 to the pentadienyl radical, and the interconversion of the pentadienylperoxyl isomers is depicted in Figure 1.17 and the relative enthalpies at all levels of theory studied here are included in Table 1.8.

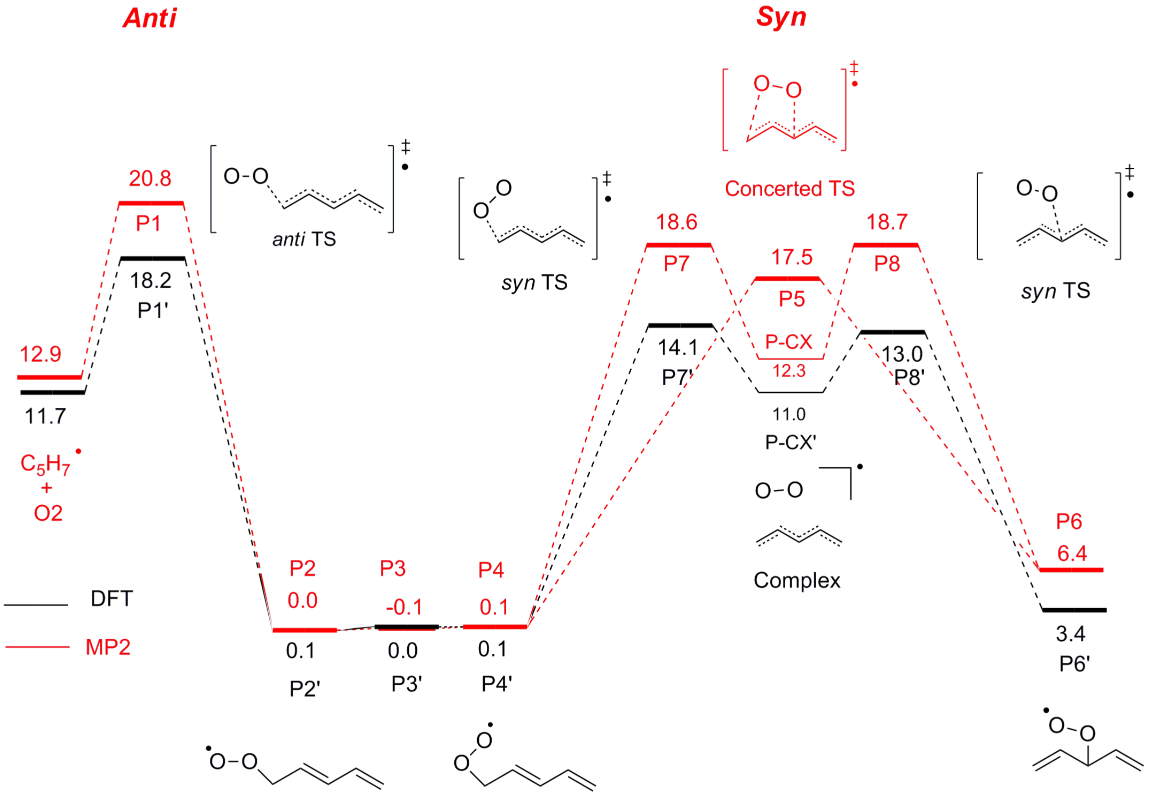

Figure 1.17 Schematic enthalpy profile for the addition of O_2 to the pentadienyl radical, and the rearrangement of the resulting conjugated and non-conjugated pentadienylperoxyl radicals (values in kcal/mol, determined by UCCSD(T)/6-311+G(2df,p) calculations at the UMP2/6-311+G(2df,p) and UB3LYP/6-311+G(2df,p) optimized geometries.

Table 1.8 Enthalpies (Δ*H*)in kcal/mol of ST, TS and CX for pentadienylperoxyl model calculated using UCCSD(T) and ROCCSD(T) at 6-311+G(2df,p) level on structures optimized using both B3LYP and MP2 at 6-311+G(2df,p) level.

Structures	***B3LYP***	***UCCSD(T)***	***RO CCSD(T)***	***Structures***	***MP2***	***UCCSD(T)***	***RO CCSD(T)***
C_5H_7•+ O_2	7.6	11.7	11.3	C_5H_7•+O_2	19.4	12.9	11.8
P1’	13.0	18.2	18.0	P1	42.0	20.8	20.0
P2’	0.3	0.1	0.2	P2	0.0	0.0	0.0
P3’	0.0	0.0	0.0	P3	- 0.1	-0.1	0.1
P4’	0.3	0.1	0.2	P4	0.1	0.0	0.1
				P5	19.0	17.5	17.0
P6’	6.5	3.4	3.7	P6	7.2	6.4	6.5
P7’	11.2	14.1	13.5	P7	19.0	18.6	17.4
P8’	12.0	13.0	12.9	P8	38.2	18.7	18.1
P-CX’	8.1	11.0	40.6	P-CX	18.9	12.3	41.1

1.4.2.3 Rate Constant of Peroxyl Fragmentation

The β-fragmentation rate constants of the allylperoxyl and pentadienylperoxyl radicals formed from O_2 addition to the allyl and pentadienyl radicals, respectively, were calculated using conventional transition state theory (Eq. 1.1)[44], with the MP2 and DFT-calculated partition functions and UCCSD(T) electronic energies corrected with the MP2 and DFT zero-point energies and are given in Table 1.9. In Eq. 1.2, k_B is the Boltzmann constant 1.38 x 10^{-23} J·K^{-1}, *h* is the Planck constant 6.62 x 10^{-34} J·s, *Q* is the partition function of DFT or MP2 optimized structures the and ΔE_0 is the zero-point electronic energy difference between the TS and the separated reactants.

$$k = \frac{k_B T}{h} \frac{Q_{TS}}{Q_{SM}} e^{\frac{-\Delta E_0}{RT}} \qquad \text{Eq.1.2}$$

Table 1.9 Calculated rate constants for the β-fragmentation of the allylperoxyl and pentadienylperoxyl radicals formed from O_2 addition to the allyl and pentadienyl radicals, respectively, and the corresponding rate constants for the same processes in the gas phase, as well as the solution phase values for mono- and polyunsaturated lipids for comparison.

Calculated Rate Constant (s^{-1})			Experimental Rate Constant (s^{-1})		
	B3LYP /CCSD(T)	MP2 /CCSD(T)		R=CH_3	R=H
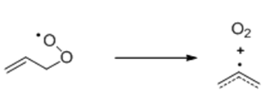	8.6 (*syn*) 0.0098 (*anti*)	N/A		3^{a1}	26^{b}
	319 (*syn*) 1.02 (*anti*)	0.09 (*syn*) 0.0052 (*anti*)	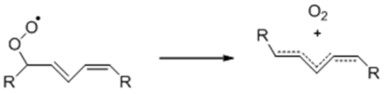	430^{a2}	138^{c}
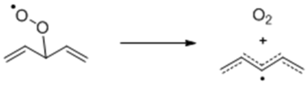	2.3×10^5	89	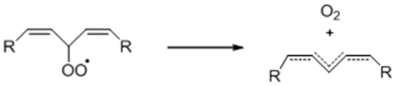	$2.4 \times 10^{6\,a3}$	N/A

[a1] taken from ref [24], [a2] taken from ref [46], [a3] taken from ref [47]
[b] taken from ref [48], [c] taken from ref [49]

1.5 Discussion

1.5.1 H-Atom Abstraction is A HAT Mechanism… or is it?

Recently, there has been much interest in the possibility of proton-coupled electron transfer (PCET) in formal H-atom transfer reactions.[50] PCET reactions are apparent H-atom transfer reactions wherein the proton of the H-atom and the electron of the H-atom are transferred between different pairs of orbitals. Several examples have been suggested, including the self-exchange reactions of phenols/phenoxyls[48] and oximes/iminoxyls [51], and the reactions of sulfenic acids with peroxyls,[51] as well as phenols with peroxyls,[52] the latter of which will be discussed in the subsequent chapter. We illustrate the phenomenon below using the self-exchange reactions of phenol/phenoxyl[50] and oxime/iminoxyl[53, 54] and the most relevant corresponding MOs are shown below.

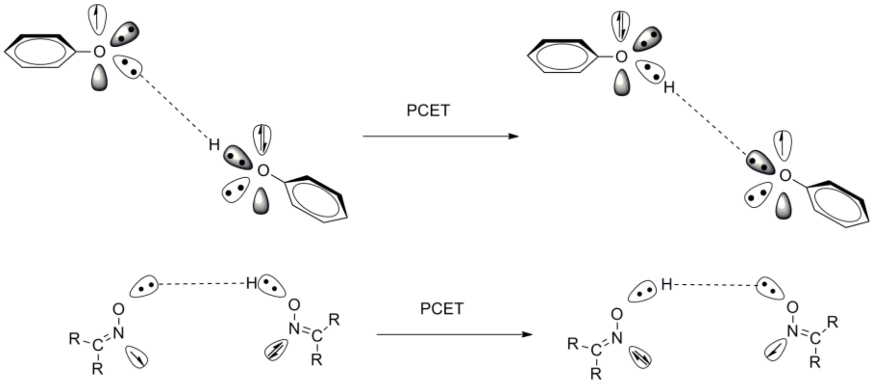

Scheme 1.11 Schematic representation of PCET in the self-exchange reactions of phenol/phenoxyl and oxime/iminoxyl.

As shown in Scheme 1.11, in the self-exchange reaction of phenols and phenoxyls, a pre-reaction complex is formed via hydrogen bonding (H-bonding) between the phenolic hydrogen and phenoxyl radical oxygen. This makes the the singly occupied molecular orbital (SOMO) of the phenoxyl radical perpendicular to the molecular framework, necessitating that the proton and electron are transferred between two different pairs of orbitals. That is, the proton is transfered along the H-bond to an O lone pair via the σ-orbitals of the two phenolic oxygens that are oriented in the plane of molecular framweork while an electron is transfered from the perpendicular HOMO of the phenol (shown only as the lone pair on the phenolic oxygen atom in Scheme 1.11, but also includes contributions due to the π-system of the aromatic ring) to the perpendicular SOMO of the phenoxyl radical (again, shown only as the unpaired electron on the phenoxyl oxygen atom in Scheme 1.11, but also includes contributions due to the π-system of the aromatic ring). In the self-exchange reaction of oximes and iminoxyls, a planar pre-reaction complex is again formed via H-bonding between the –OH group of the oxime and the O of the iminoxyl radical. However, unlike in the phenol/phenoxyl couple, both the electron transfer and the proton transfer occurs in the plane of the molecular framework, with the proton being transferred across the H-bond connecting the two terminal oxygen atoms, while an electron is transferred in the same direction between orbitals that are localized on the nitrogen atoms. This is termed a cyclic 5-centre PCET reaction.

One of the more interesting examples of a purported PCET reaction is the toluene/benzyl self-exchange reaction. Here, no H-bonded pre-reaction complex exists to enforce a geometry from which H-atom transfer cannot occur since there is no acidic hydrogen on the substrate. Regardless, since the π-stacking of the rings can enforce a *cisoid*-like geometry, the significant overlap between the phenyl moieties provides a conduit for electron transfer between the two rings while the proton is being transferred between the methylene moieties. These results inspired us to look at whether PCET may play a role in the mechanism of H-atom abstraction from allylic positions of monoenes and bis-allylic positions of lipid dienes, representatives of monounsaturated and polyunsaturated lipids, respectively. Here, overlap between the alkene π HOMO and the peroxyl π SOMO would be required to favour the *cisoid* geometry and provide a conduit for electron transfer chemistry (Scheme 1.12).

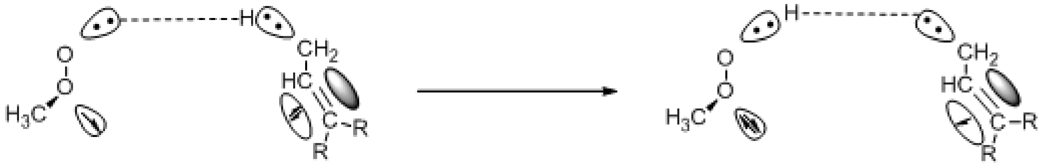

Scheme 1.12 Schematic representation of possible PCET in the formal H-atom transfer reaction between methylperoxyl radical and propene.

Surprisingly to us, there have been no detailed theoretical studies of this reaction, the closest being the work of Siegbahn and co-workers,[55] who considered the reactions of polyunsaturated lipids with hydroxyl radicals. While this may indeed serve as an initiating reaction, we argue that it is far less important than the rate-limiting propagation step in lipid autoxidation. In contrast to the reaction of hydroxyl radicals with lipids, our calculated results show that H-atom abstraction from propene and pentadiene, models of mono- and polyunsaturated lipids, respectively, by methylperoxyl, a model of the chain-carrying lipid peroxyl radical, is not a simple HAT process. Indeed, it is similar to the benzyl/toluene self-exchange reaction in that, while it proceeds without a H-bonded pre-reaction complex, the preferred TS structure indicates that there is an overlap between the peroxyl π* SOMO and propene π HOMO. Because of this overlap, a portion of the electron density is delocalized from the alkene π orbital to the peroxyl π* orbital and thus the double bond is oxidized as the peroxyl radical is reduced while the proton is moving between the σ bonds. Unfortunately, it is difficult to design an experiment that could be readily carried out that would distinguish between the two possibilities, which is an issue with distinguishing between PCET and HAT mechanisms, in general.

1.5.2 Predicting the Oxidizability of Lipids

Propagation rate constants, k_p, for the autoxidation of various hydrocarbons are available in the literature due to extensive studies on the subject in the 1960s and 1970s using the rotating sector technique which, to the best of our knowledge, is no longer practiced.[45] This has prompted the development of indirect kinetic methods for their evaluation as well as the development of computational approaches for their estimation.[29] In particular, Pratt, et al. [27] has reported a linear correlation between the calculated BDEs of various hydrocarbons and the k_ps available in the literature, and has shown that this can be used to estimate the k_p of hydrocarbons for which no experimental data exists. As part of the current study we have calculated k_p directly, and as a result, this approach is likely to prove superior for estimating k_p than simply calculating BDEs, as it takes into account the energetics of the transition states for the reactions, as opposed to only their thermochemistry.

It should be pointed out that the calculations, shown in Table 1.5, suggest that lipids containing a conjugated diene moiety do not oxidize significantly more readily than monounsaturated lipids. Unfortunately, there is currently no experimental value of k_p with which we can corroborate this data. Given the fact that conjugated linoleic acid is proving to be a lipid of increasing relevance in human health, our results suggest that this should be further investigated.[13]

1.5.3 Oxygen Addition and Peroxyl Radical Rearrangement Occurs via a Radical:Dioxygen Complex

The allyl and pentadienyl radicals that are formed as a result of the HAT/PCET process discussed above possess unpaired electron spin density at multiple centers. In the allyl radical, the spin density is split equally between the two terminal carbon atoms, whereas in the pentadienyl radical, roughly 65% of the spin density is split equally between the two terminal carbon atoms, while 35% resides on the central carbon atom. We first considered addition to the allyl radical.

Two modes of addition of O_2 to the allyl radical were identified using B3LYP: *anti* and *syn*. In contrast, only a single mode of O_2 addition to the allyl radical was identified using MP2, that which possesses an *anti* geometry. A TS structure similar to the B3LYP *syn* structure was identified, but the single negative vibrational mode that characterizes the TS has atomic displacements that are consistent with a concerted rearrangement of the allylperoxyl radical (*vide infra*) as opposed to simply C-O bond forming. It is likely that the TS structure is not symmetric, as we might expect for such a degenerate rearrangement, because this area of the potential energy surface is quite flat, and that the calculation converged before reaching the top of the saddle point.

The results of the B3LYP calculations – and CCSD(T) single point energies based on the geometries calculated by B3LYP – suggest that the *syn* pathway is that which is taken by O_2. Upon consideration of the calculated MOs for the *syn* and *anti* TS structures, the only significant difference between them is the interaction of the formally non-bonding π SOMO of the allyl radical with one of the π* SOMOs of O_2 (Figure 1.7). This interaction leads to a barrierless addition of O_2 to the allyl radical by the *syn* pathway while the *anti* pathway requires transmission of a barrier that lies 3.5-4 kcal/mol higher in enthalpy than the separated reactants.

Intrinsic reaction coordinate calculations suggest that the *syn* TS structure connects the allylperoxyl radical with a weakly bound allyl:dioxygen complex. Since DFT struggles with dispersion interactions, such as those which are holding the complex together, it is perhaps not surprising that the interaction energy is worth only 0.9 kcal/mol, and this is completely erased by thermochemical corrections, which put the complex at +0.2 kcal/mol in enthalpy relative to the separated reactants. The UCCSD(T) single point energy calculations suggest a larger interaction energy of 1.6 kcal/mol, which leads to an enthalpy that is 0.5 kcal/mol lower than allyl• + O_2 (Table 1.7), however this is probably still underestimated because the CCSD(T) calculations are carried out on the DFT minimum energy geometries, which are likely to be quite a bit higher in energy than the CCSD(T) minimum energy geometries. Unfortunately, large basis set geometry optimizations (and vibrational frequency calculations) on a system of this size are not possible with our computational resources. Calculations by Olivella and Sole[43] at the CASPT2 level, which take into account the multiconfigurational character of the reference wave function and both non-dynamical and dynamical electron correlation effects, predict an interaction energy of 2.7 kcal/mol, which is likely to be a much better estimate.

The reaction of the allyl radical with dioxygen was studied in the gas phase in 1991 by Bayes and co-workers. From measurement of the temperature dependence of the equilibrium constant for the reaction, they calculated the C-OO• bond dissociation enthalpy of the allylperoxyl radical to be 18.2±0.5 kcal/mol.[56] Our calculated results, which range from 16.2-16.7 kcal/mol are in excellent agreement with these results. From their equilibrium constant, Bayes and co-workers derived a β-fragmentation rate constant of 26 s^{-1} at 348 K.[48] Our calculated rate constants via the *syn* and *anti* TS structures are 8.6 and 9.8 x 10^{-3} s^{-1}, at 298 K respectively. Given the temperature difference, the agreement is excellent for the *syn* structure, strongly supporting our supposition that this is how the reaction proceeds.

The rearrangement of the allylperoxyl radical has been a controversial issue for some time. As mentioned in the introduction, previous computational work by Olevilla and Sole, which was based on the same MP2/6-311+G(3df,2p) approach followed by CCSD(T) single point energy calculations as we have employed here, suggested that the rearrangement was step-wise. However, as we have shown (as had they, but they misinterpreted their data), there is no *syn* TS structure that connects the allylperoxyl radical to the allyl:dioxygen complex – only the *anti* TS structure which we have discussed above. Furthermore, the TS structure for the concerted process calculated by OS was not the correct structure. Using the same theoretical approach, we discovered a lower energy transition state geometry for the concerted rearrangement. After zero point energy corrections, this structure has a lower UMP2/6-311+G(3df,2p) energy of 3.0 kcal/mol, and lower UCCSD(T) and ROCCSD(T) energies of 7.9 and 8.0 kcal/mol, respectively compared to the structure that OS had located. These revisions to the MP2 results, taken together, suggest that the allylperoxyl rearrangement is a concerted process and not step-wise. In contrast, no concerted TS structure could be located using B3LYP, and a step-wise rearrangement via a bound allyl:dioxygen complex is predicted. Given the excellent agreement between the B3LYP-derived results and the experimental data for both the C-OO BDE of the allylperoxyl radical *and more importantly its β-fragmentation rate constant*, we believe that a step-wise rearrangement is more likely.

Perhaps the more important model is that of polyunsaturated lipids, since they are more easily oxidized and result in a more complicated product distribution since unpaired electron spin density is found now at both the terminal carbon atoms as well as the central carbon atom. We will begin with the terminal addition, which bears a closer resemblance to the addition of O_2 to the allyl radical.

Using the B3LYP method, two modes of O_2 addition to the terminal carbon atom of the pentadienyl radical were detected: *syn* and *anti*. To our surprise, in contrast with the calculated results for the addition of O_2 to the allyl radical, MP2 also identified TS structures for these two modes of O_2 additon. The *syn* TS structures are lower energy by both methods, owing to the interaction of the π SOMO of the pentadienyl radical and one of the π^* SOMOs of the O_2. This is the same type of interaction that leads to a lower energy for the *syn* TS in the addition of O_2 to the allyl radical. The DFT calculations suggest a small enthalpic cost of 2.4 kcal/mol for the *syn* addition of O_2, which is far more realistic than the 6.5 kcal/mol predicted for the *anti* structure. The fact that the MP2 calculations suggest larger enthalpies of activation of 5.7 and 7.9 kcal/mol for the *syn* and *anti* pathways, respectively, argues that the DFT structures are more consistent with experiment. Similar to our calculations of the addition of O_2 to allyl, IRC calculations indicate that the TS structures for *syn* addition connect the product pentadienylperoxyl structures with a pentadienyl-peroxyl complex.

The reaction of the pentadienyl radical with dioxygen was studied in the gas phase in 2001 by Washida and co-workers. From measurements of the temperature-dependence of the equilibrium constant for the reaction, they calculated the C-OO• bond dissociation enthalpy of the pentadienylperoxyl radical to be 13.4±1.2 kcal/mol.[49] Our calculated results, which range from 11.3-12.9 kcal/mol are in good agreement with these results. Recall that our calculated C-H BDEs for 1,3-and 1,4-pentadiene are also underestimated with respect to experimental values suggesting that theory overestimates the stability of the pentadienyl radical. From their equilibrium constant at 298 K, Washida and co-workers derived a β-fragmentation rate constant of 138 s^{-1}. Our calculated rate constants via the DFT-calculated *syn* and *anti* TS structures are 319 and 1.02 s^{-1}, respectively(Table 1.9). Again, the much better correspondence between the predictions based on the *syn* TS structure and the experimental data suggest that this is the mode of O_2 addition to the terminal positions of the pentadienyl radical. It should be pointed out that while we were able to find both *syn* and *anti* TS structures for the addition/fragmentation by MP2, the CCSD(T) calculated barriers lead to predicted k_β values of 1.8 and 0.005 s^{-1}, respectively, in much poorer agreement with experiment, further supporting that the DFT structures are better representations of the goings on.

1.5.4 Understanding Product Distributions in Lipid Peroxidation

While we were carrying out the calculations described above, Tallman, et al. [29] reported the results of experimental studies of substituent effects on the regioselectivity of the autoxidation of non-conjugated dienes. In these experiments, they found that: 1) increasing size of the substituents at C-1 and C-5 of the diene favors kinetic products arising from oxygen addition at the nonconjugated position, C-3, of the pentadienyl radical intermediate and, 2) substituents at C-1 or C-5 of the pentadienyl radical have a significant effect on the regioselectivity of the formation of the conjugated diene hydroperoxides, with larger substituents directing oxygen addition to the pentadienyl radical at the site of least steric hindrance. It would be interesting to extend our calculations to help understand these preferences, as well as other documents in the past literature.

A particularly interesting result from the recent paper by Tallman et al. [29] was that oxidations of *cis,cis*-6,9-pentadecadiene lead to twice as much *cis,trans*-hydroperoxide as opposed to the *trans,trans*-hydroperoxide, the latter of which would be expected to predominate on the basis of thermodynamic considerations. In order to rationalize these observations, as well as the others in their work, they suggested that the addition of O_2 to the pentadienyl moiety via a TS wherein the dioxygen moiety is oriented *anti* to the substituent on the terminal carbon is lower in energy than the *gauche* structure as shown in Scheme 1.13.[29] While this seems entirely reasonable, there has been no evidence for the types of TS structures suggested by Tallman et al. – i.e. those with the dioxygen moiety *syn* to the diene fragment – until now.

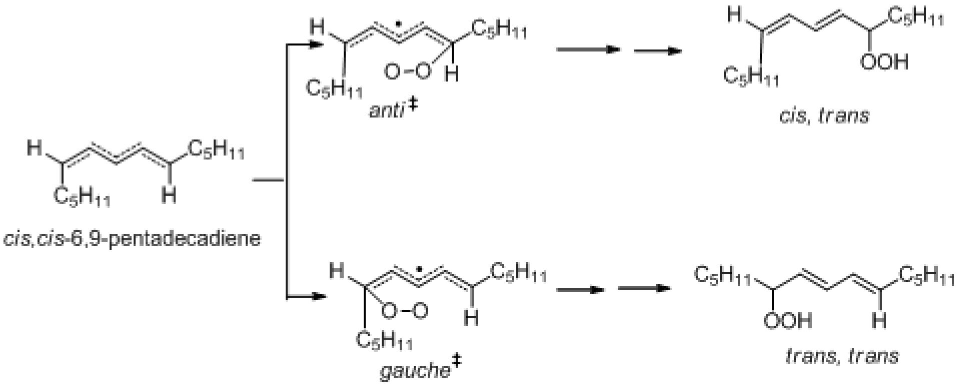

Scheme 1.13 Proposed mechanism of O_2 addition of a lipid based on experimental studies.[29]

1.6 Conclusions and Outlook

Calculations of the transition states for H-atom abstraction from models of unsaturated lipids by models of lipid-derived peroxyl radicals show that, independent of methodology, they are predicted to occcur via a cyclic transition state due to interactions between the π^* and π orbitals of the peroxyl radical and vinyl moiety of the lipid, respectively. These results suggest that the reaction cannot be described as a simple H-atom transfer mechanism, but can also be described as a proton-coupled electron transfer mechanism. Calculations of rate constants for these reactions using the methodology described herein may prove useful for the estimation of propagation rate constants for the autoxidation hydrocarbons for which experimental values are currently unavailable.

Similarly, independent of methodology, calculations of the oxygen addition step of hydrocarbon autoxidation showed that interactions between the π (SOMO) orbitals of dioxygen and the delocalized carbon-centered radical derived from the lipid (allyl, pentadienyl) reduce the activation barrier so that oxygen addition occurs in a *syn* fashion from allyl:dioxygen and pentadienyl:dioxygen complexes, respectively. These results also lead to the conclusion that the interconversion of allylperoxyl and pentdienylperoxyl radicals occurs in a step-wise fashion. We are currently pursuing calculations of terminally dimethylated analogs to provide models that more closely approximate the unsaturated lipid substrates of autoxidation *in vivo*.

Chapter 2

The Role of Protic Solvents in the Catalysis of Reactions of Phenol and Peroxyl Radicals

2.1 Introduction

2.1.1 Background and Significance

Phenols are the prototypical radical-trapping antioxidants, and are employed in nature and also in industry to guard lipids and other hydrocarbons against radical-mediated autoxidation. In humans, the most abundant lipid-soluble antioxidant is α-tocopherol, the most reactive form of Vitamin E. Vitamin E is acquired from our diet, which is also how we acquire a whole host of phenolic compounds that are believed to impart protection from radical-mediated damage, and therefore serve preventive roles in maintaining good health and providing defense against the many degenerative diseases that are believed to be related to autoxidation. Some of the other famous examples include α-tocopherol from Vitamine E, hydroquinones, such as ubiquinol (coenzyme Q_{10}), catechols, such as the polyphenolic flavonoids epicatechin found in green tea and hydroxytyrosol from olives, and resorcinols, such as the resveratrol found in grapes (Scheme 2.1).

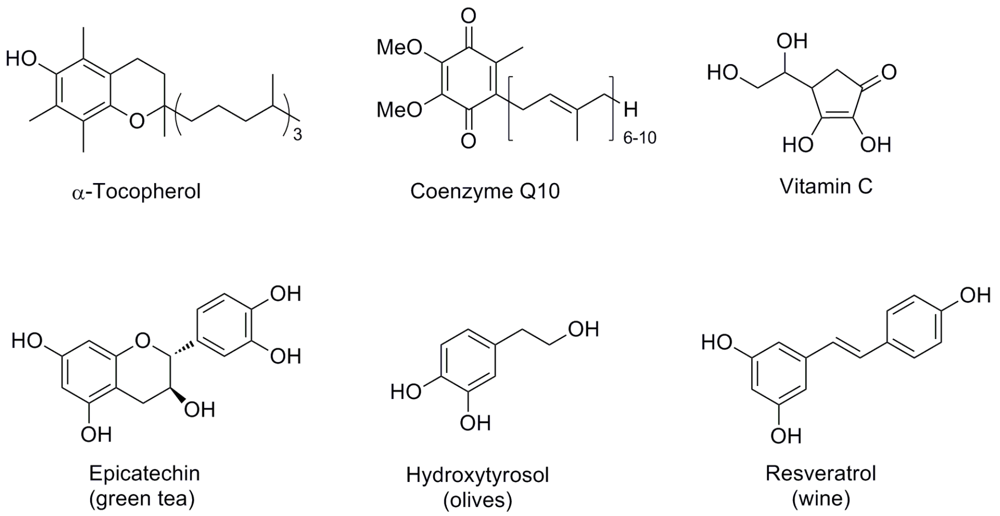

Scheme 2.1 Common antioxidants.

2.1.2 Mechanistic Considerations

The mechanism by which phenolic species slow the autoxidation of hydrocarbons is shown in Scheme 2.1. Overall, a phenolic antioxidant (ArOH) inhibits autoxidation by formally transferring the phenolic H-atom to a chain-carrying substrate-derived peroxyl radical (ROO•) to form a hydroperoxide, and an aryloxyl radical (ArO•) which can react with another peroxyl radical to yield non-radical products. The first step of H-atom transfer to a lipid peroxyl is the rate limiting step; its rate is represented by k_{inh}. What makes phenol a good antioxidant is not only because it is able to transfer a H-atom very rapidly, but also because the aryloxyl radical that is then formed is sufficiently thermodynamically stable and/or kinetically persistent that it is unreactive to oxygen or the substrate. Thus, it is possible for the phenol to break two radical chains: the first by Eq. 2.1 and the second by Eq. 2.2.

$$\mathrm{ROO}^{\bullet} + \mathrm{ArOH} \xrightarrow{k_{\mathrm{inh}}} \mathrm{ROOH} + \mathrm{ArO}^{\bullet} \qquad \text{Eq. 2.1}$$

$$\mathrm{ROO}^{\bullet} + \mathrm{ArO}^{\bullet} \xrightarrow{fast} \text{Non-radical products} \qquad \text{Eq. 2.2}$$

Scheme 2.2 Mechanism of peroxyl radical-trapping phenolic antioxidants.

The efficiency of ArOH in protecting a substrate from autoxidation is dependent on the substrate. If the substrate (RH) is easily oxidized, such that the propagation step of the reaction of $\mathrm{ROO}^{\bullet}$ with substrate is faster than the step of ArOH quenching $\mathrm{ROO}^{\bullet}$, e.g k_{p} is several orders larger than k_{inh}, then the ArOH is not efficient enough to inhibit the autoxidation. Therefore, substrates that are difficult to oxidize can be protected by relatively less efficient antioxidants and vice versa. Since the polyunsaturated lipids that are abundant in the cell membranes and lipoproteins of our cells are relatively easily oxidized, we require highly reactive antioxidants for their protection, such as α-tocopherol.

The reactivity of a phenolic antioxidant is dependent on the bond dissociation enthalpy (BDE) of the phenolic O-H bond. Phenol itself has an O-H BDE of 87 kcal/mol,[57] which makes the reaction of phenol with a peroxyl radical thermoneutral, since the O-H BDE in a hydroperoxide is essentially the same.[58] An increase in the electron density in the aromatic ring weakens the BDE of O-H by stabilizing the electron deficient phenoxyl radical, and subsequently makes it a more efficient antioxidant. Therefore, phenols that are substituted with electron-donating groups are generally the most reactive. For example, the substituents on the phenolic ring of α-tocopherol lower the phenolic O-H BDE by 10 kcal/mol,[59] which brings about an increase in the rate of the reaction with peroxyl radicals of about three orders of magnitude, from 3×10^{3} $M^{-1}s^{-1}$[59] for phenol in isooctane to 3×10^{6} $M^{-1}s^{-1}$ in benzene.[60] New generation antioxidants, such as substituted 5-pyrimidinol[47, 61] and 3-pyridinol[50, 62-64] derivatives (examples shown in Scheme 2.3) have been developed as more stable molecules to air oxidation and more active scavengers towards chain-carrying peroxyl radicals.[65]

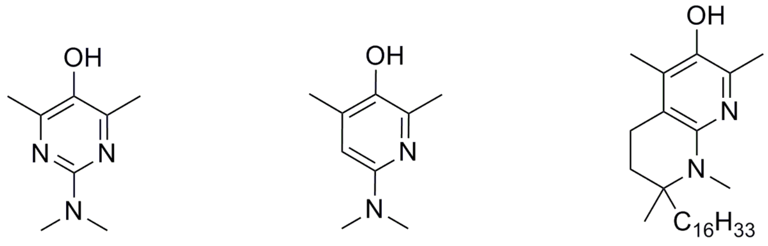

1 2 3

Scheme 2.3 Next generation phenolic antioxidants: 5-pyrimidinols and 3-pyridinols.

The mechanism of the formal H-atom transfer from a phenolic antioxidant to a chain-carrying peroxyl radical was first thought to be a hydrogen atom transfer (HAT) based on deuterium kinetic isotope effect studies. Recent theoretical work, on the other hand, suggests a proton coupled electron transfer (PCET) mechanism.[50] The most important difference between PCET and HAT is that in a PCET process, a proton and an electron are transferred between different pairs of molecular orbitals, whereas in HAT a proton and an electron are transferred together as a H-atom between a single pair of orbitals (Scheme 2.4). PCET is an interesting mechanism because H-atom transfer is one of the most fundamentally important reactions, and plays a particularly important role in biology, e.g. in the reduction of ribonucleotides,[66-68] and oxygen utilization and production in cytochrome *c* oxidase (C*c*O) and in photosystem (II) (PSII), respectively.[69-73]

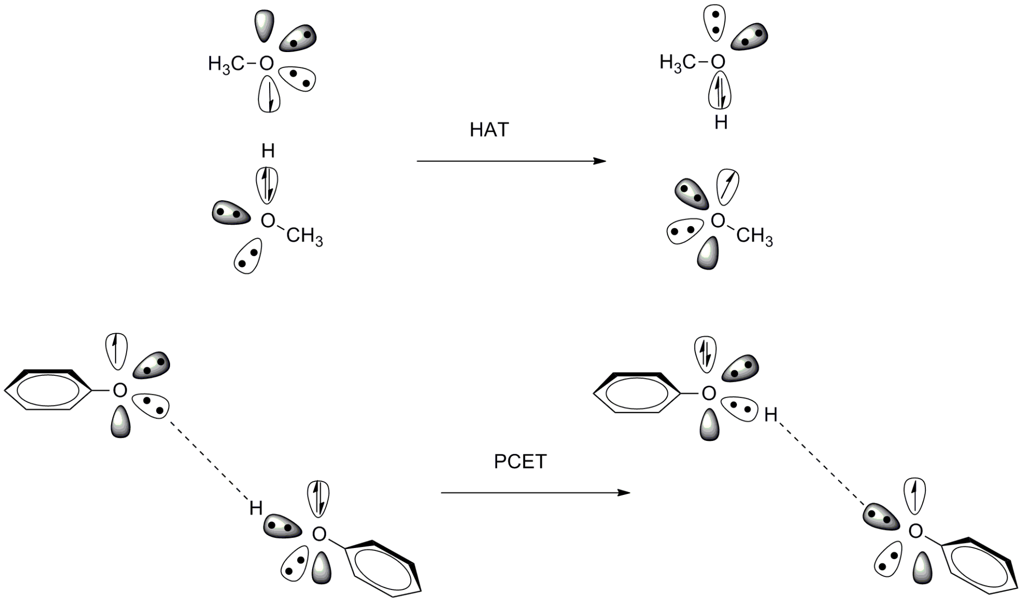

Scheme 2.4 Hydrogen atom transfer mechanism of methanol/methoxyl versus proton coupled electron transfer mechanism of phenol/phenoxyl.[75]

Mayer and Borden et al.[50] first performed calculations on the self-exchange reactions of methanol/methoxyl and phenol/phenoxyl to illustrate the difference between HAT and PCET (Scheme 2.4). In the methanol/methoxyl reaction, there is no pre-reaction complex formed. One electron and one proton travel synchronously in the σ-orbital formed by the lone pairs of oxygen. In contrast in the phenol/phenoxyl self-exchange reaction, before H-atom transfer happens, a pre-reaction complex is formed by hydrogen bonding (H-bonding) between the phenolic hydrogen and phenoxyl radical oxygen. During the TS, the complex is nearly planar. Phenolic proton transfers along the H-bond to an O lone pair via the σ-orbitals of the two phenolic oxygens that are oriented in a plane. An electron transfers at the same time as the proton, in the same direction, from the perpendicular lone pair of oxygen to the perpendicular SOMO of phenoxyl oxygen via 2p-π orbital overlapping. If it was a HAT mechanism, suggested by Mayer, et al.[50], a H-bond had to be broken for H-atom to transfer and the phenolic –OH would be re-directed towards the SOMO of phenolic oxygen. PCET is overall energetically favored over HAT.

H-atom transfer between a peroxyl and phenol was first studied theoretically by Popelier, et al.[76] It was found, using atoms in molecules (AIM) approach, from reactants to transition state, the hydrogen atom lost volume, electronic population and dipole moment, indicating the H-atom transfer was a PCET mechanism. DiLabio and Johnson[77] also predicted mechanisms for H-atom transfer of *tert*-butylperoxyl plus phenol. From the calculated results, a H-bonded pre-reaction complex was formed between the O-H group of phenol and a lone pair on the terminal oxygen of peroxyl. Also, based on the calculated HOMO and SOMO, there is an overlapping between the π-orbital of phenol and 2p orbital of terminal oxygen of the peroxyl radical. From all above, it was concluded both reactions occur following PCET mechanism from theoretical studies.

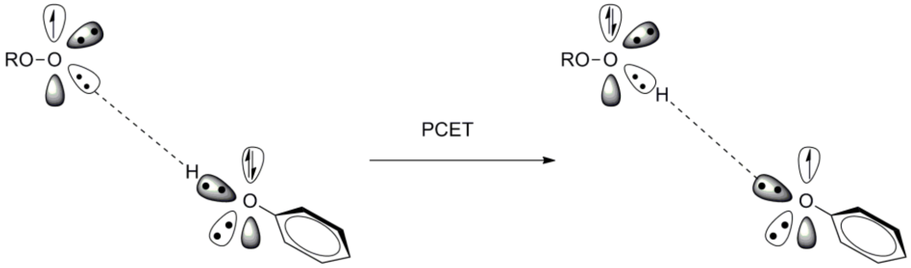

Scheme 2.5 H-atom transfer between a peroxyl and a phenol.

2.1.3 Kinetic Solvent Effects

Despite the fact that the reaction between phenols and peroxyl radicals are formally radical reactions, involving no formal charges or charge separation, they are subject to very significant solvent effects, in particular, due to hydrogen-bonding. Ingold and coworkers [75, 78] have demonstrated the importance of H-bonding between phenol and solvent or other H-bond acceptors in the medium on the kinetics of these reactions.

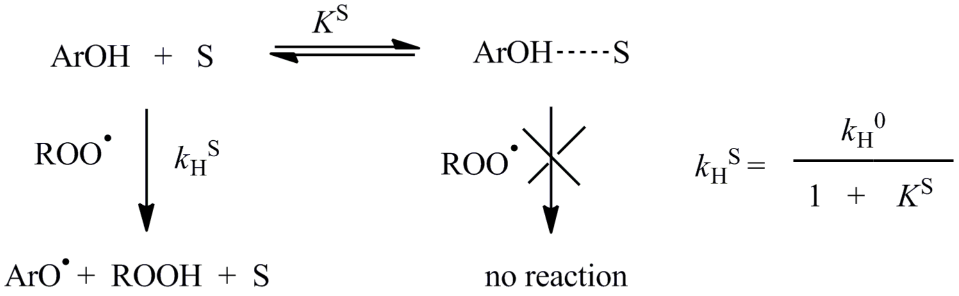

Scheme 2.6 Kinetic solvent effect on the reaction of phenols with peroxyl radicals.[79]

As shown in Scheme 2.6, solvents with strong hydrogen bond acceptors, such as those containing carbonyl or nitrile functional groups, tend to slow the rate of hydrogen donation of phenolic antioxidants.[80]

The solvent-phenol relationship is also described in Eq. 2.6. In this equation, the effect of a solvent on phenol radical trapping ability can be quantified by relating the rate constant for the reaction of a phenol with a radical Y• in any solvent ($k^S_{(ArOH;Y\bullet)}$) to the rate constant in a solvent that cannot accept hydrogen-bonds ($k^0_{(ArOH;Y\bullet)}$) and the product of the hydrogen-bond-accepting (HBA) ability of the medium and the hydrogen-bond donating (HBD) ability of the phenol, which are given by the Abraham parameters β_H^2 and α_H^2, respectively.[81]

$$\log k^{S}_{(\mathrm{ArOH;Y\bullet})} = \log k^{0}_{(\mathrm{ArOH;Y\bullet})} - 8.3\ \alpha_H^2\ \beta_H^2 \qquad \text{Eq. 2.6}$$

This equation was originally developed to understand the kinetic solvent effects for the reactions of phenols with alkoxyl radicals and hydrazyl radicals (i.e. dpph•).[82] Recently the equation was demonstrated to also account for the kinetic solvent effect on the reactions of phenols with peroxyl radicals by Jha and Pratt.[79]

Alcoholic solvents, good HBA, display a different type of solvent effect from previously stated. Rather than slowing the reaction of phenols and peroxyl radicals via the alcohol's ability to act as a H-bond acceptor with the phenol, it was reported by Ingold and co-workers[75, 78] that when in alcoholic solvents, an abnormally enhanced values of $k^{S}_{(\mathrm{ArOH;Y^\bullet})}$ was observed. It was proposed that this enhancement of rates was raised from the mechanism of H-atom transfer in a step-wise process called sequential proton loss electron transfer (SPLET), in which a proton transfers from the phenol to the solvent and then electron quickly transfers from phenoxide anion to the radical, sequentially the proton transfers from the solvent to the newly formed anion, originated from the radical (Scheme 2.8).

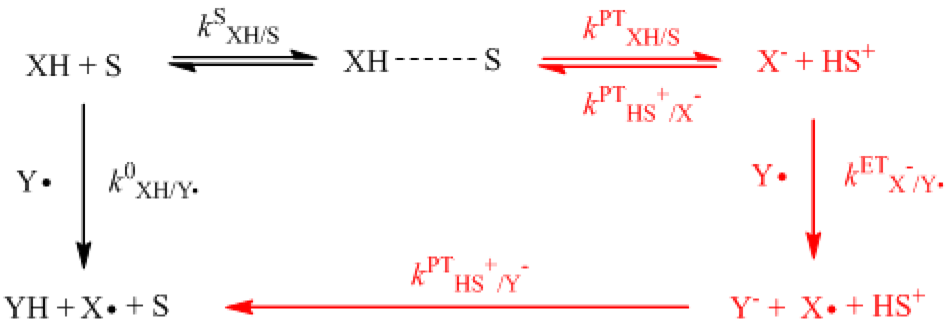

Scheme 2.7 SPLET mechanism in red versus HAT mechanism in black.[75]

Recently, it is surprising that studies by Valgimigli, et al.[83] demonstrated that in the presence of small amounts of acids, including acetic acid, HCl, *p*-toluenesulfonic acid, or trichloroacetic acid, a dramatic acceleration of the rate of reactions between phenols and chain-carrying peroxyl radicals occurs. Of the acids surveyed, acetic acid was found to be the most efficient catalyst.

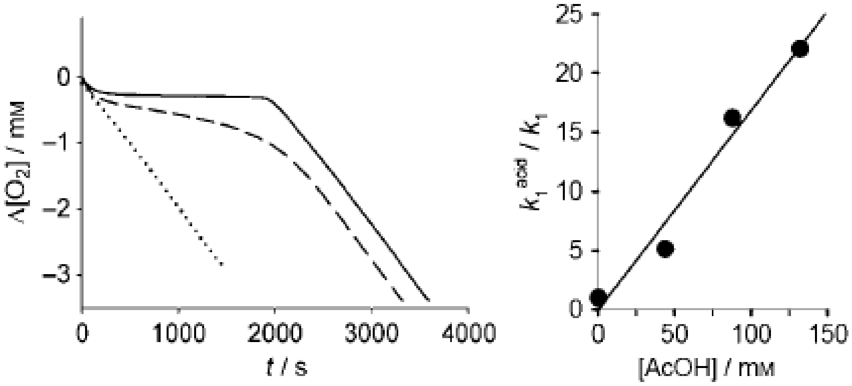

Figure 2.1 (Left) oxygen consumption at 303 K during the autoxidation of styrene (4.3 M) in CH_3CN (dotted line), and when the reaction is inhibited by pentamethylchromanol (1.25 μM) in absence (dashed line) or presence (solid line) of AcOH (88mM); (right) dependence of k_1 on the concentration of the acid.[83]

Experimental results are shown in Figure 2.1. With no antioxidant present in the reaction, oxygen was consumed by styrene autoxidation over time (dotted line). In the presence of 1.25 μM antioxidant pentamethylchrmanol, but without any acid, the rate of oxygen consumption was slower, but oxygen was still consumed over time. In the presence of 88 mM AcOH, together with pentamethylchrmanol, autoxidation of styrene was completely inhibited for the first 2000 s. It was reported that this effect corresponded to a more than 16-fold increase in k_1, the rate constant of autoxidation inhibition. The figure on the right side of Figure 2.1 showed that k_1 in the presence of AcOH/ k_1 in the absence of AcOH increased linearly as the concentration of AcOH increased in the reaction.

This result by Valgimigli, et al is the opposite of what has been previously reported that solvents with strong HBA are capable of slowing down the inhibition of autoxidation,[75, 78] suggesting the inhibition of autoxidation with the presence of acid must be operating by another mechanism.

2.2 Objective

Various results have been reported for solvent assisted inhibition of autoxidation by antioxidant. Most solvents that are good HBA slow down the inhibition process, but acidic and alcoholic solvents demonstrate acceleration in the rate of inhibition. These contradictory results imply that there must be another mechanism different from the previously reported ones that is operating. In the current study, we used computational methods to attempt to understand the acceleration in rate associated with protic acids, as well as alcohols. Although alcohols are not the same as acids, they still serve as good proton donors and acceptors, and the same towards water. Therefore, acids, alcohols and water are the three types of solvents investigated.

We propose that for each solvent, there can be three modes of interaction with the system occurring (Scheme 2.8): A) solvent serves as a H-bond donor to the phenolic oxygen of phenol, B) solvent serves as a H-bond donor to the terminal oxygen of methylperoxyl and C) solvent serves a H-bond donor and acceptor to both phenol and methylperoxyl.

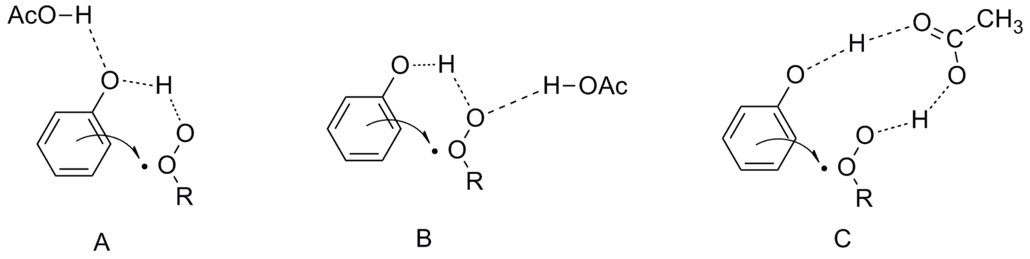

Scheme 2.8 Three modes of solvent (acetic acid as an example) interaction with the system.

2.3 Methodology

For all of the calculations reported here, phenol was used as a model compound for antioxidant. Methylperoxyl, the simplest alkylperoxyl radical, was used as a model compound for the chain-carrying lipid peroxyl radicals. The structures of the starting materials and the transition states were optimized using B3LYP with 6-311++G(2d,2p) basis set. All stationary points were characterized as minima (all positive frequencies) or transition states (single negative frequency with appropriate atomic displacements) on the potential energy surface by vibrational frequency calculations.

All calculations were performed with the Gaussian 03 suite of programs compiled to run on Sun Microsystems SunFire 25000 or Enterprise M9000 servers with UltraSPARC-IV+ or Sparc64 VII CPUs, respectively.

2.4 Results

2.4.1 Transition State Structures

Two transition state (TS) structures for the abstraction of a H-atom from phenol by the methylperoxyl radical were identified using B3LYP/6-311++G(2d,2p) and are shown in Figure 2.2. Relevant bond lengths, angles and dihedral angles are also shown for comparison. The lowest energy transition state we denote as *cisoid* (top) since the substituents on the oxygen atoms between which the H-atom is being transferred are *syn* to each other (making the dihedral angle close to zero). In contrast, we denote the second transition structure *transoid* (bottom), since the substituents on oxygen atoms between which the H-atom is being transferred are *anti* to each other (making the dihedral angle closer to 180^{o}.

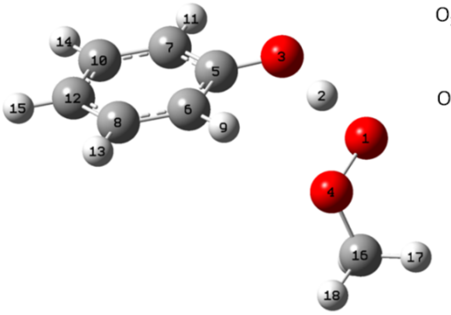

Bond (Å)		Angle (°)		Dihedral angle (°)	
O_3-O_1	2.37	C_6··C_5··O_3	122.4	C_5··O_3··O_1··O_4	-8.0
O_4-C_5	3.44	C_5··O_3··O_1	119.6		
		O_3··O_1 ·O_4	107.5		
		O_1··O_4··O_{16}	108.3		

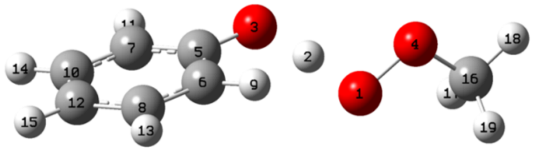

Bond (Å)		Angle (°)		Dihedral angle (°)	
O_3-O_1	2.37	C_6··C_5··O_3	121.9	C_5··O_3··O_1··O_4	-151.8
O_4-C_5	4.09	C_5··O_3··O_1	113.9		
		O_3··O_1 ·O_4	105.8		
		O_1··O_4··O_{16}	108.4		

Figure 2.2 B3LYP/6-311++G(2d,2p) optimized structures of the *cisoid* (top) and *transoid* (bottom) transition states of the reaction of phenol with methylperoxyl.

The incorporation of formic acid into the model was studied in three different configurations – with the formic acid serving as a H-bond donor to phenolic oxygen atom, with formic acid serving as a H-bond donor to the terminal oxygen atom of the peroxyl radical, and with formic acid serving as both H-bond acceptor to the phenol and H-bond donor to the terminal oxygen of the peroxyl radical. The two (*cisoid* and *transoid*) transition state structures for each of these configurations are shown in Figures

2.3, 2.4 and 2.5, respectively, along with relevant bond lengths, angles and dihedral angles for ease of comparison.

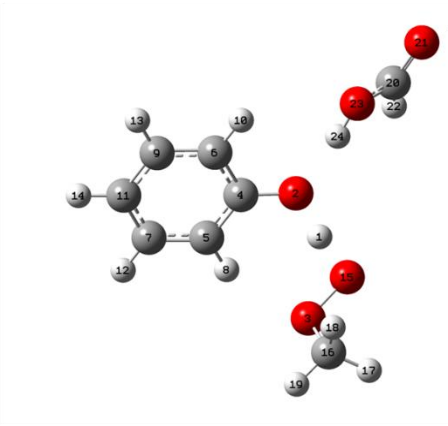

Bond (Å)		Angle (°)		Dihedral angle (°)	
O_2-O_{23}	2.77	C_5··C_4··O_2	121.2	C_5··O_3··O_1··O_4	5.5
O_2-O_{15}	2.37	C_4··O_2··O_{12}	117.7		
O_{15} –O_{23}	4.25	O_2··O_{15} ·O_3	106.7		
O_3 – C_4	3.38	O_{23}··O_2··O_{12}	111.3		
		O_{15}··O_3··C_{16}	108.7		
		C_4··O_2··O_{23}	118.8		

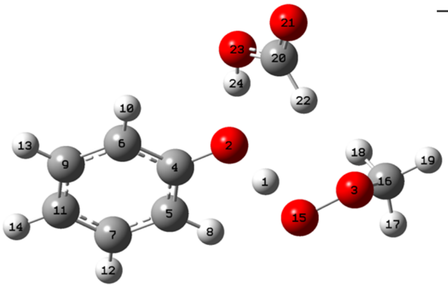

Bond (Å)		Angle (°)		Dihedral angle (°)	
O_2-O_{23}	2.81	C_5··C_4··O_2	120.7	C_5··O_3··O_1··O_4	175.7
O_2-O_{15}	2.37	C_4··O_2··O_{15}	114.0		
O_{15} –O_{23}	4.15	O_2··O_{15} ··O_3	108.1		
O_3 – C_4	4.18	O_{23}··O_2··O_{15}	106.6		
		O_{15}··O_3··C_{16}	110.6		
		C_4··O_2··O_{23}	119.8		

Figure 2.3 B3LYP/6-311++G(2d,2p) optimized structures of the *cisoid* (top) and *transoid* (bottom) transition states of the reaction of phenol with methylperoxyl with formic acid serving as a H-bond donor to the phenol.

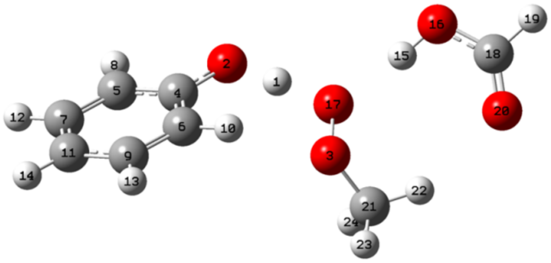

Bond (Å)		Angle (°)		Dihedral angle (°)	
O_2-O_{17}	2.38	$C_5 \cdot\cdot C_4 \cdot\cdot O_2$	118.5	$C_4 \cdot\cdot O_2 \cdot\cdot O_{17} \cdot\cdot O_3$	-6.2
O_2-O_{16}	2.76	$C_4 \cdot\cdot O_2 \cdot\cdot O_{17}$	119.7		
$O_{16}-O_{17}$	4.48	$O_2 \cdot\cdot O_{17} \cdot O_3$	108.4		
O_3-C_4	3.47	$O_2 \cdot\cdot O_{17} \cdot\cdot O_{16}$	121.4		
		$O_3 \cdot\cdot O_{17} \cdot\cdot O_{16}$	114.2		
		$C_{21} \cdot\cdot O_3 \cdot\cdot O_{17}$	108.7		

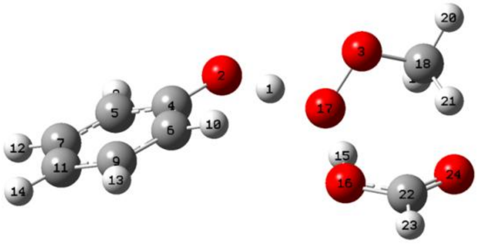

Bond (Å)		Angle (°)		Dihedral angle (°)	
O_2-O_{17}	2.39	$C_5 \cdot\cdot C_4 \cdot\cdot O_2$	118.8	$C_4 \cdot\cdot O_2 \cdot\cdot O_{17} \cdot\cdot O_3$	-144.8
O_2-O_{16}	4.55	$C_4 \cdot\cdot O_2 \cdot\cdot O_{17}$	116.0		
$O_{16}-O_{17}$	2.73	$O_2 \cdot\cdot O_{17} \cdot O_3$	104.3		
O_3-C_4	4.09	$O_2 \cdot\cdot O_{17} \cdot\cdot O_{16}$	125.4		
		$O_3 \cdot\cdot O_{17} \cdot\cdot O_{16}$	112.2		
		$C_{18} \cdot\cdot O_3 \cdot\cdot O_{17}$	108.8		

Figure 2.4 B3LYP/6-311++G(2d,2p) optimized structures of the *cisoid* (top) and *transoid* (bottom) transition states of the reaction of phenol with methylperoxyl with formic acid serving as a H-bond donor to the terminal oxygen atom of the methylperoxyl radical.

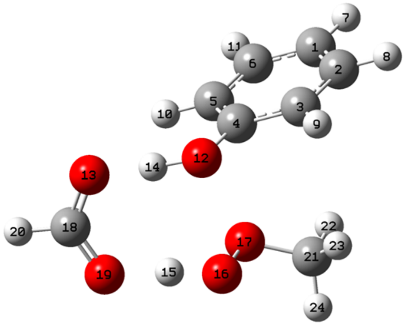

Bond (Å)		Angle (°)		Dihedral angle (°)	
O_{12}-O_{13}	2.46	$C_5{\cdot\cdot}C_4{\cdot\cdot}O_{12}$	122.8	$C_4{\cdot\cdot}O_{12}{\cdot\cdot}O_{16}{\cdot\cdot}O_{17}$	-15.8
O_{16}-O_{19}	2.45	$C_4{\cdot\cdot}O_{12}{\cdot\cdot}O_{13}$	115.2	$O_{12}{\cdot\cdot}O_{13}{\cdot\cdot}O_{19}{\cdot\cdot}O_{16}$	-5.9
O_{12} –O_{16}	2.76	$O_{12}{\cdot\cdot}C_{18}\cdot O_{19}$	96.3		
O_{17}– C_4	2.93	$O_{19}{\cdot\cdot}O_{16}{\cdot\cdot}O_{17}$	103.8		
		$O_{16}{\cdot\cdot}O_{17}{\cdot\cdot}O_{21}$	107.7		

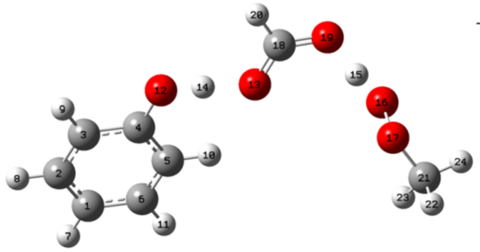

Bond (Å)		Angle (°)		Dihedral angle (°)	
O_{12}-O_{13}	2.44	$C_5{\cdot\cdot}C_4{\cdot\cdot}O_{12}$	122.5	$C_4{\cdot\cdot}O_{12}{\cdot\cdot}O_{16}{\cdot\cdot}O_{17}$	-88.1
O_{16}-O_{19}	2.45	$C_4{\cdot\cdot}O_{12}{\cdot\cdot}O_{13}$	112.7	$O_{12}{\cdot\cdot}O_{13}{\cdot\cdot}O_{19}{\cdot\cdot}O_{16}$	178.6
O_{12} –O_{16}	5.80	$O_{13}{\cdot\cdot}C_{18}\cdot O_{19}$	125.8		
O_{17}– C_4	6.52	$O_{19}{\cdot\cdot}O_{16}{\cdot\cdot}O_{17}$	103.5		
		$O_{16}{\cdot\cdot}O_{17}{\cdot\cdot}O_{21}$	107.8		

Figure 2.5 B3LYP/6-311++G(2d,2p) optimized structures of the *cisoid* (top) and *transoid* (bottom) transition states of the reaction of phenol with methylperoxyl with formic acid serving as both H-bond acceptor to the phenol and H-bond donor to the terminal oxygen of the peroxyl radical.

The incorporation of methanol into the model was also studied in the three configurations – with the methanol serving as a H-bond donor to phenolic oxygen atom, with methanol serving as a H-bond donor to the terminal oxygen atom of the peroxyl radical, and with methanol serving as both H-bond acceptor to the phenol and H-bond donor to the terminal oxygen of the peroxyl radical. The two (*cisoid* and *transoid*) transition state structures for each of these configurations are shown in Figures 2.6, 2.7 and 2.8, respectively, along with relevant bond lengths, angles and dihedral angles for ease of comparison.

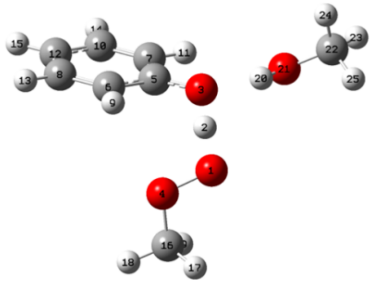

Bond (Å)		Angle (°)		Dihedral angle (°)	
O_3-O_{21}	2.92	C_3··C_5··C_6	121.5	C_5··O_3··O_1··O_4	-0.9
O_1-O_3	2.37	C_5··O_3··O_1	116.4	C_6··C_5··O_3··O_4	45.6
O_1-O_{11}	4.43	O_3··O_1··O_4	105.5		
O_4− C_5	3.32	O_1··O_4··C_{16}	108.6		
		O_3··O_{21}··C_{22}	115.8		
		O_{21}··C_3··C_1	113.4		

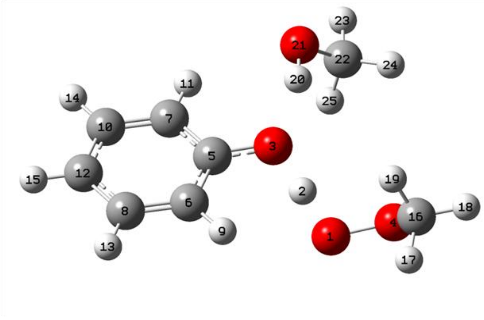

Bond (Å)		Angle (°)		Dihedral angle (°)	
O_3-O_{21}	2.94	C_3··C_5··C_6	121.1	C_5··O_3··O_1··O_4	-174.8
O_1-O_3	2.37	C_5··O_3··O_1	113.3	C_6··C_5··O_3··O_4	48.4
O_1 −O_{21}	4.43	O_3··$O_3$1··O_4	108.8		
O_4− C_5	4.18	O_1··O_4··C_{16}	110.3		
		O_3··O_{21}··C_{22}	115.5		
		O_{21}··C_3··C_1	112.6		

Figure 2.6 B3LYP/6-311++G(2d,2p) optimized structures of the *cisoid* (top) and *transoid* (bottom) transition states of the reaction of phenol with methylperoxyl with methanol serving as a H-bond donor to phenol.

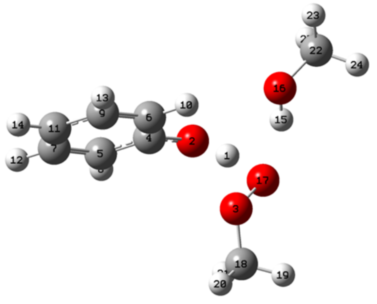

Bond (Å)		Angle (°)		Dihedral angle (°)	
O_2-O_{17}	2.38	$C_4{\cdot\cdot}O_2{\cdot\cdot}O_{17}$	111.6	$C_4{\cdot\cdot}O_2{\cdot\cdot}O_{17}{\cdot\cdot}O_3$	22.4
O_3-C_4	3.20	$C_2{\cdot\cdot}O_{17}{\cdot\cdot}O_3$	102.3	$C_6{\cdot\cdot}C_4{\cdot\cdot}O_2{\cdot\cdot}O_3$	57.9
O_{16}-O_{17}	2.91	$C_{17}{\cdot\cdot}O_3{\cdot\cdot}O_{18}$	108.6		
O_2 - O_{16}	3.90	$O_3{\cdot\cdot}O_{17}{\cdot}C_{16}$	94.1		
		$C_{17}{\cdot\cdot}C_{16}{\cdot\cdot}C_{22}$	115.1		
		$C_2{\cdot\cdot}C_{17}{\cdot\cdot}C_{16}$	94.5		

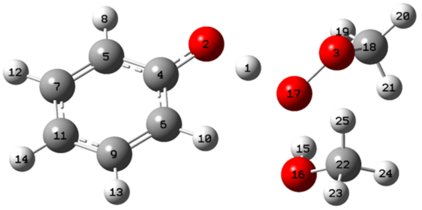

Bond (Å)		Angle (°)		Dihedral angle (°)	
O_2-O_{17}	2.38	$O_2{\cdot\cdot}C_4{..}C_6$	122.3	$C_4{\cdot\cdot}O_2{\cdot\cdot}O_{17}{\cdot\cdot}O_3$	-158.8
O_{16}-O_{17}	2.88	$C_4{\cdot\cdot}O_2{\cdot\cdot}O_{17}$	117.1	$C_6{\cdot\cdot}C_4{\cdot\cdot}O_2{\cdot\cdot}O_3$	22.5
O_2-O_{16}	4.14	$O_2{\cdot\cdot}O_{17}{\cdot\cdot}O_3$	104.1		
C_4- O_{16}	4.23	$O_2{\cdot\cdot}O_{17}{\cdot}O_{16}$	103.4		
		$O_3{\cdot\cdot}O_{17}{\cdot\cdot}O_{16}$	108.2		
		$O_{17}{\cdot\cdot}O_3{\cdot\cdot}C_{18}$	108.6		

Figure 2.7 B3LYP/6-311++G(2d,2p) optimized structures of the *cisoid* (top) and *transoid* (bottom) transition states of the reaction of phenol with methylperoxyl with methanol serving as a H-bond donor to the terminal oxygen atom of the methylperoxyl radical.

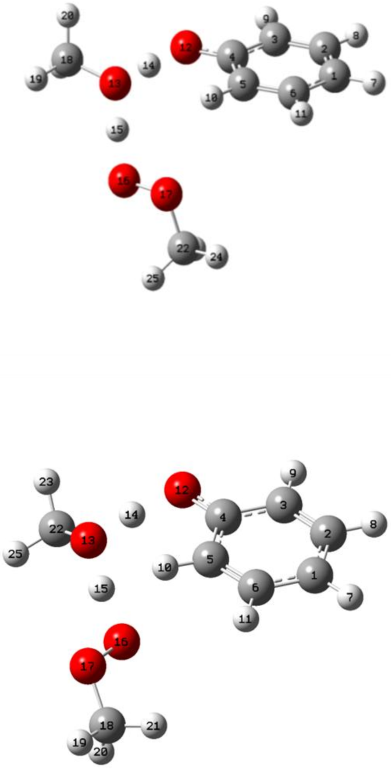

Bond (Å)		Angle (°)		Dihedral angle (°)	
O_{12}-O_{13}	2.41	$C_4\cdot\cdot O_{12}\cdot\cdot O_{13}$	118.7	$C_4\cdot\cdot O_{12}\cdot\cdot O_{16}\cdot\cdot O_{17}$	13.8
O_{13}-O_{16}	2.42	$C_{12}\cdot\cdot O_{13}\cdot\cdot O_{16}$	98.9		
O_{12}-O_{16}	3.67	$C_{13}\cdot\cdot O_{16}\cdot\cdot O_{17}$	100.1		
C_4 - O_{17}	3.89	$O_{16}\cdot\cdot O_{17}\cdot\cdot C_{22}$	108.2		
		$C_{12}\cdot\cdot C_4\cdot\cdot C_3$	119.6		

Bond (Å)		Angle (°)		Dihedral angle (°)	
O_{12}-O_{13}	2.41	$C_4\cdot\cdot O_{12}\cdot\cdot O_{13}$	114.5	$C_4\cdot\cdot O_{12}\cdot\cdot O_{16}\cdot\cdot O_{17}$	86.6
O_{13}-O_{16}	2.42	$C_{12}\cdot\cdot O_{13}\cdot\cdot O_{16}$	99.8		
O_{12}-O_{16}	3.69	$C_{13}\cdot\cdot O_{16}\cdot\cdot O_{17}$	105.7		
C_4 - O_{17}	4.58	$O_{16}\cdot\cdot O_{17}\cdot\cdot C_{18}$	119.5		
		$C_{12}\cdot\cdot C_4\cdot\cdot C_3$	108.0		

Figure 2.8 B3LYP/6-311++G(2d,2p) optimized structures of the *cisoid* (top) and *transoid* (bottom) transition states of the reaction of phenol with methylperoxyl with methanol serving as both H-bond acceptor to the phenol and H-bond donor to the terminal oxygen of the peroxyl radical.

The incorporation of water into the model was studied in three different configurations – with the water serving as a H-bond donor to phenolic oxygen atom, with water serving as a H-bond donor to the terminal oxygen atom of the peroxyl radical, and with water serving as both H-bond acceptor to the phenol and H-bond donor to the terminal oxygen of the peroxyl radical. The two (*cisoid* and *transoid*) transition state structures for each of these configurations are shown in Figures 2.9, 2.10 and 2.11, respectively, along with relevant bond lengths, angles and dihedrals for comparison.

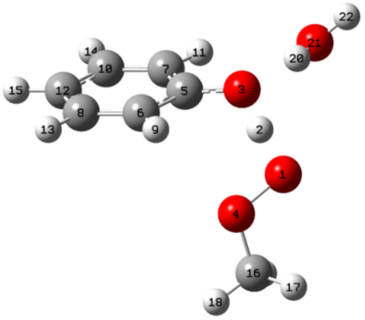

Bond (Å)		Angle (°)		Dihedral angle (°)	
O_3-O_{21}	2.91	$C_6{\cdot\cdot}C_5{\cdot\cdot}O_3$	121.3	$C_5{\cdot\cdot}O_3{\cdot\cdot}O_1{\cdot\cdot}O_4$	-4.2
O_1-O_3	2.37	$C_5{\cdot\cdot}O_3{\cdot\cdot}O_1$	117.8		
O_3-C_5	1.31	$O_3{\cdot\cdot}O_1{\cdot}O_4$	106.7		
O_4-C_5	3.38	$O_1{\cdot\cdot}O_3{\cdot\cdot}O_{21}$	114.4		
		$O_1{\cdot\cdot}O_4{\cdot\cdot}C_{16}$	108.5		
		$O_3{\cdot\cdot}O_{21}{\cdot\cdot}H_{22}$	113.9		

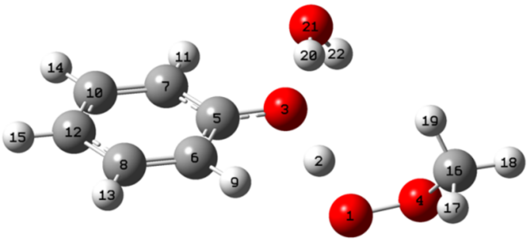

Bond (Å)		Angle (º)		Dihedral angle (º)	
O_3-O_{21}	2.92	$C_6{\cdot\cdot}C_5{\cdot\cdot}O_3$	121.1	$C_5{\cdot\cdot}O_3{\cdot\cdot}O_1{\cdot\cdot}O_4$	179.6
O_3-O_1	2.37	$C_5{\cdot\cdot}O_3{\cdot\cdot}O_1$	113.6		
O_3-C_5	1.31	$O_3{\cdot\cdot}O_1{\cdot}O_4$	108.8		
O_4-C_5	4.18	$O_1{\cdot\cdot}O_3{\cdot\cdot}O_{21}$	110.6		
		$O_1{\cdot\cdot}O_4{\cdot\cdot}C_{16}$	110.4		
		$O_3{\cdot\cdot}O_{21}{\cdot\cdot}H_{22}$	110.5		

Figure 2.9 B3LYP/6-311++G(2d,2p) optimized structures of the *cisoid* (top) and *transoid* (bottom) transition states of the reaction of phenol with methylperoxyl with water serving as a H-bond donor to phenol.

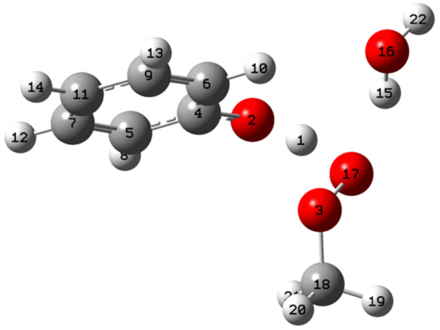

Bond (Å)		Angle (°)		Dihedral angle (°)	
O_2-O_{17}	2.38	C_2··C_4··C_6	122.5	C_4··O_2··O_{17}··O_3	23.05
O_{16}-O_{17}	2.91	C_4··O_2··O_{17}	111.5	C_6··C_5··O_2··O_3	58.3
O_2 –O_{16}	3.92	O_2··O_{17} ··O_3	102.2		
O_3 – C_4	3.20	O_{17}··O_3··C_{18}	108.6		
		O_{17}··O_{16}··H_{22}	112.9		
		O_2··C_{17}··C_{16}	95.4		

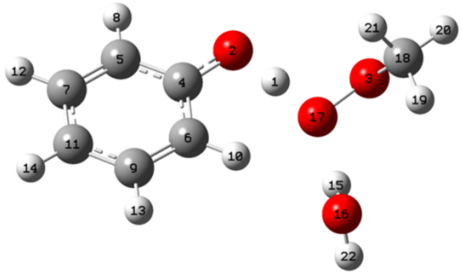

Bond (Å)		Angle (°)		Dihedral angle (°)	
O_2-O_{17}	2.38	O_2··C_4··C_6	122.1	C_4··O_2··O_{17}··O_3	-175.8
O_{16}-O_{17}	2.85	C_4··O_2··O_{17}	114.5	C_6··C_5··O_3··O_4	42.0
O_2 –O_{16}	4.22	O_2··O_{17} ··O_3	109.3		
O_3 – C_4	3.47	O_{17}··O_3··C_{18}	110.5		
		O_{17}··O_{16}··H_{22}	113.5		
		O_2··C_{17}··C_{16}	107.3		

Figure 2.10 B3LYP/6-311++G(2d,2p) optimized structures of the *cisoid* (top) and *transoid* (bottom) transition states of the reaction of phenol with methylperoxyl with water serving as a H-bond donor to the terminal oxygen of peroxyl radical.

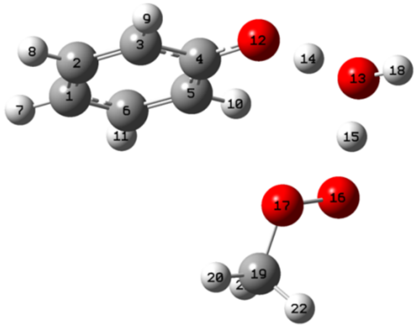

Bond (Å)		Angle (°)		Dihedral angle (°)	
O_{12}-O_{13}	2.40	C_3··C_4··O_{12}	119.0	C_4··O_{12}··O_{16}··O_{17}	-52.9
O_{13}-O_{16}	2.41	C_4··O_{12}··O_{13}	118.0		
O_{12} –O_{16}	3.81	O_{12}··O_{13} ··O_{16}	104.4		
O_4– C_{17}	3.32	O_{13}··O_{16}··O_{17}	98.0		
		O_{16}··O_{17}··C_{19}	108.3		
		H_{18}··O_{13}··O_{16}	112.7		

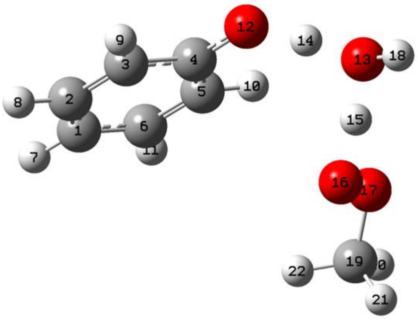

Bond (Å)		Angle (°)		Dihedral angle (°)	
O_{12}-O_{13}	2.40	C_3··C_4··O_{12}	119.3	C_4··O_{12}··O_{16}··O_{17}	85.0
O_{13}-O_{16}	2.41	C_4··O_{12}··O_{13}	113.6		
O_{12} –O_{16}	3.68	O_{12}··O_{13} ··O_{16}	99.9		
O_4– C_{17}	4.58	O_{13}··O_{16}··O_{17}	105.5		
		O_{16}··O_{17}··C_{19}	107.9		
		H_{18}··O_{13}··O_{16}	112.2		

Figure 2.11 B3LYP/6-311++G(2d,2p) optimized structures of the *cisoid* (top) and *transoid* (bottom) transition states of the reaction of phenol with methylperoxyl with water serving as both H-bond acceptor to the phenol and H-bond donor to the terminal oxygen of the peroxyl radical.

According to each of the calculated enthalpies of these structures, the H-atom abstraction from phenol via the *cisoid* TS is consistently preferred over the *transoid*

TS. The differences are 0.3 to 6.4 kcal/mol. The calculated enthalpies of activation for each process are given in Table 2.1 and the corresponding free energies of activation in Table 2.2.

Table 2.1 B3LYP/6311++G(2d,2f)-calculated absolute enthalpies (in Hartree) of the TS of reactions of phenol with methylperoxyl in the presence of formic acid, methanol and water in three different configurations compared to in their absence, except the enthalpy difference (Δ*H*) is in kcal/mol.

TS geometry		***Addivtive***			
		None	***Formic Acid***	***Methanol***	***Water***
	cis	-497.692048			
	trans	-497.691249			
	Δ*H*	*-0.5*			
H-bond to phenol	*cis*		-687.497687	-613.412060	-574.1344945
	trans		-687.487431	-613.407549	-574.1301584
	Δ*H*		*-0.6*	*-2.8*	*-2.7*
H-bond to peroxyl	*cis*		-687.497731	-613.411873	-574.1342674
	trans		-687.496745	-613.408708	-574.1311797
	Δ*H*		*-0.6*	*-2.0*	*-2.0*
H-bond to phenol and peroxyl	*cis*		-687.498559	-613.406864	-574.1279232
	trans		-687.490671	-613.406317	-574.1270715
	Δ*H*		*-5.0*	*-0.3*	*-0.5*

Table 2.2 B3LYP/6-311++G(2d,2p)-calculated absolute free energies (in Hartree) of the TS of reactions of phenol with methylperoxyl in the presence of formic acid, methanol and water in three different configurations compared to in their absence, except the free energy difference (Δ*G*) is in kcal/mol.

TS geometry		***Addivtive***			
		None	***Formic Acid***	***Methanol***	***Water***
H-bond to	*C*	-497.741743			
	T	-497.741344			
	ΔG	*-0.3*			
H-bond to Phenol	*C*		-687.560779	-613.476109	-574.1937255
	T		-687.552625	-613.4721285	-574.1901914
	ΔG		*-5.1*	*-2.5*	*-2.2*
H-bond to Peroxyl	*C*		-687.560899	-613.4742687	-574.1916634
	T		-687.559892	-613.4742768	-574.1896107
	ΔG		*-0.6*	*-0.005*	*-1.2*
H-bond to Phenol and peroxyl	*C*		-687.556612	-613.466794	-574.1831412
	T		-687.554397	-613.467039	-574.1825495
	ΔG		*-1.4*	*-0.2*	*-0.4*

2.4.2 Relevant Molecular Orbitals

In order to understand the preference for the *cisoid* transitions structures for the formal H-atom transfer reaction between phenol and methylperoxyl, we examined the frontier molecular orbitals for relevant differences as has been done previously for PCET reactions. The results are shown in Figures 2.12-2.21. In all cases, the HOMO of the *cisoid* transition structures show an interaction between the π HOMO of phenol and the π* SOMO of the methylperoxyl radical that is absent in the *transoid* transitions structures.

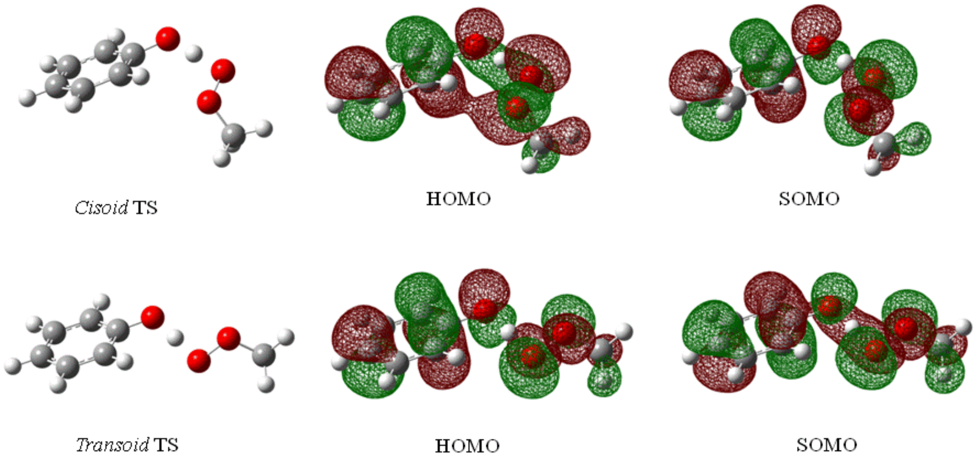

Figure 2.12 (Top) H-atom transfer from phenol to methylperoxyl in a *cisoid* conformation and (bottom) uncatalyzed H-atom transfer in a *transoid* conformation, along with their HOMO and SOMO.

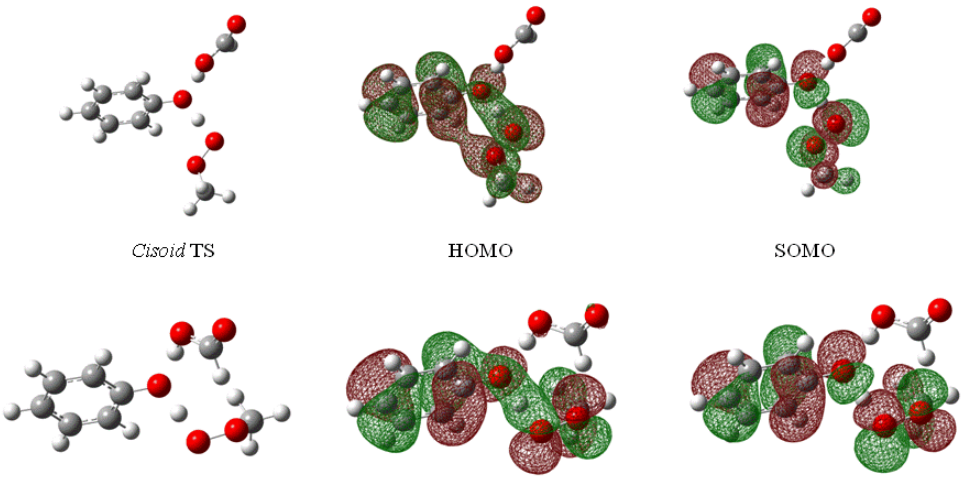

Cisoid TS HOMO SOMO

Transoid TS HOMO SOMO

Figure 2.13 (Top) H-atom transfer in a *cisoid* conformation and (bottom) H-atom transfer in a *transoid* conformation with formic acid as a H-bond donor to phenol, along with their HOMO and SOMO.

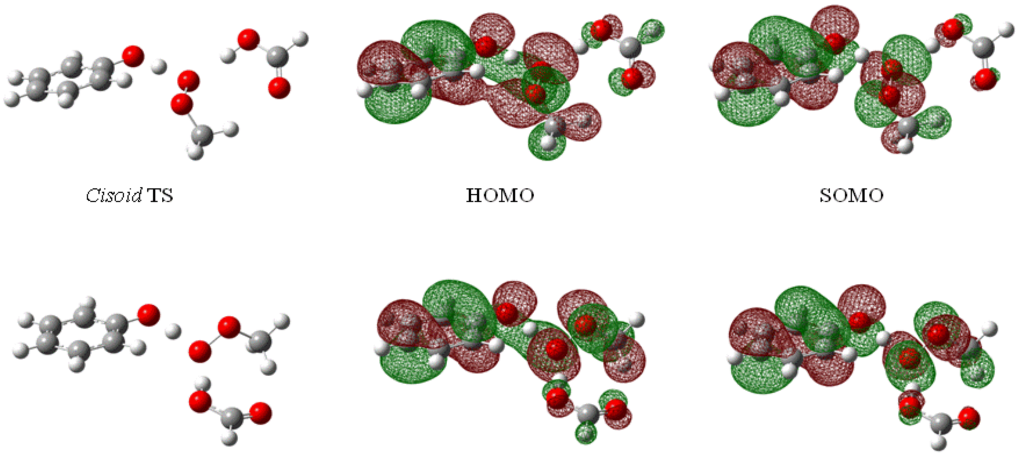

Cisoid TS HOMO SOMO

Transoid TS HOMO SOMO

Figure 2.14 (Top) H-atom transfer in a *cisoid* conformation and (bottom) H-atom transfer in a *transoid* conformation with formic acid as a H-bond donor to the terminal oxygen of peroxyl, along with their HOMO and SOMO.

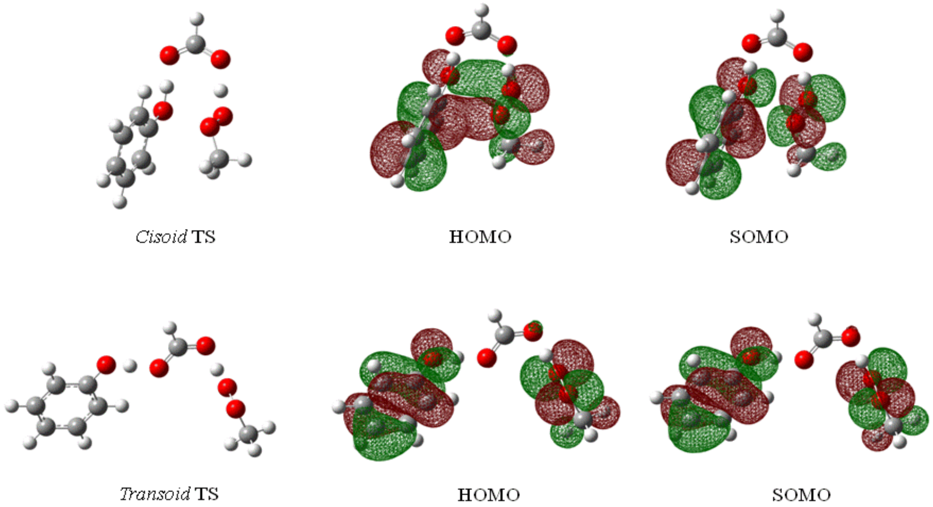

Figure 2.15 (Top) H-atom transfer in a *cisoid* conformation and (bottom) H-atom transfer in a *transoid* conformation with formic acid as a H-bond donor and acceptor to phenol and the terminal oxygen of peroxyl radical, along with their HOMO and SOMO.

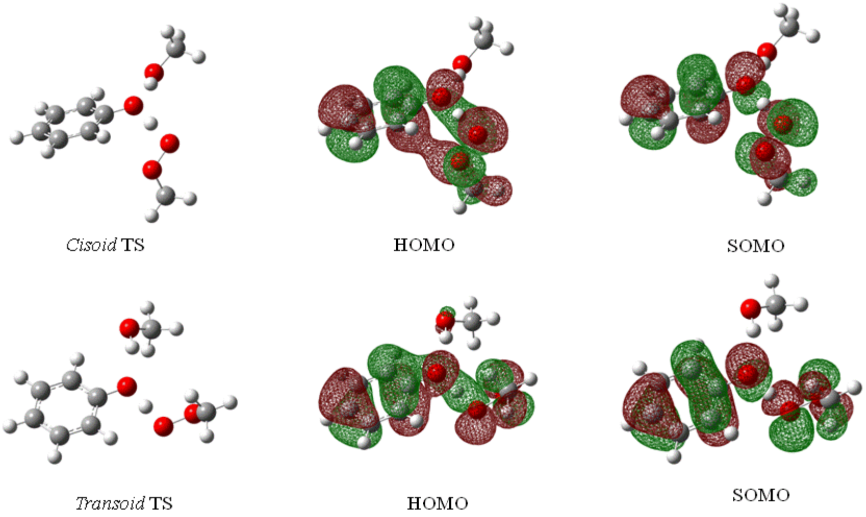

Figure 2.16 (Top) H-atom transfer in a *cisoid* conformation and (bottom) H-atom transfer in a *transoid* conformation with methanol as a H-bond donor to phenol, along with their HOMO and SOMO.

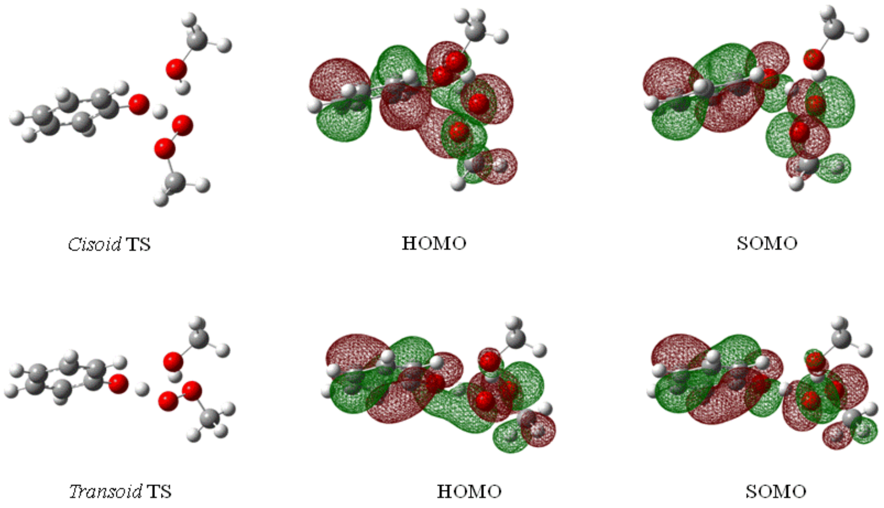

Figure 2.17 (Top) H-atom transfer in a *cisoid* conformation and (bottom) H-atom transfer in a *transoid* conformation with methanol as a H-bond donor to the terminal oxygen of peroxyl radical, along with their HOMO and SOMO.

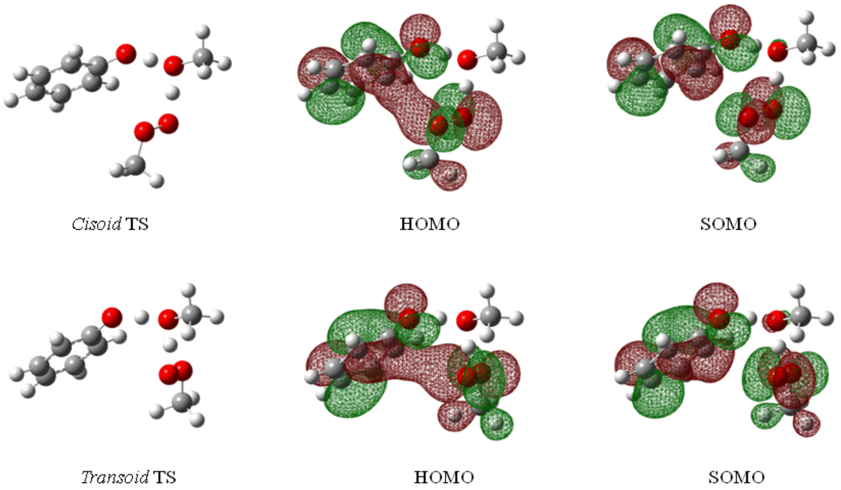

Figure 2.18 (Top) H-atom transfer in a *cisoid* conformation and (bottom) H-atom transfer in a *transoid* conformation with methanol as a H-bond donor and acceptor to phenol and the terminal oxygen of peroxyl radical, along with their HOMO and SOMO.

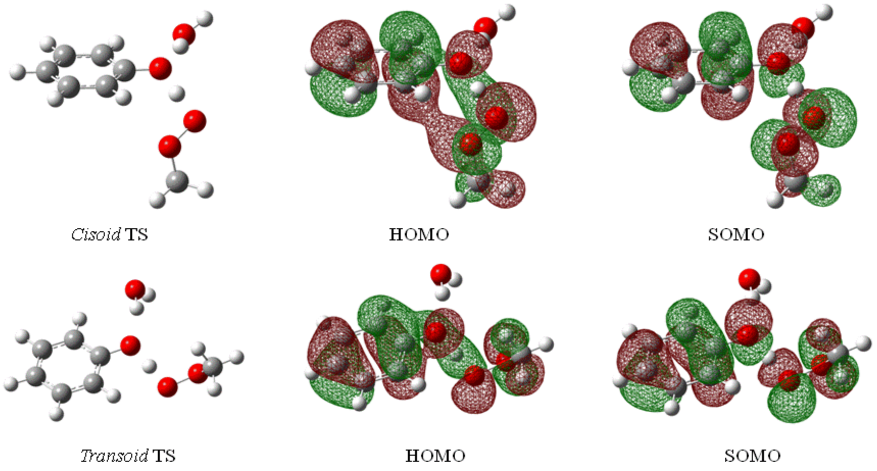

Figure 2.19 (Top) H-atom transfer in a *cisoid* conformation and (bottom) H-atom transfer in a *transoid* conformation with water as a H-bond donor to phenol, along with their HOMO and SOMO.

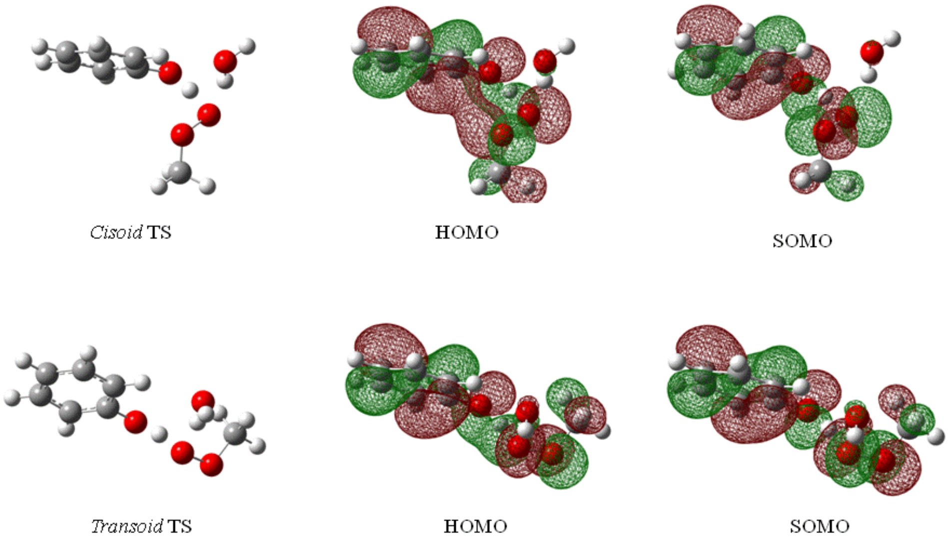

Figure 2.20 (Top) H-atom transfer in a *cisoid* conformation and (bottom) H-atom transfer in a *transoid* conformation with water as a H-bond donor to the terminal oxygen of peroxyl radical, along with their HOMO and SOMO.

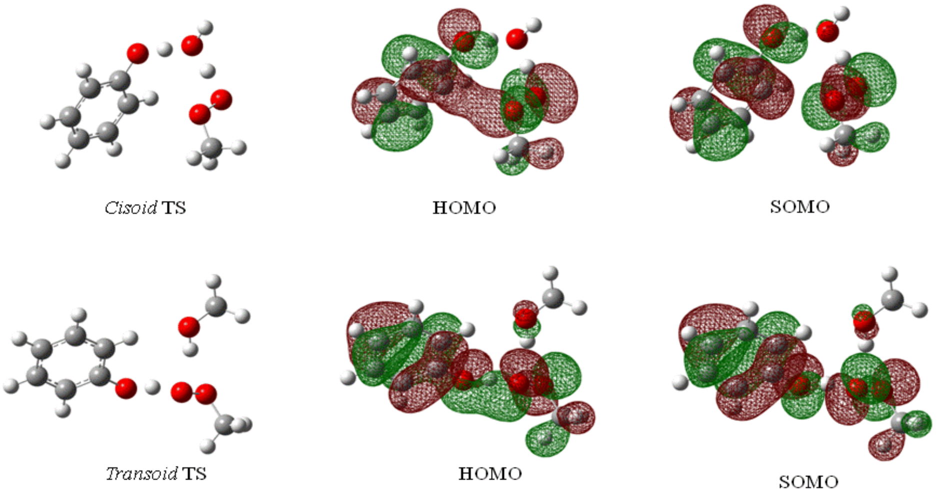

Figure 2.21 (Top) H-atom transfer in a *cisoid* conformation and (bottom) H-atom transfer in a *transoid* conformation with water as a H-bond donor and acceptor to phenol and the terminal oxygen of peroxyl radical, along with their HOMO and SOMO.

2.4.3 Reaction Enthalpy and Free Energy Profiles

Profiles of the enthalpies and free energies of the H-bonded pre-reaction complexes and the transition state structures are shown relative to those of the separated reactants for the reaction of phenol with methylperoxyl in Figure 2.22. Analogous profiles for the reactions involving formic acid, methanol and water are shown in Figures 2.23, 2.24 and 2.25, respectively.

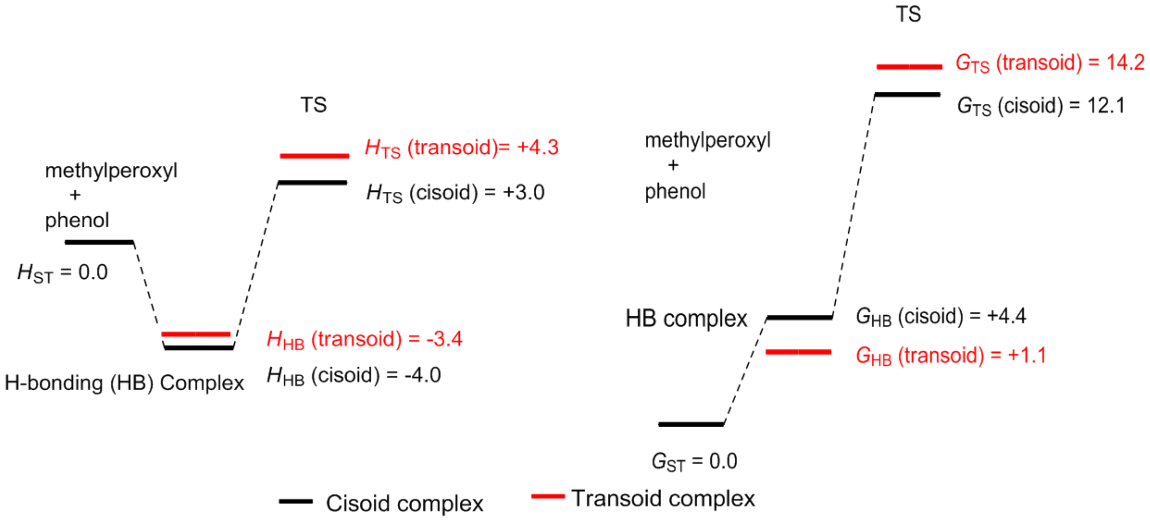

Figure 2.22 B3LYP/6-311++G(2d,2p)-calculated enthalpy (left) and free energy (right) profiles for the reaction of phenol with methylperoxyl via the *cisoid* pathways.

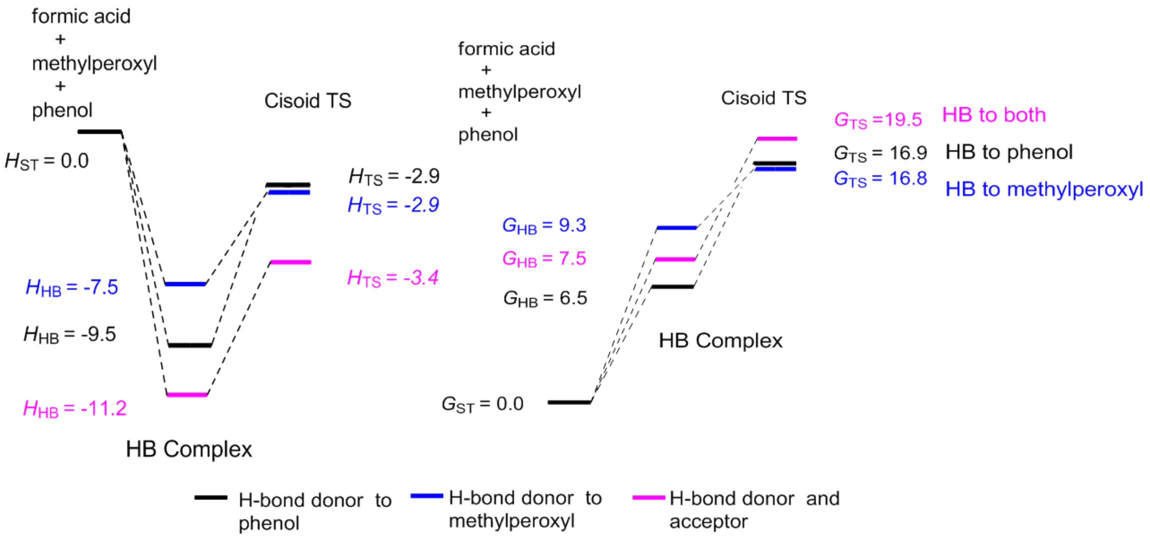

Figure 2.23 B3LYP/6-311++G(2d,2p)-calculated enthalpy (left) and free energy (right) profile for the reaction of phenol and methylperoxyl via *cisoid* pathways with the three different interactions with formic acid.

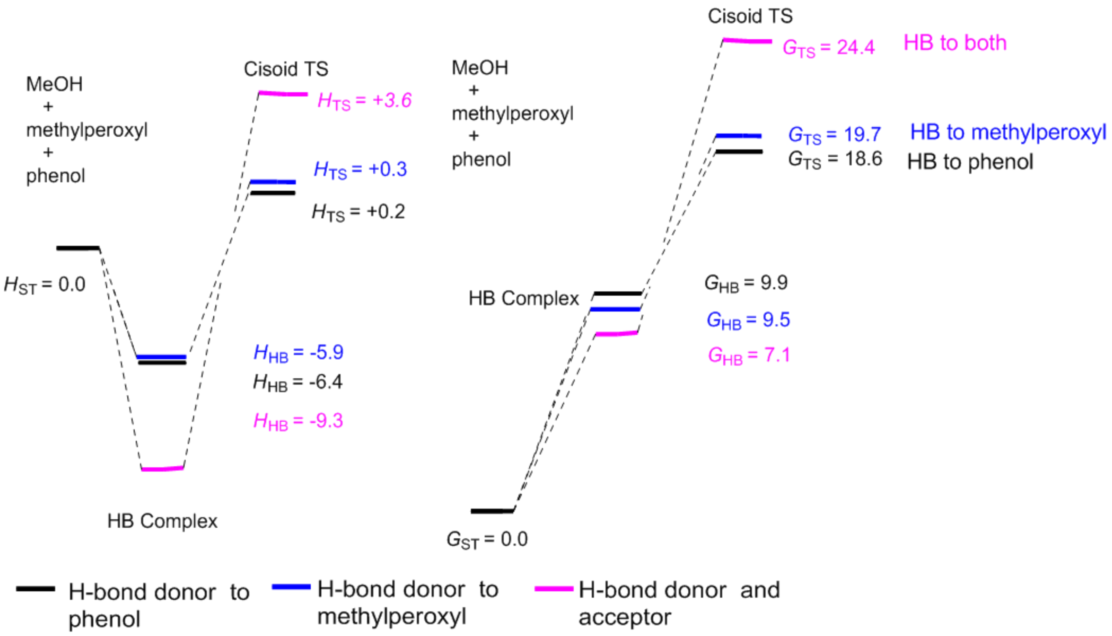

Figure 2.24 B3LYP/6-311++G(2d,2p)-calculated enthalpy (left) and free energy (right) profile for the reaction of phenol and methylperoxyl via *cisoid* pathway with the three different interactions with methanol.

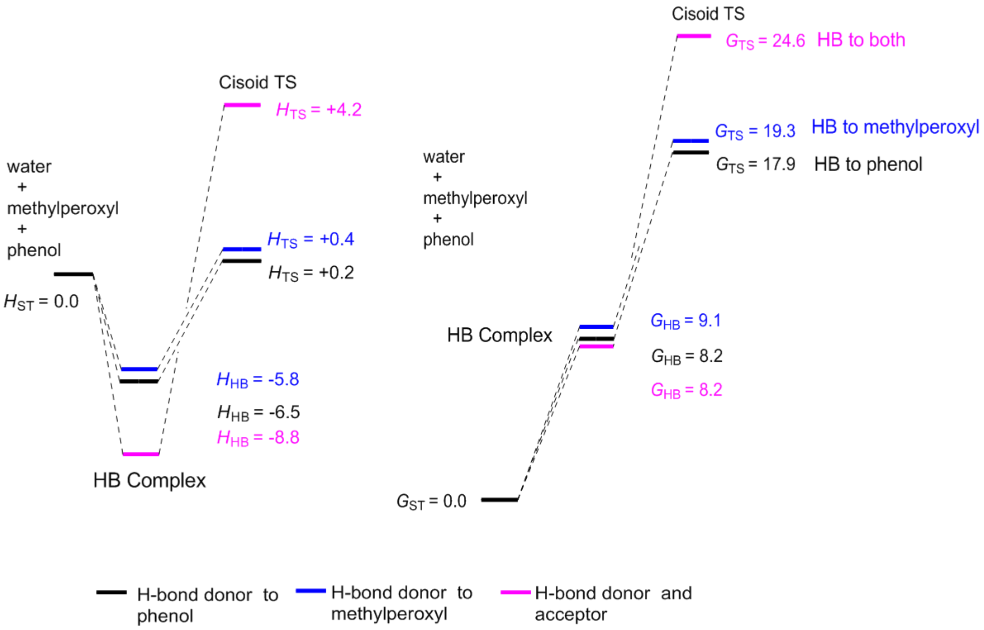

Figure 2.25 B3LYP/6-311++G(2d,2p)-calculated enthalpy (left) and free energy (right) profile for the reaction of phenol and methylperoxyl via *cisoid* pathway with the three different interactions with water.

2.4.4 Effect of Interactions with Solvent on Calculated Enthalpies and Free Energies of Activation

To aid in the discussion, the data above have also been collected in a single figure to demonstrate the relative effects of each additive on each of the reaction enthalpy and free energy profiles for the reaction of phenol with the methylperoxyl radical. The former is shown in Figure 2.26 and the latter in Figure 2.27.

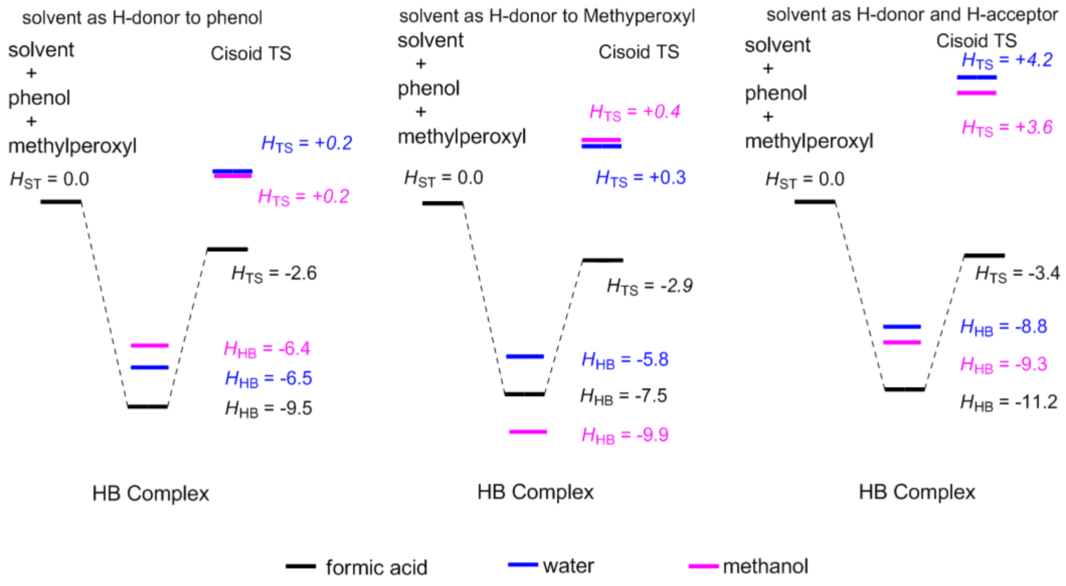

Figure 2.26 B3LYP/6-311++G(2d,2p)-calculated enthalpy profile via *cisoid* conformation of each solvent in the three modes of interaction.

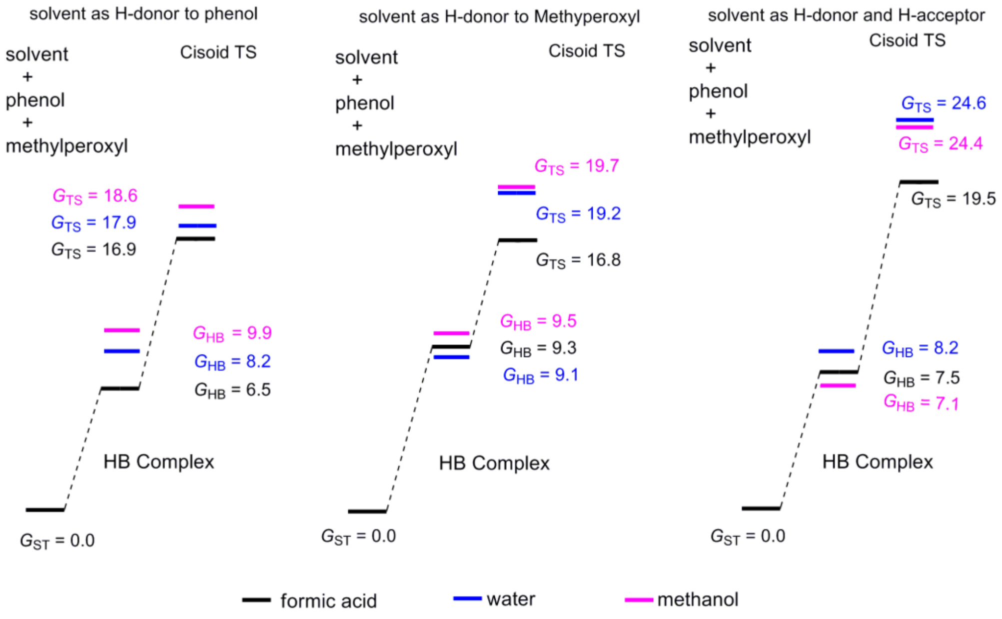

Figure 2.27 B3LYP/6-311++G(2d,2p)-calculated free energy profile via *cisoid* conformation of each solvent in the three modes of interaction.

2.5 Discussion

Although the rate of radical reactions are commonly assumed to be independent of the solvent, e.g. in H-atom abstraction from cyclohexane by cumyloxyl radicals,[84] Ingold and co-workers[85] have demonstrated dramatic solvent effects on the rates of H-atom abstraction from phenol and *tert*-butyl hydroperoxide by cumyloxyl radicals. They suggested that large solvent effects in these types of reactions could be rationalized on the basis of whether the H-atom that was being abstracted was sufficiently acidic to form a H-bond with the solvent. For those that were not, such as cyclohexane, no solvent effect would be observed. However, for those that were, such as phenol and *tert*-butyl hydroperoxide, the solvent effect would be proportional to the strength of the H-bond, and hence the equilibrium between H-bonded and non-H-bonded substrate. These ideas have been further developed as we pointed out in the Introduction, but the fundamental concept remains the same. Two exceptions have been noted, where the kinetics of these reactions have proved faster than expected: 1) in alcoholic solvents, and 2) in the presence of small amounts of acid. To better understand these exceptions, we performed computational studies on models of H-transfer from phenols to peroxyl radicals wherein formic acid, methanol and water were incorporated.

Previous theoretical calculations of the phenol/hydroperoxyl reaction couple by O'Malley, Popelier and co-workers[50] and the phenol/*tert*-butylperoxyl reaction couple by DiLabio and Johnson[77] which used similar B3LYP-based DFT approaches, have revealed that this reaction takes place via a *cisoid* TS structure that has the characteristics of a proton-coupled electron transfer (see Introduction). The validity of this important conclusion is supported by the excellent agreement between the calculated rate constant (k) of 1.4 x 10^4 $M^{-1}s^{-1}$ at 298 K, and calculated activation energy (E_a) of 5.6 kcal/mol with the experimental rate constant (k = 2.8 x 10^4 $M^{-1}s^{-1}$ at 303 K) and experimental activation energy (E_a = 5.2 kcal/mol),[86] noted by Johnson and DiLabio.[87] Therefore, in this current study, we used the same combination of B3LYP method and 6-311++G(2d,2p) basis set as did DiLabio and Johnson in their studies.

First, let us review the H-atom transfer from phenol to methylperoxyl without any additive. Methylperoxyl served as a more computationally tractable model for the secondary or tertiary peroxyls employed in the experimental investigations. In the absence of any solvent, two TS, as well as the two corresponding H-bonded pre-reaction complexes), were found. One is in the *cisoid* conformation and one is in the *transoid* conformation, as shown in Figure 2.2 (top) and Figure 2.2 (bottom). Enthalpy (ΔH_{TS}) of *cisoid* TS is 1.3 kcal/mol lower than that of the *transoid* TS (Figure 2.22). Usually, a *transoid* TS is preferred due to the steric bulkiness within the *cisoid* conformation. But in our case, the lower ΔH_{TS} of *cisoid* TS than *transoid* conformation is elucidated by HOMO and SOMO of each TS (Figure. 2.12). In *cisoid* TS, the overlapped interaction of (SOMO) π*-orbital of distal oxygen and (HOMO) π-orbital of phenol ring provides a shortcut for electron transferring while a proton transfers through σ-orbital overlapping between phenol oxygen and distal oxygen of methylperoxyl. In the *transoid* TS, both proton and electron transfer through the σ-orbital. Thus, *cisoid* TS conformation lowers the TS barrier by transferring electron and proton separately via separate pairs of orbitals.

It is indicating the π-π^* overlapping not only compensates the increase in enthalpy caused by steric bulkiness of a *cisoid* TS, but also over-compensates the enthalpy to favor the *cisoid* TS over the *transoid* TS. Because of the observed preference towards a *cisoid* TS over a *transoid* TS and an observed H-bonded pre-complex, it is indicating the H-atom transfer between phenol and methylperoxyl is a PCET process.

2.5.1 Reactions of Phenol and Methylperoxyl in the presence of Formic acid

The dramatic acid catalysis of the reaction of a variety of phenols with peroxyl radicals has been demonstrated for a variety of acids (i.e. acetic acid, HCl, *p*-toluenesulfonic acid, and trichloroacetic acid) in acetonitrile, but of these, acetic acid was found to be the most effective. In our calculations, formic acid was used in the place of acetic acid to save computational expense. It should be kept in mind that while acetic acid and formic acid are close in p*K*a values, 4.75 and 3.75, respectively, they differ considerably in polarity (the dielectric constants for acetic acid and formic acid are 6.2 and 58). As pointed out above, we envisioned three possible modes by which formic acid could serve to alter the energetic of the reaction: 1) as H-bond donor to the phenol, which would lower the phenolic O-H bond strength; 2) as H-bond donor to the methylperoxyl radical, which would increase the electrophilicity of the SOMO ; 3) as both H-bond acceptor to the phenolic O-H and H-bond donor to the methylperoxyl radical, thereby serving as a proton relay, while the electron can be transferred directly between the HOMO of the phenol and SOMO of the methylperoxyl radical. Indeed, we were able to locate low energy *cisoid* and *transoid* TS structures for each possibility, and in each case, the *cisoid* TS structures were lower in energy than the corresponding *transoid* ones.

As shown in Figure 2.23, ΔH_{HB} for formic acid serving as both H-bond donor and acceptor is the lowest due to the optimized H-bonding interactions: H-bond acceptor to the phenol and H-bond donor to the methylperoxyl. Comparing ΔH_{HB} for formic acid serving as a H-bond donor to methylperoxyl and to phenol, ΔH_{HB} for former is smaller due to the fact phenol is likely more basic than methylperoxyl radical so that formic acid forms a stronger H-bonding with phenol. However, in ΔG_{HB} profile, ΔG_{HB} for formic acid as both H-bond donor and acceptor is no longer the lowest due to the entropic cost of forming optimizing the H-bonded interactions and the resultant loss in degrees of freedom – an example of the concept of entropy-enthalpy compensation. Consideration of the three profiles reveals that there is a slight preference for the pathway wherein formic acid serves as H-bond donor to methylperoxyl, indicated by the lowest ΔG_{TS}. The association of formic acid with the methylperoxyl radical enhances its electrophilicity, facilitating the reaction.

Experimentally, Valgimigli et al.[83] have found something conceptually similar, but mechanistically distinct. Using kinetic isotope effect (KIE) studies, they were able to show that where primary KIEs prevail in the absence of acids ($k_{\mathrm{H}}/k_{\mathrm{D}}$ = 6.3±1.3 and 4.6±1.0 for reactions of pentamethylchromanol and 2-methoxy-4,6-dimethylpyrimidin-5-ol, respectively), in the presence of acetic acid, inverse KIEs are observed ($k_{\mathrm{H}}/k_{\mathrm{D}}$ = 0.9±0.3 and 0.6±0.2 for reactions pentamethylchromanol or 2-methoxy-4,6-

dimethylpyrimidin-5-ol, respectively). The observed inverse KIE in the presence of acetic acid indicates that H-atom transfer is not involved in the rate-determining step, but at the pre-equilibrium stage. Thus, the acid present in solution protonates the methylperoxyl radical, making it more electrophilic, such that it can now react by electron transfer with the phenol. The mechanism suggested by these results is shown in Scheme 2.9. Unfortunately, this is impossible to capture in our calculations.

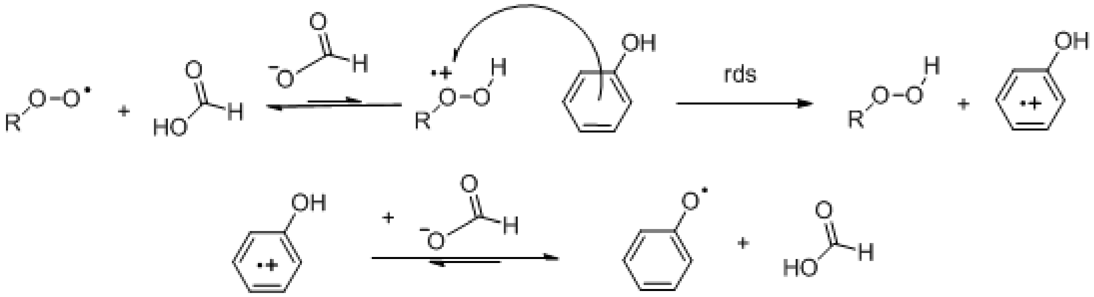

Scheme 2.9 Suggested mechanism for formic acid mediated H-atom transfer.

2.5.2 Reactions of Phenol and Methylperoxyl in the Presence of Methanol and Water

Given the foregoing, we wondered whether interactions between an alcohol and either the phenol, methylperoxyl, or both, may also lower the barrier to reaction. This would serve as an alternative explanation to SPLET for the rate enhancements observed in the reactions of phenols and peroxyl radicals. Again, three possible modes by which methanol could serve to alter the energetic of the reaction were envisioned: 1) as H-bond donor to the phenol; 2) as H-bond donor to the methylperoxyl radical; 3) as both H-bond acceptor to the phenolic O-H and H-bond donor to the methylperoxyl radical; and again we were able to locate low energy *cisoid* and *transoid* TS structures for each possibility. Also, in each case, the *cisoid* TS structures were lower in energy than the corresponding *transoid* ones.

Within the three modes of solvent interacting, ΔG_{TS} showed that the mode when methanol as a H-bond donor to phenol is favored, giving the lowest ΔG_{TS}=18.6 kcal/mol. As mentioned in section 2.3, Ingold and co-workers[75] proposed that methanol involved H-atom transfer was likely to go through a SPLET mechanism (Scheme 2.7). Ingold et al.[75] reported that methanol catalyzed the H-atom transfer by deprotonating the phenol. In their initial experiments, in order to avoid the interference of the water present in the methanol, it was distilled over Na directly prior to use. This made the MeOH inherently basic, exaggerating the effect. Nevertheless, in carefully dried and neutralized methanol, faster rates than what were expected were still observed. And with the addition of acid to surpress the necessary pre-equilibrium in SPLET, a decrease in the reaction rate was observed. We therefore performed calculations on models of phenols reacting with peroxyls that incorporated methanol as a model alcohol in order to understand effect, if any, it has on the energetics of the H-atom transfer process.

What we found from our calculations offers an alternative explanation to SPLET for the rate enhancement of this reaction in alcoholic solvents. Based on our calculations, H-bonding from methanol to the phenolic oxygen lowers the barrier to the H-atom transfer reaction, presumably by reducing the O-H bond strength of the phenol. This is essentially the intermolecular equivalent to the basis for the high reactivity of catechols, wherein intramolecular hydrogen bond donation to phenol lower the O-H BDE, shown in Scheme 2.10, since the phenoxyl radical is a better hydrogen-bond acceptor than the phenol itself,[88] thereby accelerating their rates of reaction.

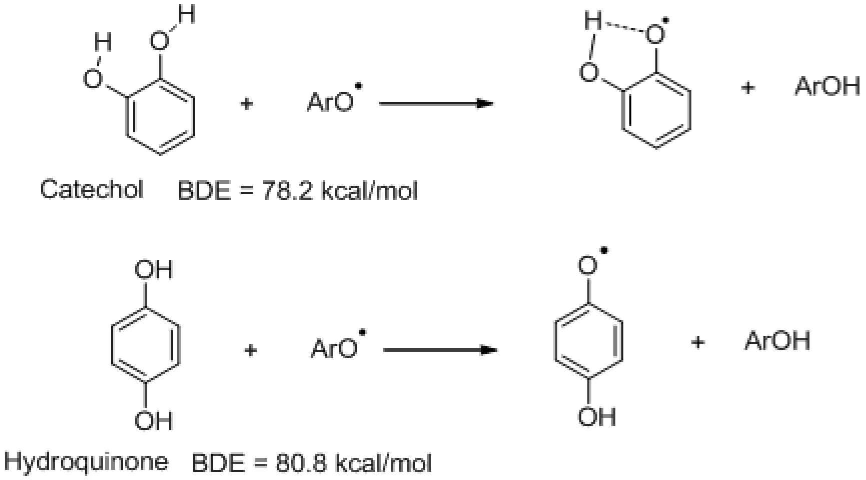

Scheme 2.10 BDEs for O-H bond for catechol and hydroquinone.

To round out our computational investigations of the involvement of acids and alcohols on the reactions of phenols with peroxyl radicals we considered water. Some water has been shown to be essential in achieving the impressive acid catalysis observed by Valgimigli et al.,[83] and is almost always present in the reactions carried out in alcoholic solvents. Again, the same three possible modes by which water could serve to alter the energetic of the reaction were envisioned, again we were able to locate low energy *cisoid* and *transoid* TS structures for each possibility, and again in each case, the *cisoid* TS structures were lower in energy than the corresponding *transoid* ones.

The results are almost indistinguishable from those obtained for the model incorporating methanol. The free energy profile again indicates that the favoured mode of incorporation of water in the model is when it serves as a H-bond donor to phenol. Since water will only be present in trace amounts in the alcoholic solvents, clearly this interaction is unlikely to be of importance in these cases.

2.6 Conclusions

From the calculations, we found that H-bonding interactions of formic acid, methanol and water with phenol and/or methylperoxyl are able to clearly influence the energetics of the formal H-atom transfer reaction between phenols and peroxyl radicals. Three modes of incorporation were studied for each additive, and each model revealed that the H-atom transfer between phenol and methylperoxyl is a PCET mechanism due to the intervention of a H-bonded pre-reaction complex and a low energy *cisoid* TS which clearly shows significant overlap between the π HOMO of the phenol and the π* SOMO of the peroxyl radical. Formic acid interacts most effectively as an H-bond donor to the methylperoxyl radical, which increases the electrophilicity of the π* SOMO of the peroxyl, leading to a lower enthalpy of activation. This is conceptually similar to what is observed by experiment in solution, where acetic acid has been shown to protonate the peroxyl in a rapid, but unfavourable pre-equilibrium step, followed by rate-determining electron transfer between the phenol and hydroperoxide radical cation. Methanol (and water) interacts most effectively as an H-bond donor to the phenol, which weakens the strength of the O-H in a manner similar to the intramolecular H-bond in catechols, and may serve as an alternative explanation to the SPLET mechanism advanced by Ingold and co-workers.

Chapter 3

A Kinetic Study of a Halogenase in the Pyrrolnitrin Biosynthetic Pathway

3.1 Introduction

3.1.1 Background and Significance

Pyrrolnitrin [3-chloro-4-(2'-nitro-3'-chlorophenyl)pyrrole] (PRN) is a secondary metabolite found in many pseudomonads and is known to have broad-spectrum antifungal activity.[89, 90] The primary mode of action of PRN occurs in the cell membrane, where it inhibits the syntheses of protein, RNA and DNA, largely through the electron transport chain, by uncoupling the normal flow of electrons.[91] Nowadays, due to pathogen resistance to fungicides and concern for public safety, natural substances obtaining antifungal activity are in high demand. Because of the antifungal activity of PRN, it was considered to have important mechanisms of biological control of fungal plant pathogens.[92-94] van Pée and coworkers[95] have pioneered the study of the biosynthesis of PRN in *Pseudomonas fluorescens* BL915, from which the *prn* genes were originally identified and cloned. L-tryptophan (L-Trp) was determined to be the precursor of PRN based on studies wherein bacterial cultures were fed with isotopically labeled and/or substituted Trp.[96-100] A biosynthetic pathway for PRN was proposed as early as 1976,[96-100] and refined by tracer studies and through the isolation of intermediates.[96, 98-101] The currently accepted biosynthetic pathway is shown in Scheme 3.1, and illustrates how each of the gene products, PrnA, PrnB, PrnC and PrnD, and a newly discovered PrnF,[102] contribute to the synthesis of PRN.

The function of the PRN-synthesizing genes in the *prn* operon has been suggested on the basis of product studies from the lysate of selected gene knockout strains of

Pseudomonas fluorescens BL915.[95] Shown in Scheme 3.1, PrnA, together with a hitherto unidentified flavin reductase, installs a chloride at the 7-position of L-Trp to give 7-chlorotryptophan (7-Cl-Trp); PrnB catalyzes the rearrangement of 7-Cl-Trp to a phenylpyrrole with concomitant decarboxylation to give monodechloroaminopyrrolnitrin (MDA); PrnC, which also requires a flavin reductase, installs a second chloride, but this time at the beta-position of the pyrrole ring to give aminopyrrolnitrin (APRN); PrnD, the last enzyme in the pathway, and also dependent on a flavin reductase, carries out a 6-electron oxidation of the amine group to a nitro group. Recent studies have lead to the identification of a flavin reductase within the *prn* operon from *Pseudomonas fluorescens* BL915. This flavin reductase has been subsequently cloned and overexpressed in *E.coli* and was shown to work more effectively with PrnD (k_{cat} = 11.3 min^{-1}) than other flavin reductases (e.g. SsuE, k_{cat} = 6.8 min^{-1}, a flavin reductase from *E.coli*). To date, PrnF has not been assayed for its ability to reduce the flavin as part of PrnA and PrnC catalysis. Looking at the biosynthetic pathway to pyrrolnitrin in chemistry perspective, it is noted that two of the four enzymes, PrnA and PrnC, ensure regioselectivities of the installed Cl.[103]

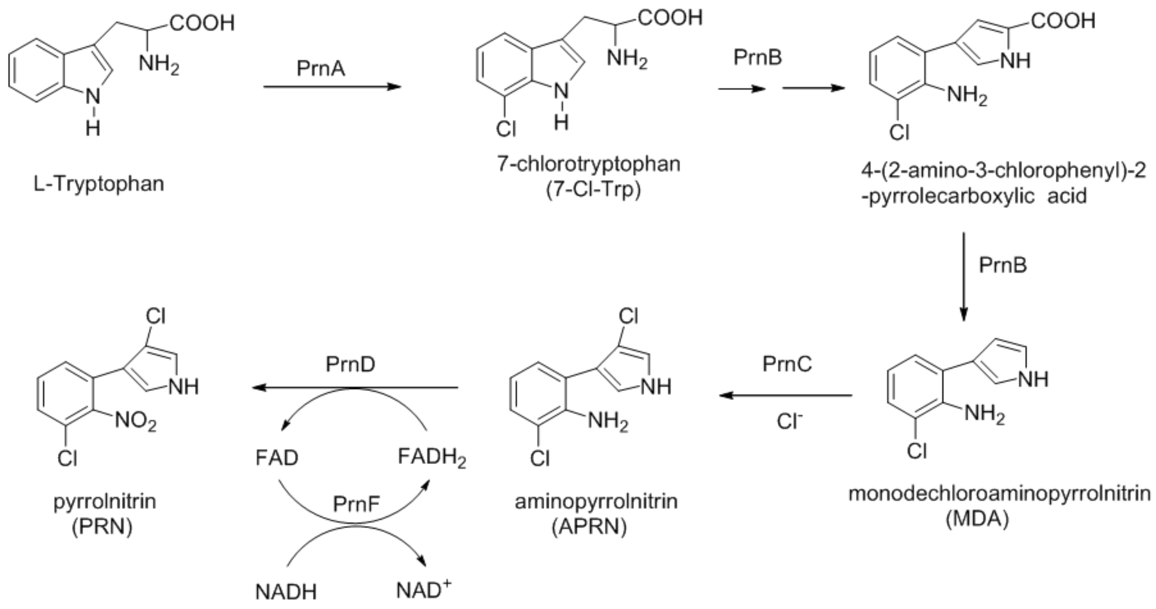

Scheme 3.1 The proposed biosynthetic pathway to pyrrolnitrin.

Halogenated molecules are abundant in nature. Some of them are natural products and some are man-made compounds.[104] Up to now, the number of halogenated natural products that have been discovered is larger than 4500, and is comprised of a list that is surely incomplete.[105] Halogenated natural products are often secondary metabolites of microbial organisms. Within these organisms, there is often a cluster of genes present, expressing enzymes that incorporate the halogen atoms into these secondary metabolites. Halogen insertion into substrates alters the physical and chemical properties of the substrate by both steric effects and electronic effects. This way, it determines the selectivity and affinity of the substrate interacting with biological targets and helps the host organism adapt to the biological environment.

Halogenases function on a broad range of organic molecule motifs, including aliphatic carbons, olefinic centers, aromatic rings and heterocyclic rings. That gives a variety of natural products including 2300 organochlorines, 2100 organobromines, 120 organoiodines and 30 organofluorines (Scheme 3.2).[105] The fact that more than 95% of the organohalides are chlorine and bromine-containing natural products reflect the natural abundance of chloride and bromide ions in the biosphere. Organochlorines are usually found in terrestrial microorganisms whereas organobromines are usually found in marine microorganism due to the natural abundance of chloride in soil and bromide in marine environments.

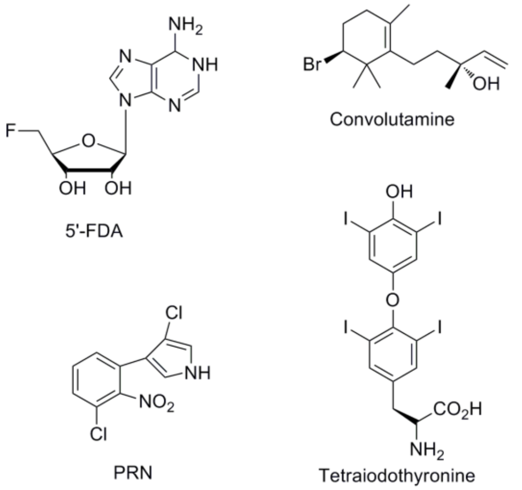

Scheme 3.2 Biologically active organohalides.

Many organochlorines are therapeutically interesting, such as vancomycin, rebeccamycin, chlortetracycline, and chloramphenicol[106-109] (Scheme 3.3). Vancomycin is used to treat Gram-positive bacterial infections when other antibiotics are not effective[106]; rebeccamycin was discovered as antibiotic against several Gram-positive bacterial strains, and is a promising antitumor agent due to its capability of targeting DNA topoisomerase I and II[109]; chlortetracycline is commonly used in veterinary medicine to treat conjunctivitis in cats; and chloramphenicol is the first antibiotic to be manufactured on a large scale and it is effective against wide range of microorganisms.[108] Some of the organochlorines are antibiotics with a broad spectrum of anti-fungal activity for plant protection and preservation, such as pyrrolnitrin and pyoluteorin. It is known that pyrrolnitrin (Scheme 3.3) is an important secondary metabolite produced in the strains of *Pseudomonas*, playing a role of biological control of fungal plant pathogens.[95] Pyoluteorin (Scheme 3.3), another chlorine-incorporated antibiotic, is known as an inhibitor to *oomycete Pythium ultimum*.[110]

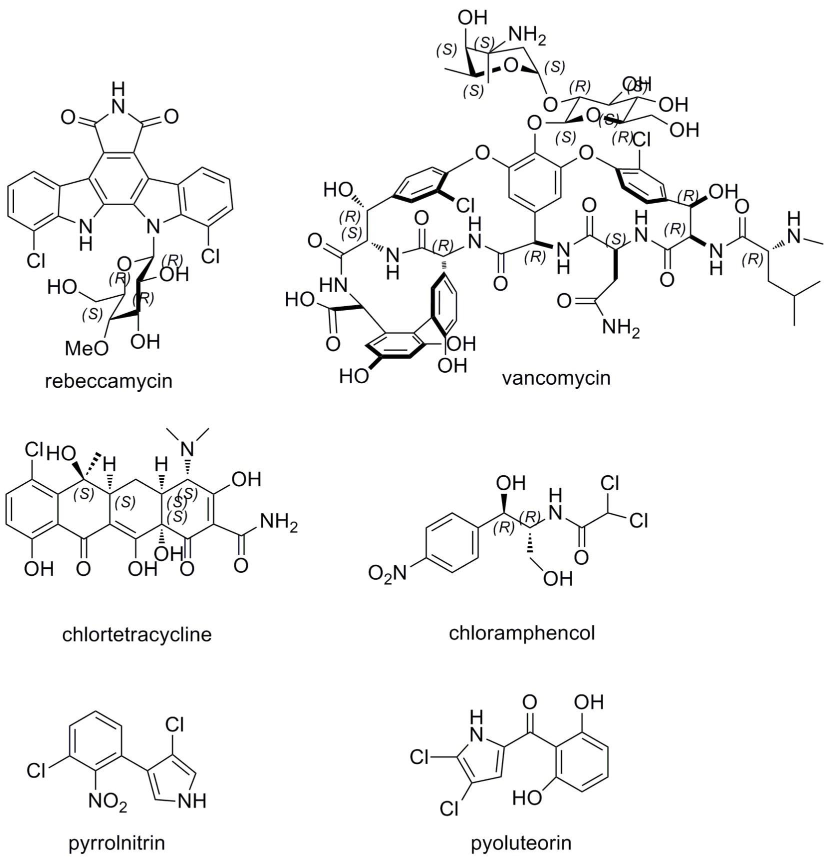

Scheme 3.3 Examples of natural organochlorines. Rebeccamycin, vancomycin, chlortetracycline, chloramphenicol are of therapeutic interest. Pyrrolnitrin and pyoluteorin are particularly useful against plant pathogens.

In nature, fluorinated natural products are not encountered as commonly as chlorinated, brominated or iodinated products, although fluoride is present in the earth crust in a fairly large amount. From a mechanistic perspective, F^- is highly electronegative and therefore much more difficult to oxidize to an electrophile or a radical species than Cl^-, Br^- and I^-. This and its toxicity to many organisms – may be the reason that fluorinated metabolites are rarely seen. However, nucleophilic halogenases[111] are known to be able to install F$^-$, as well as Cl$^-$, as nucleophiles to electrophlic substrates. Besides the good leaving group of a substrate facilitates the nucleophilic attach the halide anion, the halide binding site in the active site is surrounded by hydrophobic amino acid side chains, helping to desolvate the F$^-$ ion, and facilitate reaction. One example is the 5‘-fluoro-5’-deoxyadenosine synthase (5’-FDAS) from *Streptomyces cattleya*.[111, 112] This enzyme catalyzes fluorination of *S*-adenosyl-L-methionine (AdoMet) to give 5’-deoxy- 5’- fluoroadenosine (5’-FDA) and L-Met as a leaving group in S_N2 fashion (Scheme 3.4). A homologous of 5’-FADS was found in marine bacteria *Salinispora tropica* and chlorinates AdoMet to 5’-ClDA.[111, 112]

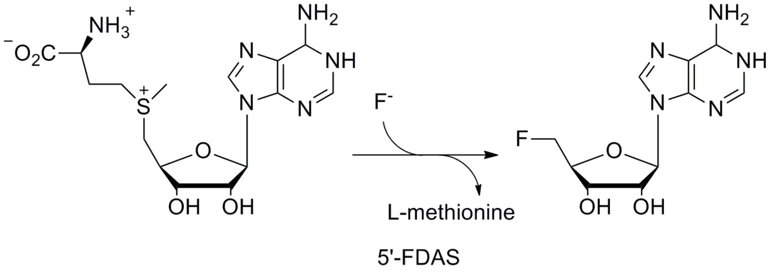

Scheme 3.4 Enzymatic fluoronation of *S*-adeno-syl-L-methionine (AdoMet).

In general, the strategies of chlorination, bromination and iodination in nature are similar. In the world of enzymatic halogenation, the abundant anions Cl$^-$ and Br$^-$ (and sometimes I$^-$) are usually oxidized and readily react as electrophiles or radical species. Here, we mainly focus on these major halogenases, whose common enzymatic strategy is predominantly oxidative. Among them, there are two main categories of halogenases: haloperoxidases and O_2-dependent halogenases, categorized according to the different oxidants employed.

3.1.2 Haloperoxidases

Haloperoxidases use hydrogen peroxide (H_2O_2) as an oxidant to activate the halide ion for electrophilic reactions. Haloperoxidases are divided into three sub-categories according to the type of redox cofactor that is employed: heme-dependent haloperoxidases use a heme group as a redox cofactor; vanadium-dependent haloperoxidases use a vanadium complex as a redox cofactor; and non-heme iron haloperoxidase use a non-heme iron complexed to amino acid side chains as a redox cofactor.

3.1.2.1 Heme-Dependent Haloperoxidases

Haloperoxidases use a heme-iron complex as redox cofactor, which oxidizes halide anions to give a bound (-OX), an “X^+” equivalent. (-OX) is then released as hypohalous acid.[113] X in this case can be chloride, bromide or iodide, but not fluoride.[113] The general mechanism of a heme-dependent halogenase is shown in Scheme 3.5. H_2O_2 is used to oxidizes the heme iron. The generated protoporphyrin cation radical is a particularly strong oxidant,[113, 114] which effectively oxidizes X^- to give a bound hypohalite anion (-OX), a “X^+” equivalent. It was suggested by Sundaramoorthy et al. that –OX is released as HOX, which can then act as an electrophilic halogenating agent on the substrate.[113]

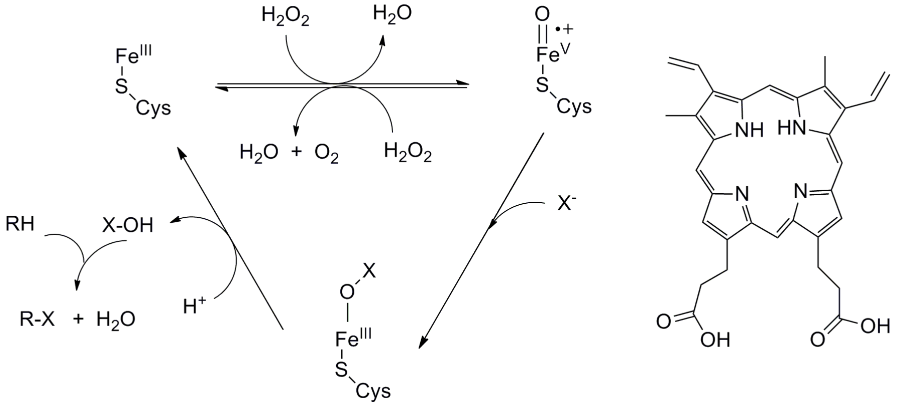

Scheme 3.5 General mechanism of heme-dependent haloperoxidases (protoporphyrin ring is shown on the right).

The first example was a fungal enzyme isolated from *Caldariomyces fumago*, chloroperoxidase (CPO). It is shown in Scheme 3.6 that CPO installs Cl on a dione substrate to produce gem-di-chloro metabolite caldariomycin.[114-116]

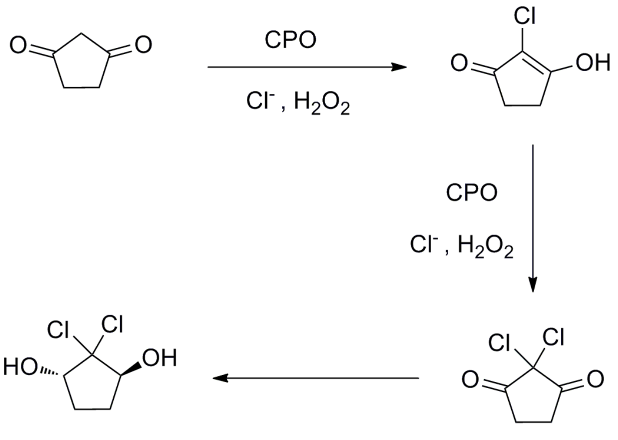

Scheme 3.6 heme-dependent haloperoxidase CPO chlorination on a dione.

3.1.2.2 Vanadium-Dependent Haloperoxidases

Vanadium-dependent haloperoxidases function in a similar way to the heme-dependent ones. However, as the name tells us, instead of using a heme-iron complex as a redox cofactor, it makes use of a vanadium complex to activate the halide ion. In doing so, as shown in Scheme 3.7, a vanadium (-OX) species is generated, which is hydrolyzed to give hypohalous acid to react with substrates. However, the oxidative state of the metal centre does not formally change over the process of generating a (-OX) species.[104] According to the X-ray structure of the vanadium complex, the imidazole ring of a bound histidine is the only anchor of this vanadium complex to the active site of the haloperoxidase.[117] The typical enzymes from this class are vanadium-dependent chloroperoxidases (V-CPOs) from certain fungi and vanadium-dependent bromoperoxidases (V-BrPOs) from marine algae.[118] One example of V-BrPO bromination is shown in Scheme 3.8.

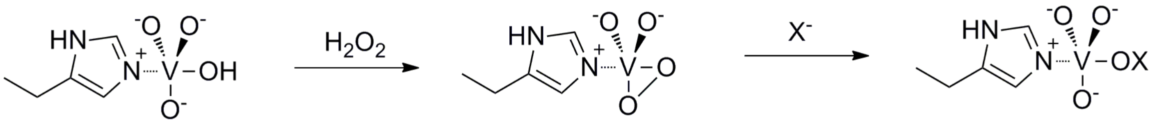

Scheme 3.7 General mechanism of vanadium-dependent haloperoxidases.[104]

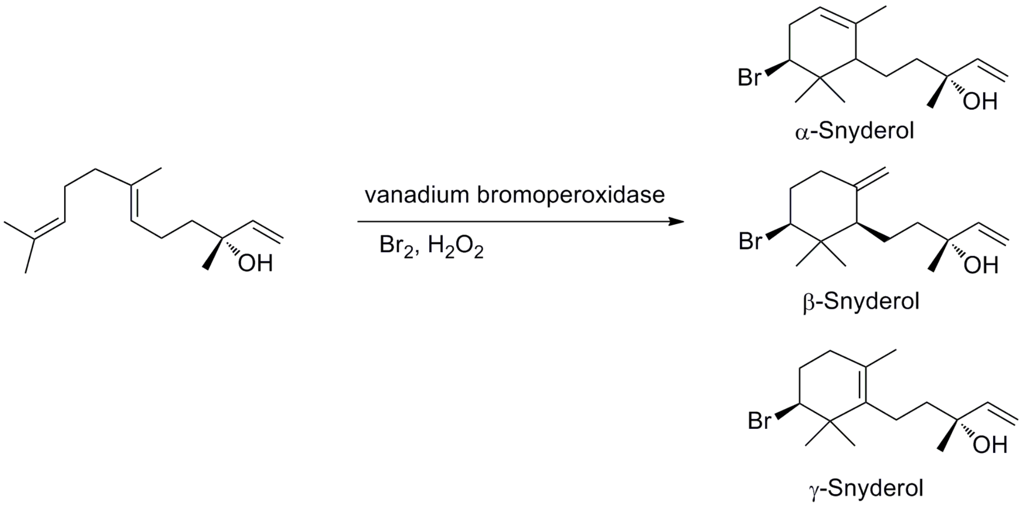

Scheme 3.8 Formation of α–, β–, γ-snyerol by vanadium-dependent bromoperoxidase.

3.1.2.3 Non-Heme Haloperoxidases

The last class of haloperoxidase contains a non-heme iron as redox cofactor. This was first discovered in the bacterium *Pseudomonas pyrrocinia* in 1986.[119] Since then, examples have been isolated from other microorganisms, including algae and other *Pseudomonas* species.[120-122] The mechanism for these non-heme iron haloperoxidases is very similar to the heme-iron haloperoxidases, except that instead of heme, the redox active iron atom is ligated by amino acid side chains. The enzyme non-heme iron bromoperoxidase from *Corallina pilulifera* was investigated. It catalyzed bromonation on monochlorodimedone to monobromomonochlorodimedone, shown in Scheme 3.9 (A).[123] Its mechanism was described by Itoh, et al in 1986, and is shown in Scheme 3.9 (B).[123]

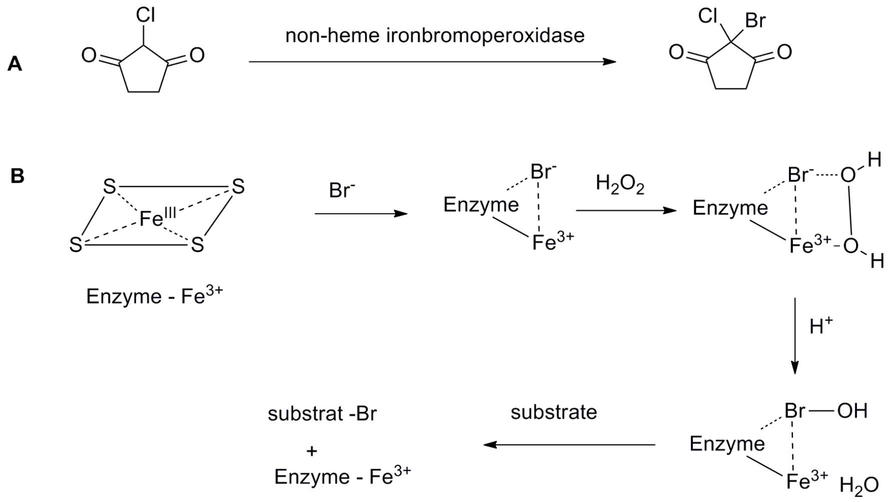

Scheme 3.9 A. non-heme iron bromoperoxidase bromonation on monochlorodimedone. B. General mechanism of non-heme iron haloperoxidation at the active site.

3.1.3 Oxygen-Dependent Halogenases

It was not known until 1997 that O_2-dependent halogenases are responsible for the majority of halogenations in microorganisms.[117] An enzyme Cts4 responsible for assembling C_7-Cl bond of the tetracycline nucleus in chlortetracycline biosynthetic pathway was first discovered to be a flavoprotein.[124] Since then, homologues of this halogenase were subsequently found in electron rich aromatic motif of natural product.[107, 109, 125] Although haloperoxidases were first isolated, characterized and studied, they are not often involved in synthesizing more complicated metabolites. On the other hand, the two types of O_2-dependent halogenases are taking an important role in the world of halogenation.[104] O_2 is the oxidant adapted by O_2-dependent halogenases. The two types of O_2-dependent halogenases are non-heme iron halogenases, using a non-heme iron complex as redox cofactor and α-ketoglutarate (α-KG) as a co-substrate, and

$FADH_2$-dependent halogenases, using $FADH_2$ as a redox cofactor (Scheme 3.10). They are responsible for inserting mostly chloride and bromide ions at certain positions of the substrate molecules.[126]

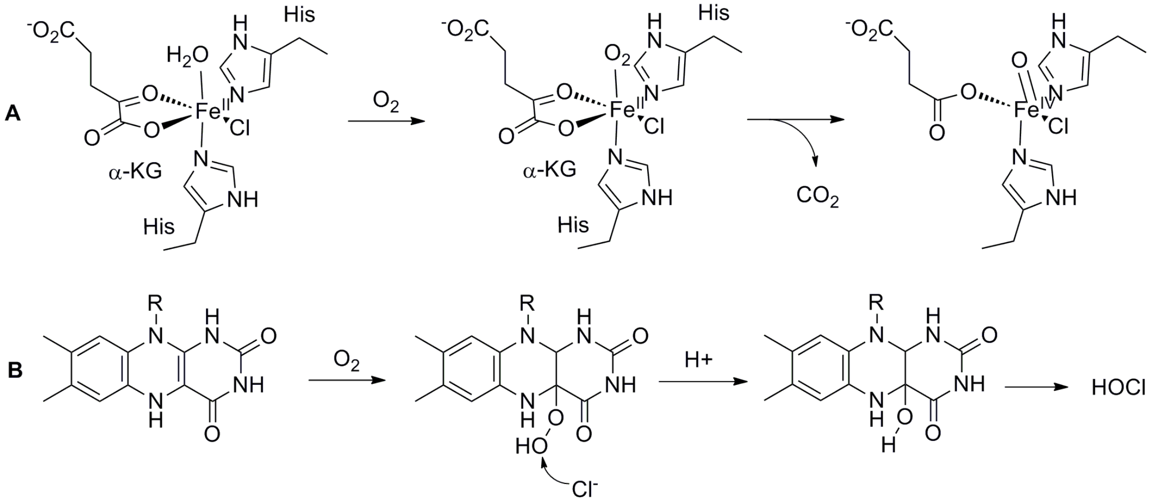

Scheme 3.10 Reactive intermediates generated by non-heme Fe^{2+}- and $FADH_2$- dependent halogenases. (A) Intermediates in the mechanism of non-heme Fe^{2+}- dependent halogenases. (B) Intermediates in the mechanism of $FADH_2$-dependent halogenases.[104]

The two oxidants of O_2-dependent halogenases and haloperoxidases, molecular oxygen and hydrogen peroxide, have the same formal oxidation states and function in the same logic. The two redox cofactors, $FADH_2$ and α-KG bound to a non-heme iron complex, are first oxidized by di-oxygen to form two powerful oxidizing reagents. Their redox power correlates to the oxidative potentials of the carbon sites to be halogenated.[104] While Cl^- is oxidized to "Cl^+" equivalent or a radical species, the oxidized cofactors are reduced to where they start from and can be oxidized to catalyze another reaction.

3.1.3.1 α-Ketoglutarate-Dependent Halogenases

It was observed that some halogenated natural products contain the halogen at an unactivated aliphatic carbon (e.g., barbamide), rather than an electron-rich aromatic rings.[127] From sequencing data of some O_2-dependent halogenases, their amino acid sequences did not show homology to the sequences of flavin-dependent.[127] These two observations suggested another class of O_2-dependent enzyme exists in nature. This class came to be known as α-ketoglutarate-dependent halogenases. The reason that α-ketoglutarate-dependent halogenases are able to halogenate the unactivated aliphatic carbons is that a high-valent oxoiron species[27] is generated as a powerful oxidant to abstract the H• from an un-activated carbon of the substrate. The mechanism shown in Scheme 3.11 was proposed based on studies of microbial non-heme iron hydroxylases, which operated by a very similar mechanism (*vide infra*).[128]

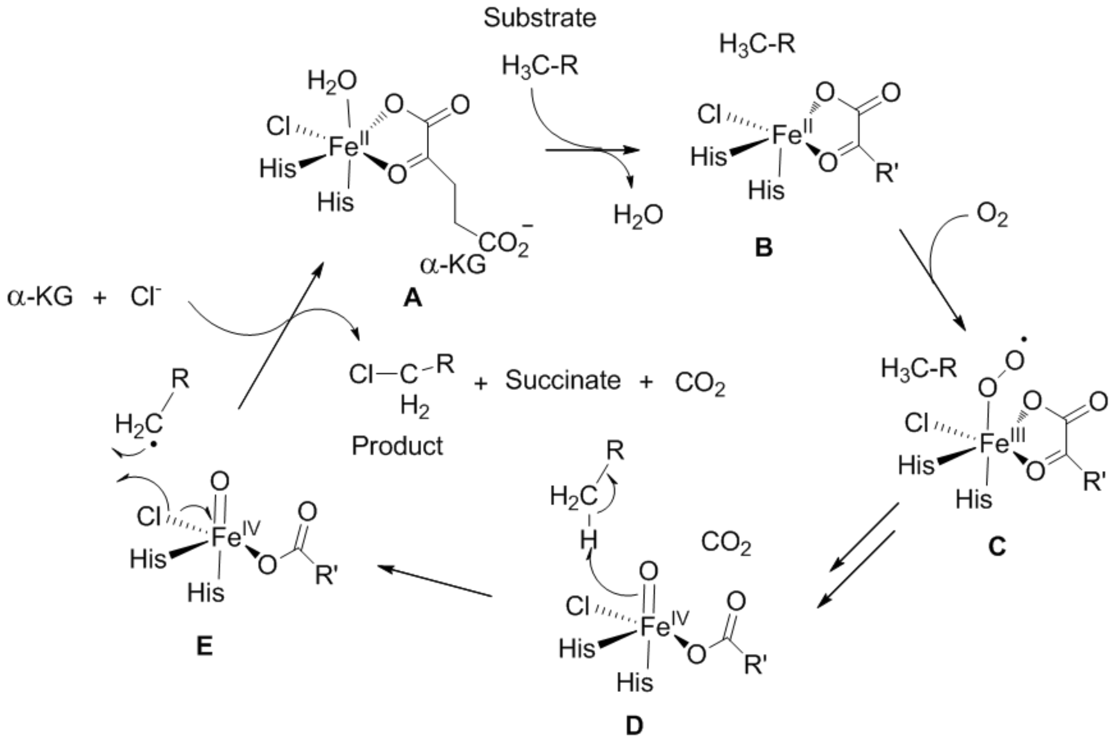

Scheme 3.11 Accepted mechanism of α-Ketoglutarate-Dependent Halogenases.

Non-heme iron halogenases contain an iron-binding motif comprising 2 His residues and a carboxylate side chain from either an Asp or Glu residue.[129, 130] These enzymes have been demonstrated to catalyze the halogenation of aliphatic carbons. The at the presence of halogenase, Fe$^{(II)}$, α-KG, O_2 and X^-.[104] SyrC, as the first α-ketoglutarate-dpendent halogenase isolated from *Pseudomonas syringae* biosynthetic gene cluster for the lipo-nonapeptidolactone syringomycin E,[131, 132] have all the requirements to perform as a α-ketoglutarate-dependent oxygenase. However, it showed chlorinating activity of the substrate.[131, 133] As the suggested mechanism shown in

Scheme 3.11, both halogenase and hydroxylase start with **A**, except that each hydroxylase has an aspartic acid or glutamic acid (Asp/Glu) replacing the Cl ligand. After binding the oxygen to the iron complex (**C**), α-KG undergoes decarboxylation and the active site forms a high energy $Fe^{(IV)}$-oxo intermediate (**D**). This high energy intermediate is able to abstract a H• from the unactivated carbon of a substrate. The resulting CH_2•, in proximity to the active site, abstracts the Cl• from the active site, rather than •OH. It was elucidated that the bonding between $Fe^{(III)}$ and O bond is stronger than $Fe^{(III)}$-Cl bonding and the orientation of CH_2• and the iron-bound Cl in the active site (**E**) is one essential factor. Radical rebound involves transferring Cl• to CH_2• to yield CH_2Cl,[134] the final product. In the hydroxylase active site, CH_2• abstracts the axial •OH. In the same way as halogenase, two radicals yield CH_2OH. Therefore, it was expected that this type of halogenase uses the same mechanism as the non-heme hydroxylase.

3.1.3.2 Flavin-Dependent Halogenases

The characterization of this class of halogenase was first established by van Pée and co-workers[135] when they successfully reconstituted PrnA activity *in vitro*. PrnA is known as the first enzyme in pyrrolnitrin biosynthetic pathway, first isolated from *Pseudomonas fluorenscens*, chlorinates at the 7 position of an L-Trp to give 7-Cl-Trp. It was found that both O_2 and FAD were required for this type of enzyme to function. In the reaction assay, FAD was presented as its reduced form $FADH_2$. It indicated that a flavin reductase and NAD(P)H were required in order to produce the halogenase activity (Scheme 3.12). The flavin reductase is an unspecific enzyme because reductase from *Pseudomonas* strain can be replaced by flavin reductase from other bacteria, such as *E. coli*.[135] In the two-component enzyme system, $FADH_2$ was under diffusion control between the two enzymes.

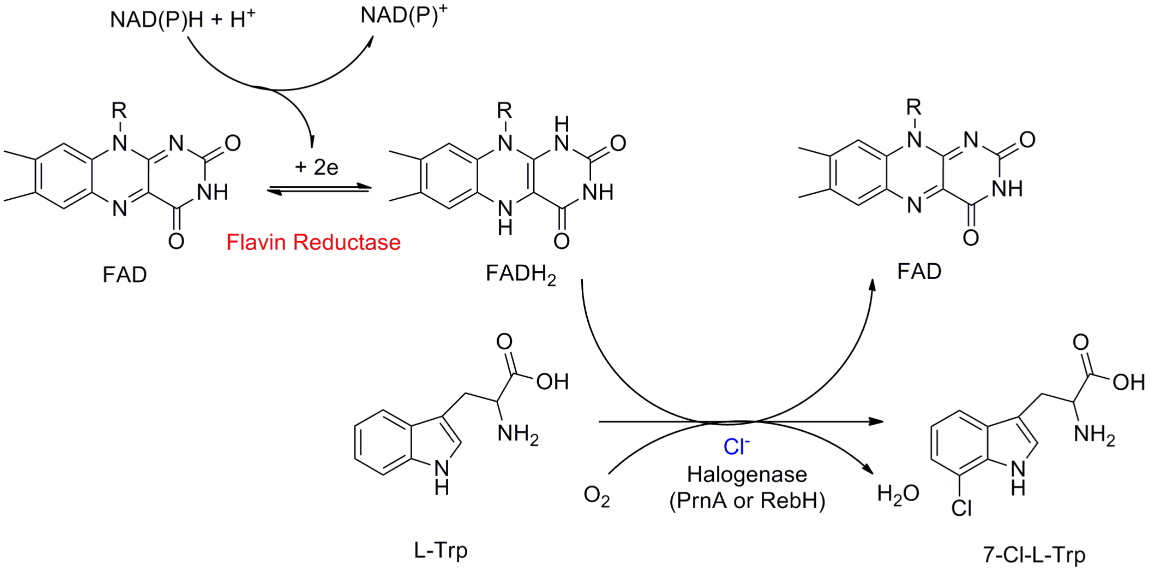

Scheme 3.12 The two-component enzyme system of flavin-dependent halogenases. Reverse the bottom chlorination reaction; the FADH2 to FAD arrow is against the chlorination arrow.

In addition to PrnA, several flavin-dependent halogenases have been reconstituted *in vitro*, including PltA from pyoluterorin biosynthesynthesis in *P. fluorescens* Pf-5[110], RebH from the chemotherapeutic agent rebeccamycin biosynthesis in *Lechevalieria aerocolonigenes*[136], KtzQ and KtzR from antifungal kutznerides in actinomycete *Kutzneria* sp. 744[39], SgcC3 from antitumor antibiotic C-1027 in *Streptomyces* *globisporus*[137], ThaL from thienodolin in *Streptomyces albogriseolus*[138] and PyrH from antibiotic pyrroindomycin in *Streptomyces globisporus*[139].

Flavin-dependent halogenase share high sequence homology with flavoprotein monooxygenases. Such flavoprotein also relies on the two-enzyme system to function, but usually the flavin reductase and monooxygenase are fused together in one protein. However, separate flavin reducase and monooxygenase systems are still found.[140-144] Because of the high homology in sequences and the similarity in requirements for the enzyme to show activity *in vitro*, the mechanism of flavin-dependent halogenases has been suggested based on the extensively studied mechanism of flavin-dependent monooxygenases.

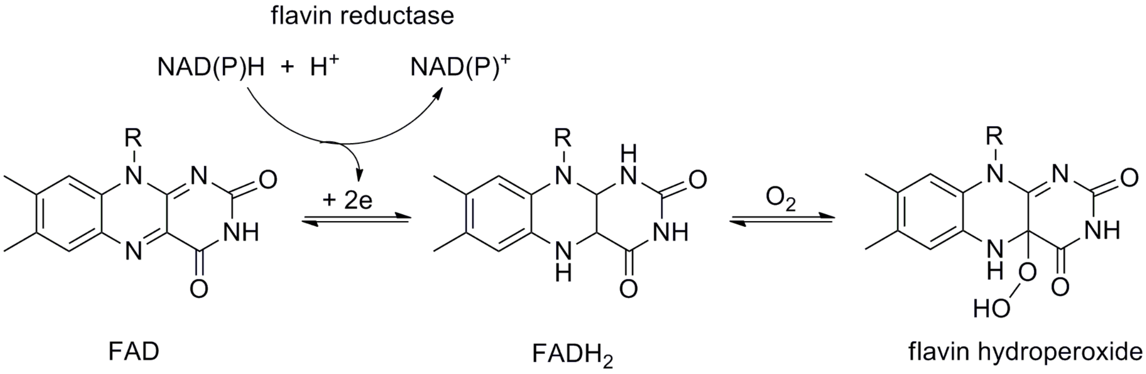

Scheme 3.13 Oxidation of $FADH_2$.

As shown in Scheme 3.13 the mechanism shown involves FAD reduced to $FADH_2$ by flavin reductase and NAD(P)H, followed by reacting with oxygen regiospecifically to give flavin hydroperoxide, also called FAD-C4a-OOH hydroperoxyflavin adduct. Both flavin-dependent monooxygenases and flavin-dependent halogenases use this flavin hydroperoxide intermediate. It was known that the production of flavin hydroperoxide is independently of substrate, as proposed by Walsh and coworkers who showed that the rates of flavin hydroperoxide formation in RebH were comparable in the presence and absence of tryptophan.[140] In flavin-dependent monooxygenases, the (-OH) group of flavin hydroperoxide is an (+OH) equivalent and is able to be delivered to the electron rich motif of a substrate, located at certain position of the enzyme active site.[145] In halogenases, a Cl^- can either react with the distal oxygen of FAD-C4a-OOH to give HOCl, or react with proximal oxygen to give FAD-OCl. Both of them are (Cl^+) equivalents.

Before concluding that flavin-dependent halogenases use a (Cl+) equivalent as an electrophile to react with the substrate, Cl^-, FAD-C4a-OCl and HOCl are the three possible chlorinating reagents. Cl- was eliminated right away because it does not agree with fact that halogenases require electrophilic species, not nucleophile, in the catalytic process. FAD-C4a-OCl was suggested to be the chlorinating reagent because HOCl was thought to be non- substrate specific enough due to its high reactivity.[136] However, with more studies, FAD-C4a-OCl was eliminated based on the stop flow experiments of RebH.[136] RebH is one of the first flavin-dependent halogenases studied and shares high sequence homology with PrnA. From the experiments, it was found the completion of FAD re-formation was detected prior to the formation of 7-Cl-Trp.[146, 147] If FAD-C4a-OCl was the chlorinating reagent, 7-Cl-Trp would not form after FAD formation was completed. 7-Cl-Trp would have formed somewhere in between the formation of FAD-C4a-OCl and FAD. This result suggested that HOCl is possibly the real chlorinating agent to L-Trp. Studies showed that according to PrnA crystal structures [148], a 10 Å long channel is available leading HOCl into the active site to where the substrate is bound. The side chain of K79 located close to L-Trp is proposed by van Pee and Naismith to position HOCl by hydrogen bonding in a specific orientation to react with the C7 of the L-Trp.

As mentioned previously, amino acid residue K79, residing nearby the active space is able to activate Cl to be more electrophilic by forming a chloramine. Walsh and coworkers[149] have shown the existence of a long-lived chloramine intermediate in the chlorination of tryptophan by RebH. It was also shown that formation of chloramine in the active site is independent of tryptophan or FAD. There are two possible mechanisms reported so far. Both reached the consensus that K79 is essential for forming chloramine to do electrophilic aromatic substitution on L-Trp. Yeh, et al.[149] suggested that not only K79 helped forming chloramines, it is also important to the overall enzyme structure by forming a H-bonding with the hydroxyl group of S347. [149] In the other case, shown in Scheme 3.14. E346 was involved in stabilizing the Wheland intermediate via π orbital and glutamate anion interation.[148]

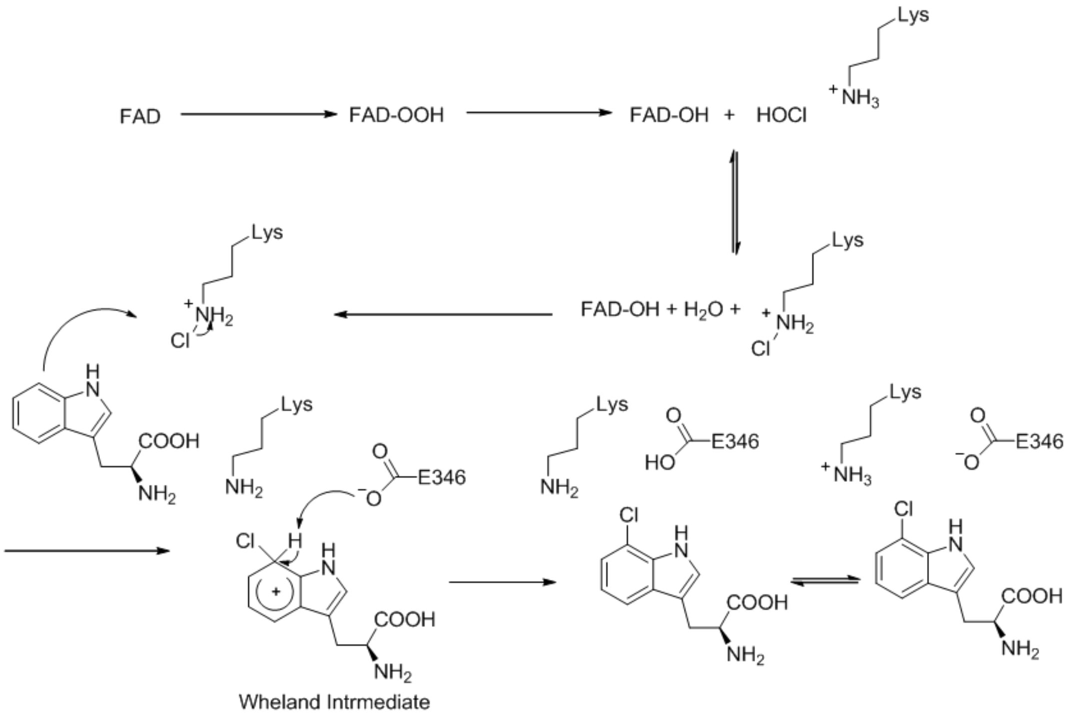

Scheme 3.14 Suggested mechanism of PrnA.

3.1.4 Characterization of PrnA and RebH

The crystal structure of PrnA has been reported by van Pée and coworkers[148] (Fig. 3.1). PrnA is a homo dimer composed of two identical pyramidal shaped monomers. Each monomer has binding sites for a FAD, an L-Trp and a Cl^- ion. Flavin binds to the solvent-exposed groove. It was reported that only flavin binding site is conserved in flavin-dependent halogenases. Cl^- binds to a pocket on one face of the $FADH_2$ ring. L-Trp and 7-Cl-Trp are bound in the pyramid shaped monomer (Fig.3.2). Now that the kinetic parameters for PrnA have already collected, but at the beginning of PrnA chatacterization, it was found that PrnA had low activity *in vitro*, which means it required more detailed studies in order to obtain full kinetic characterization. In order to study PrnA and the flavin-dependent halogenases, RebH was studied by Walsh and coworkers.[38] RebH is another flavin-dependent halogenase isolated from rebeccamycin biosynthesis in *Lechevalieria aerocolonigenes*[136]. It uses L-Trp as the substrate, shares 53% sequence identical and 67% similar to PrnA sequence (Fig. 3.3). RebH has its native flavin reductase RebF, interacts with RebH in a 3:1 ratio. Kinetic study showed that k_{cat} for RebH = 1.4 min^{-1} and K_M for L-Trp = 2.0 μM. Later one for PrnA, van Pée and coworkers[50] reported $k_{cat} = 0.093 \pm 0.03$ min^{-1} and $K_M = 160 \pm 40$ μM.

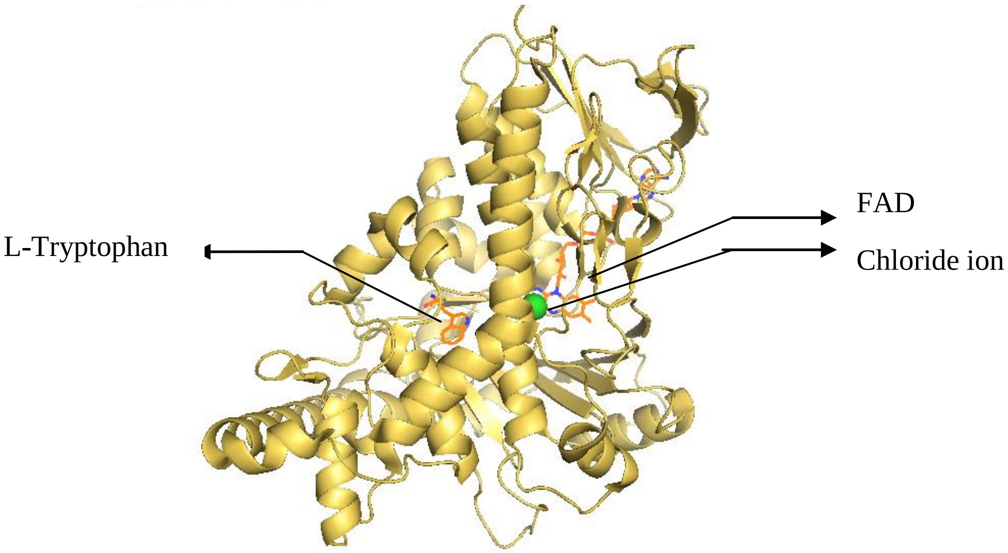

Figure 3.1 The monomer structure of PrnA. Each monomer contains binding sites for L-Trp, FAD and Cl^-.

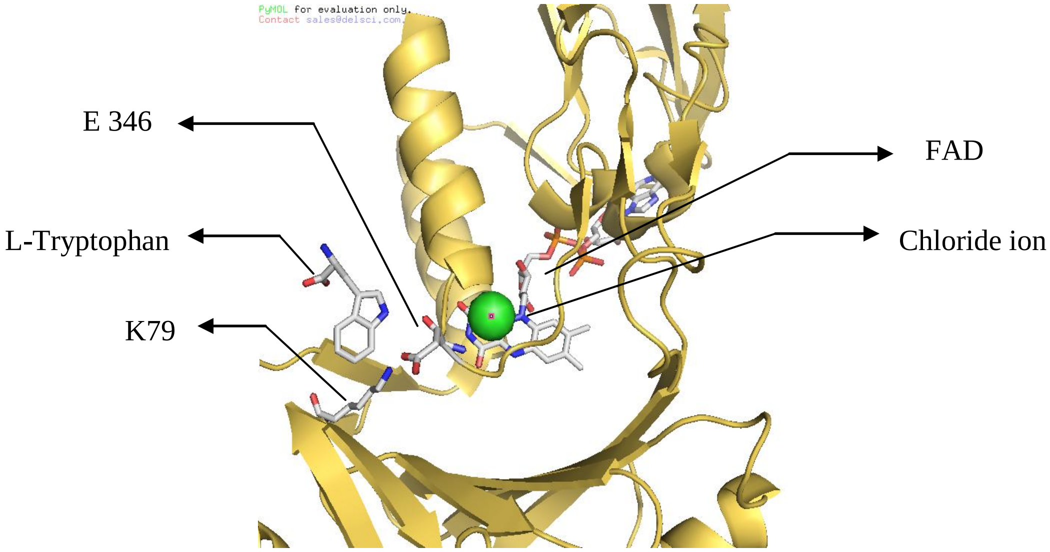

Figure 3.2 A close up at the active site of PrnA, E346 and K79 are considered to be the active site residues.

PrnC, introduced in section 3.1.1, is related to PrnA because they are both flavin-dependent halogenases in PRN biosynthetic pathway. From the sequence alignment, PrnC conserves the amino acid K79, suggested to be responsible for accepting HOCl to form chloamine, in the active site. In Figure 3.3, conserved K79 and conserved W 272 and W274 motif are highlighted in yellow, framed in red boxes. PrnA and RebH are high in homology than they are with PrnC. However, PrnC and other flavin dependent halgenases, such as CalO3 and CRpH, are high in homology. Both PrnC and PrnA contain a flavin binding site and this site show weak sequence homology to flavin-dependent monooxygenase enzymes 4-hydroxybenzoate 3-monooxygenase from *Burkholderia cenocepacia* (J2315) (Fig. 3.4). Due to the conserved K79 in the active site, sequence homology between PrnA and PrnC, and that fact that PrnC is flavin-dependent, it is hypothesized PrnC shares the same mechanism as PrnA.

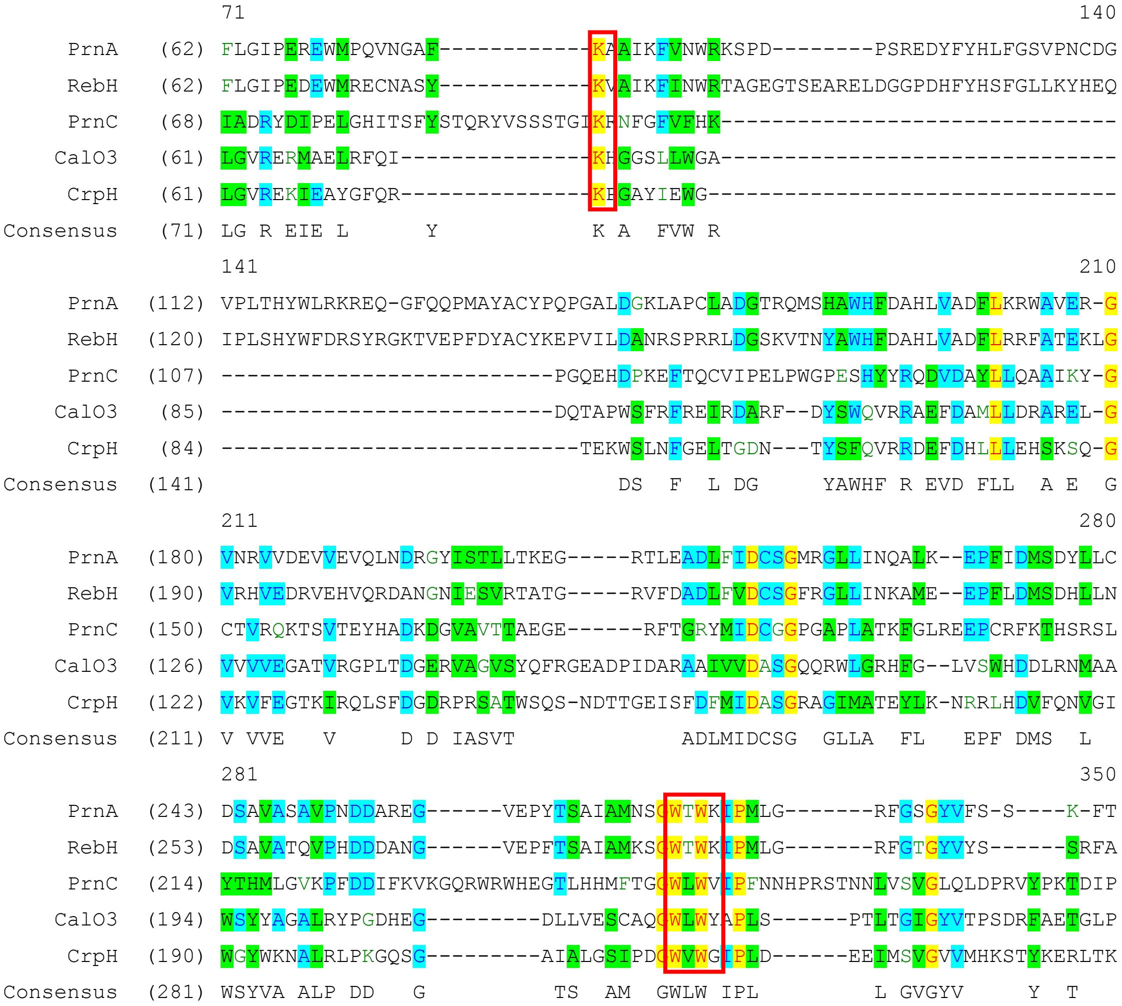

```
                71                                                                 140
     PrnA  (62) FLGIPEREWMPQVNGAF------------KAAIKFVNWRKSPD--------PSREDYFYHLFGSVPNCDG
     RebH  (62) FLGIPEDEWMRECNASY------------KVAIKFINWRTAGEGTSEARELDGGPDHFYHSFGLLKYHEQ
     PrnC  (68) IADRYDIPELGHITSFYSTQRYVSSSTGIKRNFGFVFHK-------------------------------
    CalO3  (61) LGVRERMAELRFQI---------------KHGGSLLWGA-------------------------------
     CrpH  (61) LGVREKIEAYGFQR---------------KEGAYIEWG--------------------------------
Consensus  (71) LG R EIE L      Y            K A  FVW R
                141                                                                210
     PrnA (112) VPLTHYWLRKREQ-GFQQPMAYACYPQPGALDGKLAPCLADGTRQMSHAWHFDAHLVADFLKRWAVER-G
     RebH (120) IPLSHYWFDRSYRGKTVEPFDYACYKEPVILDANRSPRRLDGSKVTNYAWHFDAHLVADFLRRFATEKLG
     PrnC (107) --------------------------PGQEHDPKEFTQCVIPELPWGPESHYYRQDVDAYLLQAAIKY-G
    CalO3  (85) --------------------------DQTAPWSFRFREIRDARF--DYSWQVRRAEFDAMLLDRAREL-G
     CrpH  (84) ----------------------------TEKWSLNFGELTGDN---TYSFQVRRDEFDHLLLEHSKSQ-G
Consensus (141)                                DS  F  L DG     YAWHF R EVD FLL  A E  G
                211                                                                280
     PrnA (180) VNRVVDEVVEVQLNDRGYISTLLTKEG-----RTLEADLFIDCSGMRGLLINQALK--EPFIDMSDYLLC
     RebH (190) VRHVEDRVEHVQRDANGNIESVRTATG-----RVFDADLFVDCSGFRGLLINKAME--EPFLDMSDHLLN
     PrnC (150) CTVRQKTSVTEYHADKDGVAVTTAEGE------RFTGRYMIDCGGPGAPLATKFGLREEPCRFKTHSRSL
    CalO3 (126) VVVVEGATVRGPLTDGERVAGVSYQFRGEADPIDARAAIVVDASGQQRWLGRHFG--LVSWHDDLRNMAA
     CrpH (122) VKVFEGTKIRQLSFDGDRPRSATWSQS-NDTTGEISFDFMIDASGRAGIMATEYLK-NRRLHDVFQNVGI
Consensus (211) V VVE   V     D D IASVT             ADLMIDCSG  GLLA  FL   EPF DMS  L
                281                                                                350
     PrnA (243) DSAVASAVPNDDAREG------VEPYTSAIAMNSGWTWKIPMLG-------RFGSGYVFS-S----K-FT
     RebH (253) DSAVATQVPHDDDANG------VEPFTSAIAMKSGWTWKIPMLG-------RFGTGYVYS------SRFA
     PrnC (214) YTHMLGVKPFDDIFKVKGQRWRWHEGTLHHMFTGGWLWVIPFNNHPRSTNNLVSVGLQLDPRVYPKTDIP
    CalO3 (194) WSYYAGALRYPGDHEG---------DLLVESCAQGWLWYAPLS------PTLTGIGYVTPSDRFAETGLP
     CrpH (190) WGYWKNALRLPKGQSG---------AIALGSIPDGWVWGIPLD------EEIMSVGVVMHKSTYKERLTK
Consensus (281) WSYVA ALP DD   G          TS  AM  GWLW IPL         L GVGYV     Y  T
```

Figure 3.3 Sequence alignment of RebH from *Lechevalieria aerocolonigenes* (BAC15758), PrnA (AAP88294), PrnC (ACF60536) from *Pseudomonas fluorenscens* CalO3 from *Micromonospora echinospora* (AAM70353) and CRpH from *Nostoc sp. ATCC 53789* (ABM21576).

Shown in Figure 3.3, PrnA and RebH are high in homology than they are with PrnC. However, PrnC and other flavin dependent halgenases, such as CalO3 and CRpH, are high in homology.

```
PrnA      TADFLKLWGLSDNQQLNQINFRVGRNKRAWVNNCVSIGLSSCFLEPLESTGIYFIYAALY 358
PrnC      CXXXXXXXXFSSNACVGDR-YCLMLHANGFIDPLFSRGLENTAVT---------IHALAA 326
FMO       TQKSVTPMRSFVSETMQHGRLFLAGDAAHIVPPTGAKGMNLAVAD---------VRALSR 312
                      .  : .    :  .    :    : *:.              : *
```

Figure 3.4 Sequence alignment of flavin binding sites (shown in green) of 4-hydroxybenzoate 3-monooxygenase (FMO) from *Burkholderia cenocepacia* (J2315), PrnA and PrnC from *Pseudomonas fluorenscens*. Green highlights the flavin binding region of PrnA, PrnC and FMO.

3.2 Objective

There are several benefits to using halogenases as opposed to chemical halogenation to install halogen atoms on drugs, or potential drugs, to modulate and/or optimize their interactions with receptors or other targets. Most importantly, halogenases can regioselectively[103] install halogens on non-activated substrates,[104] and the reaction is relatively environmentally friendly. Because natural organohalides produced from the enzymatic halogenations are useful in broad areas, such as agriculture and medicine, their *in vitro* mechanisms are of much interest.

In this study, we aimed to clone the genes encoding the two halogenases of the pyrrolnitrin biosynthetic pathway, PrnA and PrnC, over-express them in *E. coli*, and isolate and purify the enzymes such that their activities can be reconstituted. In particular, we are keen to understand the mechanisms of these enzymes and the strategies which they employ to obtain the regioselectivity observed in the chlorination of L-Trp by PrnA and MDA by PrnC.

3.3 Methodology

3.3.1 Materials

The pET-28a(+) vector and *E. coli* BL21(DE3) cells were purchased from Novagen. *E. coli* XL1-Blue cells were from Stratagene. The genomic DNA of *P. fluorescens* Pf-5 was purchased from ATCC (BAA-477D). Restriction enzymes, T4 DNA ligase and calf intestine alkaline phosphatase (CIAP) were purchased from Fermentas. Oliogonucleotide primers were from Sigma-Genosys. *Pfu* Turbo DNA polymerase was from Stratagene. QIAquick OCR Purification Kit and QIAprep Spin Miniprep Kit were purchased from Qiagen. L-Tryptophan, NADH, FAD and kanamycin (kan) were purchased from Sigma-Aldrich. Isopropyl β-D-1-thiogalactopyranoside (IPTG) was purchased from Invitrogen. Luria Bertani (Millar) agar and Luria Bertani (Miller) broth, sodium chloride, Tris-base, yeast extract, tryptone and glucose were purchased from Fisher Biosciences. DNA sequencing was carried out by Robarts Research Institute (London, Ontario) and the TCAG sequencing facility (The Hospital for Sick Children, Toronto, Ontario). Ni-NTA resin and Sephacryl S-200 resin were purchased from GE-Healthcare.

3.3.2 Cloning of *prnC* and *prnA* into pET-28a(+)

This work was carried out by Amélie Ménard. The *prn* genes were PCR-amplified from *P. fluorescens* Pf-5 genomic DNA. The oligonucleotide primer 5’-

GCCATATGATGAACAAGCCAATCAAGAATATC-3’ (*Nde*I restriction site is underlined) and 5’-GTGCGGCCGCCTACTGGCGTTCCTGAG-3’ (*Not*I restriction site is underlined) were used for the amplication of *prnA* and 5’-GCCATATGATGACTCAGAAGACCC-3’ (*Nde*I restriction site is underlined) and 5’-GTGCGGCCGCCTACTTCTTCAGAGCC-3’ (*Not*I restriction site is underlined) were used for the amplication of *prnC*. The genes were amplified with *Pfu* Turbo DNA polymerase (hot-start) using the following program: 4 min at 94 ºC, 30 cycles of 0.5 min at 94 ºC, 0.5 min at 58 ºC, 1.5 min at 72 ºC and a final elongation of 5 min at 72 ºC. The amplified genes were verified by agarose gel electrophoresis and PCR products with the correct molecular weights were purified. Double digests were then performed with the purified *prnA* and *prnC* PCR products and pET-28a(+) plasmids with *Nde*I and *Not*I restriction enzymes. Each *prn* gene was then ligated into the corresponding *Nde*I and *Not*I sites of pET-28a(+) using T4 DNA ligase. *E. coli* XL1-Blue cells were transformed with each ligation mixture. The heat denature ligation (1 μL) was added to 100 μL of competent cells, incubated on ice for 30 min, followed by heat shock at 42 ºC for 40 sec. It was cooled immediately on ice and continue incubating on ice for 5 min. 100 μL of transformed cells were grown in 800 μL of SOC media (2% tryptone, 0.5% yeast extract, 10 mM NaCl, 2.5 mM KCl, 10 mM MgCl$_2$, 10 mM MgSO$_4$, 1% glucose) for 1 hr and concentrated in 100 mL SOC and transferred to LB solid media, with 50 μg/mL kan and 1% glucose. It was incubated for 15-16 hrs at 37 ºC. Colonies were picked up and gown in LB media with 1% glucose and 50 μg/mL kan for 15-16 hrs shaking. Cells were harvested and the plasmids were extracted and purified. Sequencing of both DNA strands of the purified plasmids confirmed the sequences of PrnA and PrnC. The final constructs contain a *kan* resistance gene, are under the control of T7 promoter and *lac* operator and are expressed as N-terminal His_6-tagged proteins.

3.3.3 Expression, Isolation and Purification of PrnA

PrnA with an N-terminal His_6 tag was expressed from *E. coli* BL21(DE3) heat shock competent cells (Novagen) that had been transformed with the *prnA* plasmid described above. Cells were grown in Luria-Bertani (LB) media with kan (50 μg/mL) and 1% glucose in an air shaker (250 rpm, 30 ^{o}C) until the A600 of the culture reached 0.6 to 0.8. At this point, the culture was cooled in ice for 30 minutes before it was induced with 1 mM IPTG. After incubation at 15 ºC for 12 hours, cells were harvested by centrifugation at 3500 × g at 4 ºC for 30 minutes. The cell pellet was then resuspended in Buffer A (50 mM tris-base, 10 mM imidazole, 300 mM NaCl, pH 7.2) and lysed with an Emulsiflex-C5 homogenizer (Avestin, Canada). The lysed cells were then centrifuged at 40,000 × g at 4 ºC for 30 minutes. The supernatant was passed through a Ni-NTA column pre-equilibrated with Buffer A at a flow rate of 1 mL/min. After washing with Buffer A untile the UV absorbance at 280 nm reached zero, the His_6 tagged PrnA was eluted with a flow rate of 5 ml/min along a gradient from 10 mM to 51 mM imidazole for 2 column volumes (CV), washed for 6 CV at 51 mM imidazole (10% of 500 mM imidazole), followed by another gradient from 51 mM to 500 mM imidazole over 20 CV and final wash at 500 mM imidazole for 5 CV using an AKTA Fast Performance Liquid

Chromatography (FPLC) (GE Healthcare Life Sciences, USA). The eluted fractions were analyzed by 12% sodium dodecyl sulfate polyacrylamide gel electrophoresis (SDS-PAGE) gels followed by Coomassie Blue G-250 staining. Fractions containing pure PrnA as demonstrated by SDS-PAGE analysis were pooled, concentrated with Millipore Amicon Ultra centrifugal ultrafiltration devices (10,000 MWCO). The concentration of purified protein was determined from the absorbance at 280 nm using the calculated extinction coefficient of ε_{280} = 100,770 M^{-1} cm^{-1} and calculated MW = 63,505.04 g/mol. The extinction coefficient and MW were calculated from the amino acid sequence of PrnA using the web-based ProtParam tool (http://ca.expasy.org/tools/protparam.html). Concentrated PrnA was stored in protein storage buffer containing 50 mM Tris-base, 300 mM NaCl and 50% glycerol, pH = 7.2, at 4ºC before use.

3.3.4 Expression, Isolation and Purification of PrnC

PrnC with a N-terminal His_6 tag was expressed from *E. coli* BL21(DE3) heat shock competent cells (Novagen) that had been transformed with the *prnC* plasmid above. Cells were grown in 2xYT media with kan (50 µg/mL) and 1% glucose in an air shaker (250 rpm, 30 ^{o}C) until the A600 of the culture reached 0.6 to 0.8. At this point, the culture was cooled in ice for 30 minutes before it was induced with 1 mM isopropyl β-D-1-thiogalactopyranoside (IPTG). After incubation at 15 ºC for 24 hours, cells were harvested by centrifugation at 3500 × g at 4 ºC for 30 minutes. The cell pellet was then resuspended in Buffer A (50 mM tris-base, 40 mM imidazole, 300 mM NaCl, 10% glycerol, pH 7.2) and lysed with an Emulsiflex-C5 homogenizer (Avestin, Canada). The lysed cells were then centrifuged at 40,000 × g at 4 ºC for 30 minutes. The supernatant was passed through Buffer A pre-equilibrated Ni-NTA column and after washing with Buffer A when UV absorbance at 280 nm is zero, the His_6 tagged PrnC was eluted at a flow rate of 1 mL/min with a gradient from 40 mM to 95 mM (12% 500 mM imidazole) for 2 column volumes (CV), washed for 6 CV, followed by another gradient from 95 mM to 500 mM imidazole over 20 CV and final wash at 500 mM imidazole for 5 CV at a flow rate of 5 ml/min using an AKTA Fast Performance Liquid Chromatography (FPLC) (GE Healthcare Life Sciences, USA). The eluted fractions were analyzed by 12% SDS-PAGE gels followed by Coomassie Blue G-250 staining. Fractions containing pure PrnC as demonstrated by SDS-PAGE analysis were pooled, concentrated with Millipore Amicon Ultra centrifugal ultrafiltration devices (10,000 23 MWCO). PrnC fractions containing inpurity shown at MW 28 kDa by SDS-PAGE analysis were pooled, concentrated with Millipore Amicon Ultra centrifugal ultrafiltration devices (10,000 23 MWCO) and then further purified by gel filtration using a Sephacryl S-200 column (1.6 cm x 60 cm; GE Healthcare, USA) pre-equilibrated with TB buffer (50 mM Tris-base, 300 mM NaCl and 10% glycerol, pH 7.2) at a flow rate of 1 mL/min and was eluted with TB buffer at a flow rate of 0.5 mL/min. The pooled fractions from the gel filtration column were concentrated by ultrafiltration (10,000 MWCO, Amicon). The concentration of purified protein was determined from the absorbance at 280 nm using the calculated extinction coefficient of ε_{280} = 46,785 M^{-1} cm^{-1} and calculated MW = 64,770.5 g/mol. The extinction coefficient and MW were calculated from the amino acid sequence of

PrnC using ProtParam, the web-based tool. Concentrated PrnC was stored in protein storage buffer containing 50 mM Tris-base, 300 mM NaCl and 50% glycerol, pH = 7.2, at 4ºC before use.

3.3.5 Flavin Reductase Activity

The *E. coli* flavin reductase Fre[150-152] was kindly provided by Dr. David Zechel's laboratory. Its concentration was calculated using the extinction coefficient of 27,055 M^{-1} cm^{-1} and molecular weight of 28,536.5 g/mol calculated from its amino acid sequence with the web-based ProtParam tool. The assay contained 0.2 μM Fre, 0.5 mM NADH and 1 μM FAD in 600 μL of 10 mM phosphate buffer at pH 7.0 in a total volume of 600 μL. The mixture of the all except Fre was incubated for 3 minutes before Fre was injected in a small volume (<10 μL). The initial rate was measured according to the rate of disappearance of NADH at wavelength of 340 nm over 5 minutes. Each assay was done in triplicate. All the assays were performed using Cary 300 Bio UV-visible Spectrophotometer with a Cary Temperature control.

3.3.6 Synthesis of 7-Chlorotryptophan, MDA and APRN.

The synthesis of 7-chlorotryptophan was carried out in a two-step sequence as shown in Scheme 3.15 from serine and 7-chloroindole as described in the literature.[153]

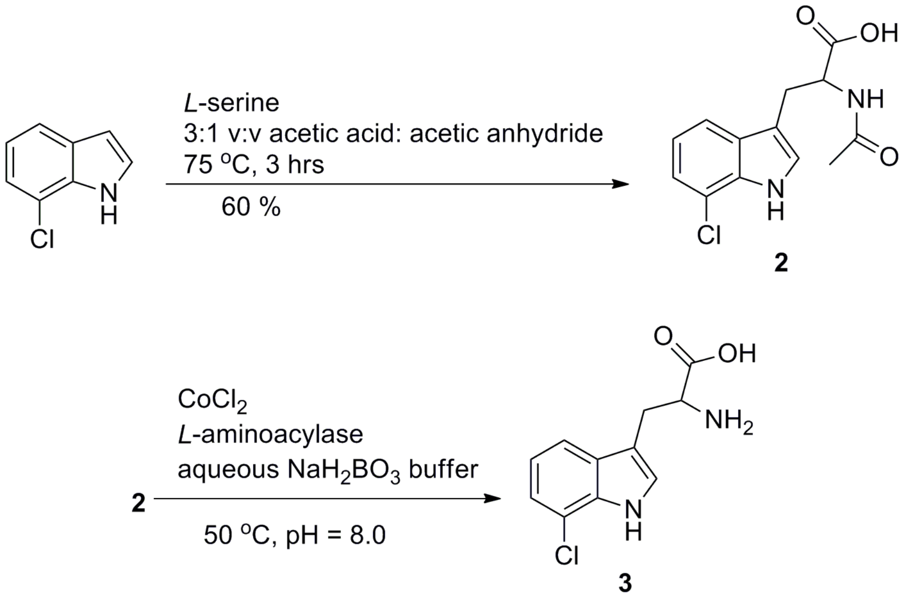

Scheme 3.15 Synthesis of 7-chloro-L-tryptophan.

APRN were prepared by a multistep procedure as described by Morrison et al. as shown in Scheme 3.16. MDA was prepared by Matthew Morrison as described in Morrison et al.[103]

.

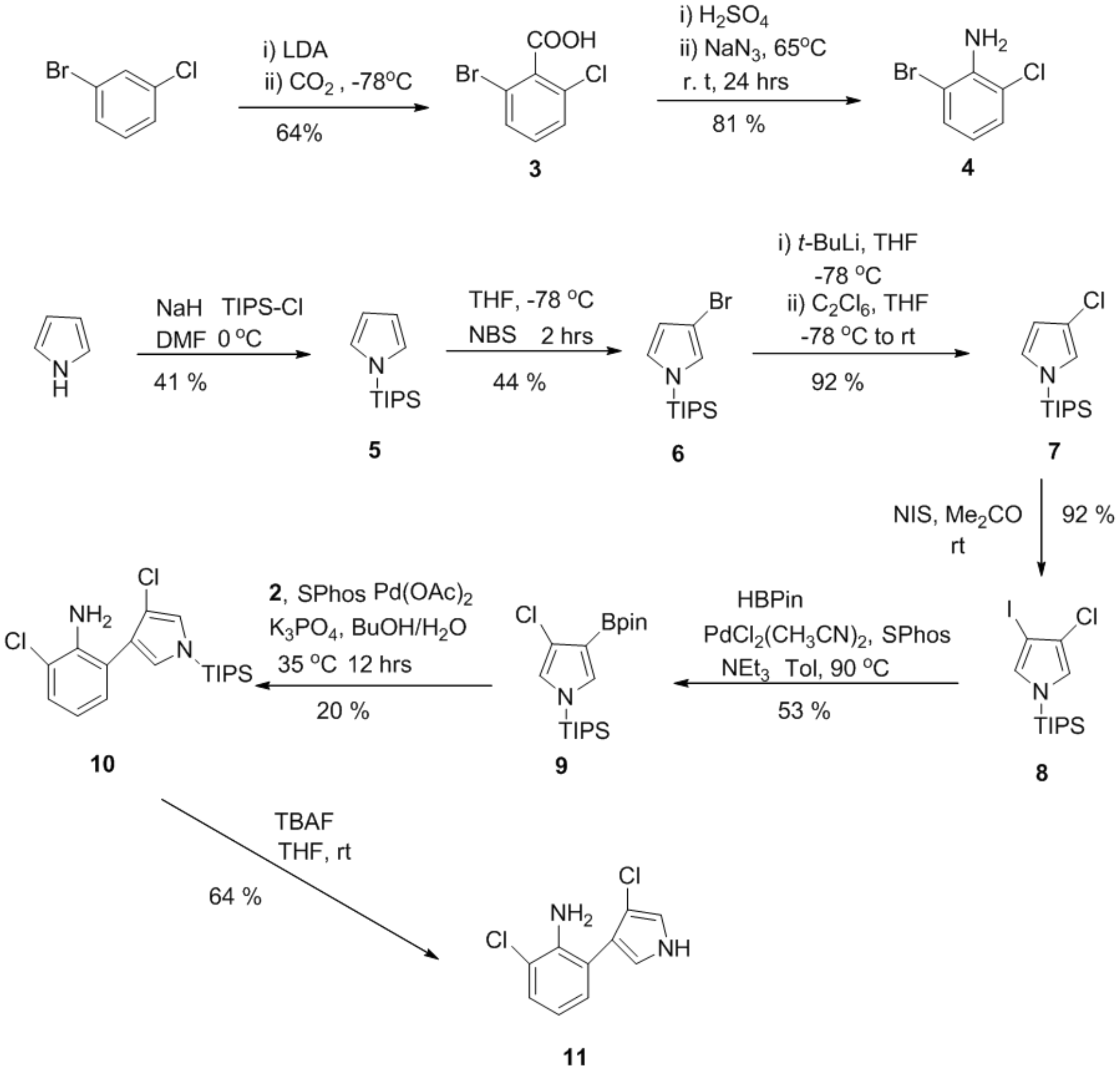

Scheme 3.16 Synthesis of aminopyrrolnitrin.

3.3.7 Response Factors for L-Trp, APRN and MDA using HPLC

A stock solution of L-Trp (36.3 mM) was diluted to 0.36 mM, 0.7 mM, 1.1 mM, 1.4 mM and 1.8 mM with 10 μL of 0.67 mM of 4-DCMA (Scheme 3.17) in 100 μL of 10 mM phosphate buffer at pH = 7.2 and the response of of L-Trp determined at 280 nm relative to 4-DCMA by reverse phase HPLC (Alliance Waters 2695 Separations Module with Waters 2996 Photodiode Array Detector) using a C18 column (Waters Nova, 4 μm, 3.9 x 150 mm). The solvent system was 40% methanol, 60% water and 0.1% TFA at a flow rate of 0.5 ml/min.

Concentrations of APRN and MDA were determined using 0.0945 M of 5-bromo-N,N-dimethylpyrimidin-2-amine (5-BDPA) (Scheme 3.17) as an internal standard to calibrate the exact amount of APRN and MDA within the stock according to proton integration from NMR spectrums.

A stock solution of APRN (0.127 M) was diluted to 0.25 mM, 0.51 mM, 0.76 mM, 1.02 mM and 1.27 mM with 15 mM benzylalcohol (BA). A stock solution of MDA (0.6189 M) was diluted to 0.62 mM, 1.24 mM, 2.47 mM, 3.71 mM and 4.94 mM with 15 mM BA in 10 mM phosphate buffer at pH=7.2. The responses of APRN and MDA relative to BA were measured at by 206 nm and 213 nm, respectively by Alliance Waters 2695 Separations Module with Waters 2996 Photodiode Array Detector using column from Waters, C18 xBridge^{TM} 2.5um, 4.6 x 75mm. The solvent system was 60% methanol and 40% water at a flow rate of 0.5 ml/min. PA of MDA and its internal standard BA was at 213 nm and PA of APRN and its internal standard BA was at 206 nm, where MDA and APRN had the highest absorbance, respectively.

5-bromo-N,N-dimethylpyrimidin-2-amine (5-BDPA) 4-(Dimethylamino)cinnamaldehyde (4-DCMA)

Scheme 3.17 Structures of the internal standards.

3.3.8 Tryptophan Chlorination by PrnA

The *in vitro* assay of PrnA was carried out at 30ºC in an a heating block. Reaction assay contained 2.2 mg/mL PrnA, 10 μM FAD, 2.4 mM NADH, 12.5 mM $MgCl_2$, 0.6 mM L-Trp and 0.55 mU Fre in 10 mM phosphate buffer at pH 7.2 in a total volume of 200 μL. Aliquots of 50 μL reaction mixture was taken out and left in the freezer at -80ºC overnight. All the aliquots were thawed and heated at 95ºC for 5 minutes. 10 μL of 3.3 mM (4-dimethylamino)-cinnamaldehye (4-DCMA) was added to the each aliquot, followed by centrifugation at 13,000 g for 15 minutes (Fisher Scientific accuSpin^{TM} Micro) and the resultant clear solution (supernatant) was submitted to reverse phase HPLC (Alliance Waters 2695 Separations Module with Waters 2996 Photodiode Array Detector) using a C18 column (Waters Nova, 4 μm, 3.9 x 150 mm). The solvent system was 40% methanol, 60% water and 0.1% TFA at a flow rate of 0.5 ml/min.

3.3.9 MDA Chlorination by PrnC

The *in vitro* assay for PrnC contained 34.6 μM enzyme, 10 μM FAD, 2.4 mM NADH, 12.5 mM $MgCl_2$, 500 μM MDA, 0.55 mU/mL Fre, 32.9 U/mL catalase, 10 mM phosphate buffer pH at 7.0 in total volume of 450 μL. The FAD, NADH, $MgCl_2$, MDA , catalase and Fre were first combined, and the reaction was then initiated by adding PrnC and NADH in small volumes (< 20 μL). The assay was incubated over 3 hours at 30ºC in a shaker (New Brunswick Scientific Classic Series: C24KC Refrigerated Incubator Shaker). 50 μL aliquots were obtained every 30 minutes, followed by immediate incubation for 5 minutes at 95ºC to precipitate proteins and terminate the reactions. 10 μL of 15 mM BA was added to each sample once they were cooled to room temperature. Proteins contained in each aliquot were precipitated out by centrifugation at 13,000 g for 15 minutes (Fisher Scientific accuSpin^{TM} Micro). The resultant clear solution (supernatant) was submitted to was submitted to reverse phase HPLC (Alliance Waters 2695 Separations Module with Waters 2996 Photodiode Array Detector) using a C18 column (Waters Nova, 4 μm, 3.9 x 150 mm). The solvent system was 60% methanol and 40% water at a flow rate = 0.5 ml/min.

3.3.10 Kinetics of Chlorination of MDA by PrnC

When determining k_{cat} and K_M for an enzyme, the concentration of substrate [S] varies while the total enzyme concentration $[E]_T$ is usually constant and [S] is more than 10 fold greater than $[E]_T$.

Table 3.1 Variable Concentrations in Assay Conditions for PrnC kinetic study.

Concentration of MDA (μM)	**Concentration of PrnC (μM)**
20	*1.8*
30	*1.8*
40	*3*
50	*3*
60	*3*
100	*7*
180	*7*

Besides PrnC and MDA, the reaction contained 10 μM FAD, 2.4 μM NADH, 12.5 μM $MgCl_2$, 0.55 mU/mL Fre, 32.9 U/ml catalase in 10 mM phosphate buffer pH at 7.2 in total volume of 250 μL. The mixture of FAD, NADH, $MgCl_2$, MDA, catalase and Fre were combined and incubated at 30ºC for 2 minutes using a dry-heating block (Eppendorf ThermoStatplus). The enzymatic reaction was initiated by adding PrnC, together with NADH in small volumes (< 10 μL). Conditions for kinetics assay at various concentrations of MDA and PrnC are listed in Table 3.1 above. Aliquots were obtained at 0, 5, 10, 15 and 20 min for assays containing MDA of concentrations 20 and 30 μM and for assays containing 40-180 mM MDA, aliquots were obtained at 1, 2, 5, 10, 15 min, followed by immediate incubation at 95ºC for 5 min. 10 μL of 15 mM BA was added to each sample once they were cooled to room temperature.

Proteins contained in each aliquot were precipitated out by centrifugation at 13,000 g for 15 minutes (Fisher Scientific accuSpin^{TM} Micro) and the resultant clear solution was submitted to HPLC (Waters 1525 Binary HPLC bump with Water 996 photodiode Array Detector and Waters 717plus Auto-sampler). A reverse phase column Waters Nova C18, 3.9 x150 mm, 4 μm, was used. Mobile phase was 60% methanol and 40% water at a flow rate = 0.5 ml/min. Each assay repeated in triplets using PrnC from the one preparation of expression from 4 liters of culture.

3.4 Results

3.4.1 Over-expression and Purification of PrnA

PrnA was expressed as a C-terminal His$_6$ tagged fusion protein in *E. coli*. The soluble portion of PrnC was purified by FPLC using a Ni-NTA column (Figure 3.5 A). The bands from eluted fractions containing PrnA, as demonstrated by the 12% SDS-PAGE, confirmed the calculated mass of 63.5 kDa from amino acid sequence (Figure 3.5 B & C). The 2 L culture yielded soluble PrnA at 7-10 mg/L.

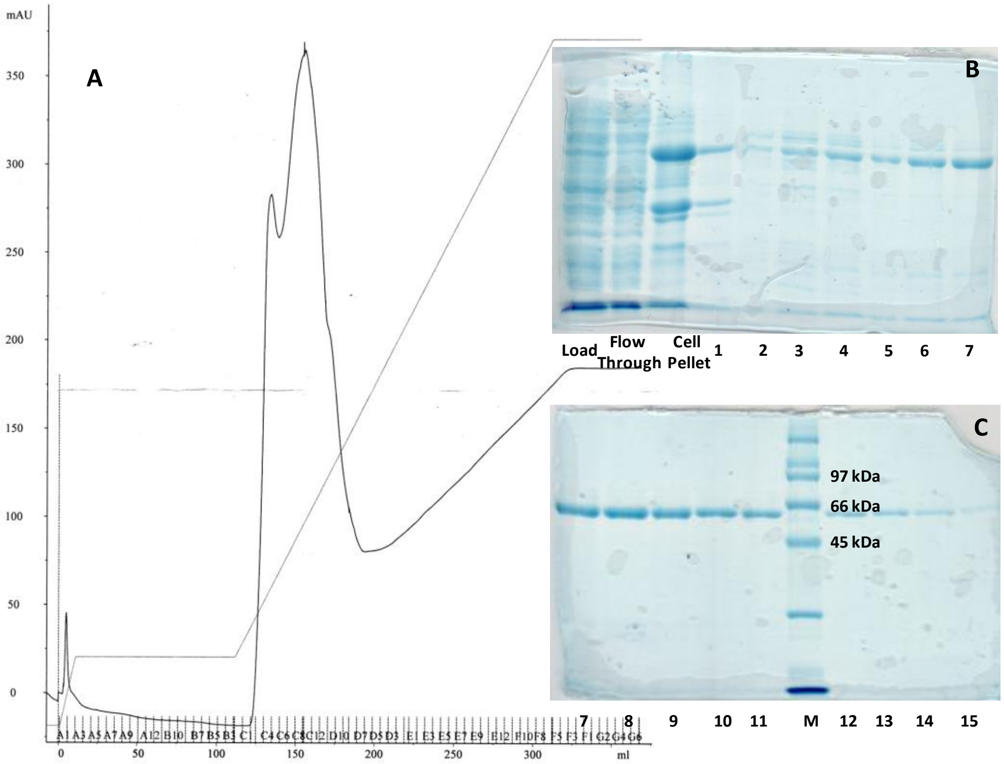

Figure 3.5 A. Chromatogram for purification of PrnA by Ni-NTA chromatography. UV-absorbance at 280 nm plotted on the Y-axis, fraction number (5 mL each) on the X-axis). B, C. SDS-PAGE gel (12%) showing the load, flow through, and cell pellet, as well as the collected fractions, numbered as such. Lane M shows the BioRad broad range marker.

3.4.2 Over-expression and Purification of PrnC

PrnC was expressed as a N-terminal His_6 tagged fusion protein in *E. coli*. The soluble portion of PrnC was purified using a Ni-NTA column of a FPLC system. The eluted fractions after FPLC contained relatively pure protein as demonstrated by SDS-PAGE. A calculated mass of 64.7 kDa from amino acid sequence was confirmed by most dominant band in the eluted fractions. (Figure 3.6 B & C). Fractions 1-10 contained proteins that co-eluted with PrnC, shown in Figure 3.6 B & C, were combined and concentrated to 1 ml, followed by further purification of gel filtration. The dominant peak (Figure 3.7 A) is PrnC. It was confirmed by SDSPAGE (Figure 3.7 B & C) as well as its purity. These fractions from gel filtration were combined and concentrated and its purity was further confirmed by SDS-PAGE. From 4 L culture we obtained 2-5 mg/L soluble recombinant PrnC.

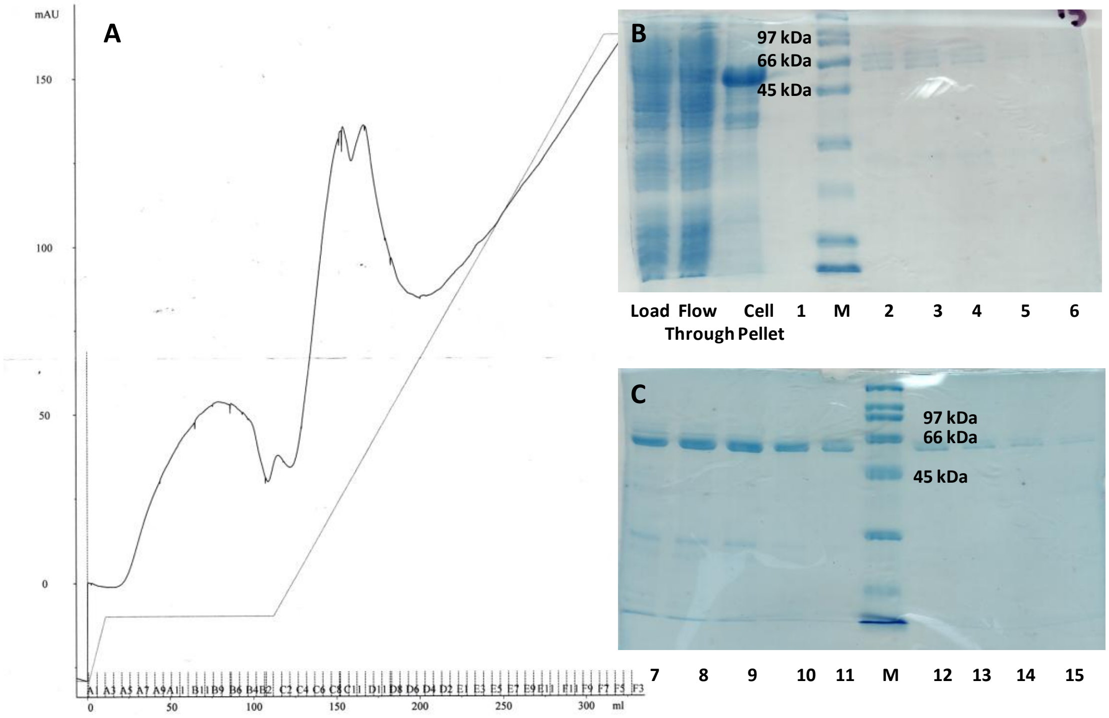

Figure 3.6 A. Chromatogram for purification of PrnC by Ni-NTA chromatography. UV-absorbance at 280 nm plotted on the Y-axis, fraction number (5 mL each) on the X-axis). B, C. SDS-PAGE gel (12%) showing the load, flow through, and cell pellet, as well as the collected fractions, numbered as such. Lane M shows the BioRad broad range marker.

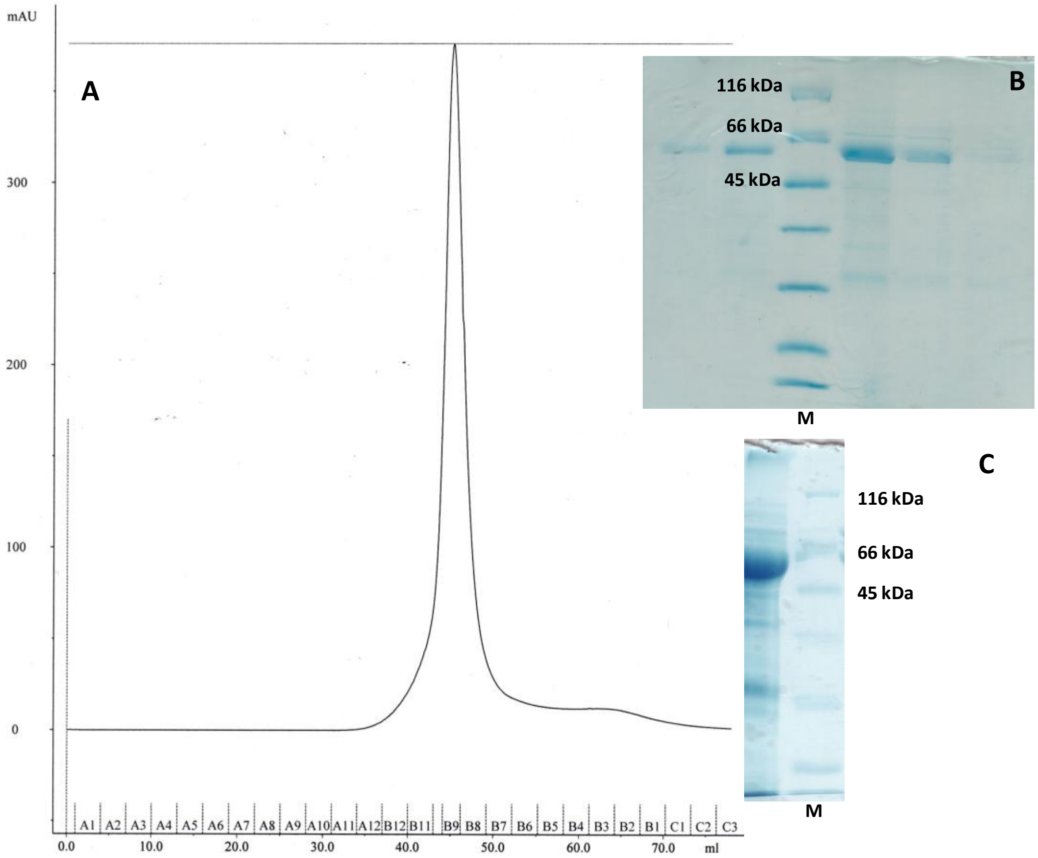

Figure 3.7 A. Chromatogram for purification of PrnC by gel filtration chromatography. UV-absorbance at 280 nm plotted on the Y-axis, fraction number (3 mL each) on the X-axis). The two SDS-PAGE gels shown are 12%. B. Fractions collected corresponding to the major peak in the chromatogram. C. Concentrated and combined fractions from B with M being the LabAid SM0431 Protein Molecular Weight Marker.

3.4.3 Synthesis of 7-Cl-Trp and APRN

The synthesis of 7-acetyl-Cl-Trp (**2**) was achieved in 60% yield, yielding a dark brown product. Sherman *et al*. reported the contaminant, α-acetamidoacrylic acid, found after the first flash chromatography with 95:5:1 CH_3Cl-MeOH-acetic acid was eliminated after a second chromatographic purification under the same conditions to afford a final yield of 83%. However, we did not find a second chromatographic step helped further purification of **2**. More silica gel was used in our case to obtain pure **2** with a 60% yield. The de-acylation of 2 will be performed in the future using an enzyme (de-acylase) as a catalyst.

For the synthesis of APRN, most of the yields are lower than what Morrison, et al. reported. However, experiments were performed in the same way as Morrison, et al. has described. There are two main reasons the yields were lower. One is experiments in our studies were performed on small (mg) scales, which usually comes with the problems of losing products while purifying when, especially, there are several purification steps, such as washing, extracting, chromatography and etc. The other main reason was that most of these reactions were successful at the first try, hence there were some experimental errors associated with lack of experience. Due to the fact that we are not looking for perfect yield, we carried on to achieve the final product. The final product APRN was purified by HPLC normal phase chromatography using 75% hexane and 25% ethyl acetate, instead of flash chromatography, the yield was comparable to Morrison, et al. reported: **3**(99%), **4** (92%), **5** (99%), **6** (90%), **7** (92%), **8** (92%), **9** (80%), **10** (85%) **11** (79%).

3.4.4 Response Factors for L-Trp, APRN and MDA

The response factors were determined using Eq. 3.1 where PA is the peak area and [substrate] and [internal standard] is the concentration of substrate and internal standard, respectively.

$$\frac{PA\ of\ Substrate}{PA\ of\ Internal\ Standard} = Response\ Factor\ \frac{[Substrate]}{[Internal\ standard]} \quad \text{Eq. 3.1}$$

Retention time for L-Trp was 4.9 min, for 4-DCMA was 11.1 min, determined from the HPLC with a solvent system of 40% methanol, 60% water and 0.1% TFA at a flow rate of 1 ml/min. According to Fig. 3.8, the response factor of L-Trp at λ=280nm against internal standard 4-DCMA is 0.4.

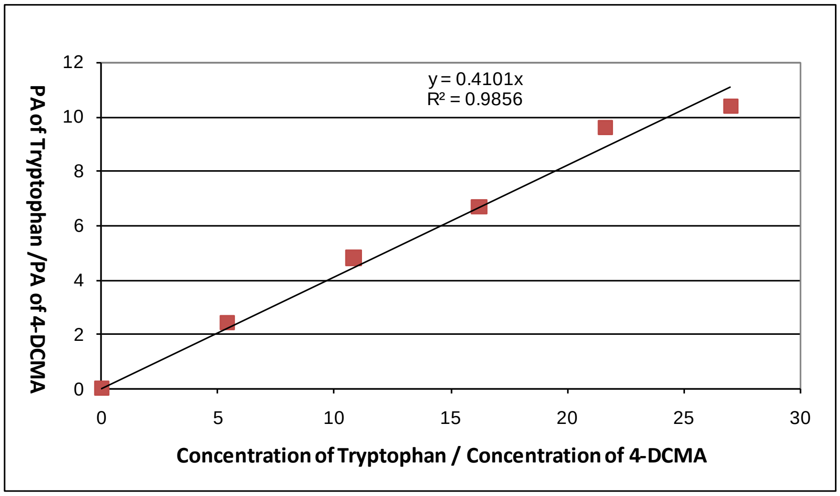

Figure 3.8 Response factor of L-tryptophan against 4-DCMA (0.067 mM) at 280 nm.

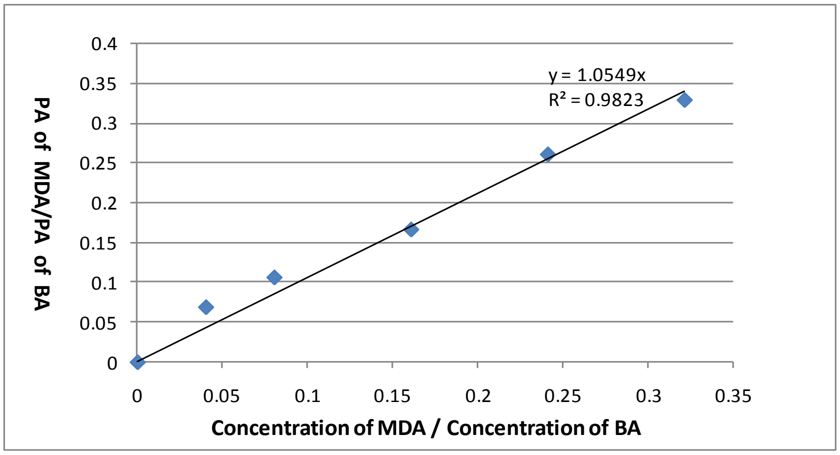

Figure 3.9 Response factor of MDA against BA (0.015 M) at 213 nm.

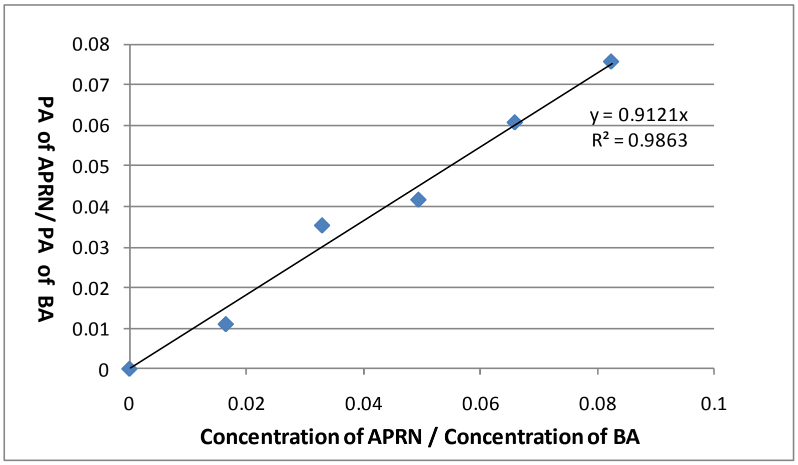

Figure 3.10 Response factor of APRN against BA (0.015 M) at 206 nm.

Retention time for MDA peaks was 6.6 min, for APRN was 8.7 min and for BA was 2.3 min, determined from the HPLC with a solvent system of 60% methanol and 40% water at a flow rate of 0.5 ml/min. According to Figure 3.9 and 3.10, the response factors of MDA at λ=213 nm and APRN at λ=206 nm against internal standard BA are 1.1 and 0.9, respectively.

3.4.5 PrnA *in vitro* assay demonstrated conversion of substrate 7-Cl-Trp.

Shown in Figure 3.12, 7-Cl-Trp generation was observed after 1 min of the reaction. In the next 40 minutes, the peak size of L-Trp at r.t. = 4 minutes reduced largely while the peak size of 7-Cl-Trp increased largely. When at 6 hours, peak of the L-Trp had nearly disappeared whereas peak size of 7-Cl-Trp increased. Fig 3.12, peak area (PA) (substrate)/PA (BA) versus time, demonstrated the reaction process in a quantitative way. The consumption of L-Trp happened rapidly over the first 40 minutes and a much slower rate afterwards. As for 7-Cl-Trp, it seemed to have reached its maximum production in the first hour of the reaction period. Over the next 5 hours, the amount of 7-Cl-Trp was still increasing, but in a slower rate.

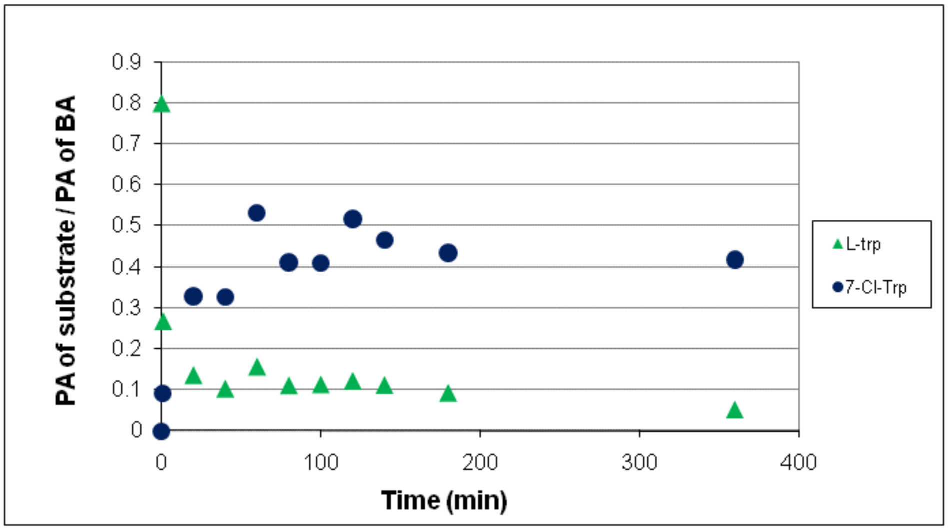

Figure 3.11 Time course for L-Trp reacting with PrnA, yielding 7-Cl-Trp. Assay conditions as described in the Methods section.

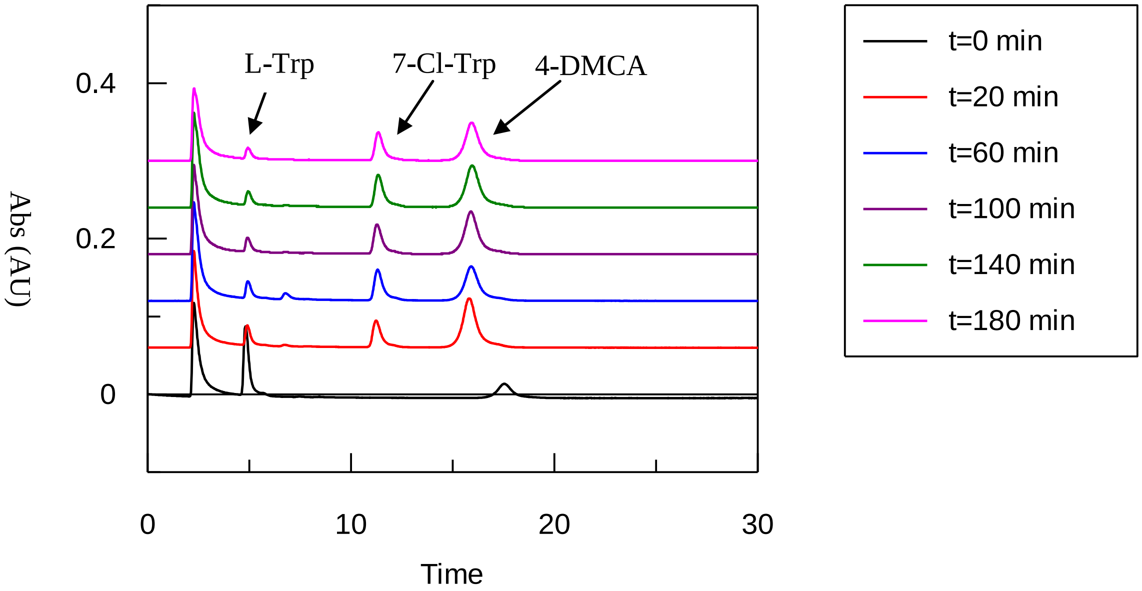

Figure 3.12 HPLC chromatography of aliquots from the *in vitro* PrnA assay for 3 hours.L-Trp has r.t. = 4.8 min and 7-Cl-Trp has r.t. = 11.3 min.

3.4.6 PrnC *in vitro* assay demonstrated complete conversion of substrate MDA.

As demonstrated in Figure 3.13, the peak of APRN at r.t. =19 minutes was observed at 1 min of reaction time. Over time, the peak size of APRN increased whereas the peak size of MDA at r.t. = 14 mins decreased. Quantitative data is shown in Figure 3.14. MDA was completely consumed over two and half hours. APRN was generated corresponded to the decreasing of MDA. Once all MDA was consumed over 150 minutes, the generation of APRN stopped and possibly due to the degradation of APRN, the amount of APRN started to decrease after 150 minutes. Based on the response factors calculated for MDA and APRN using BA as an internal standard, 0.0031 umol of APRN was generated using 0.0032 umol of MDA, which demonstrated a 97% conversion after 3 hours.

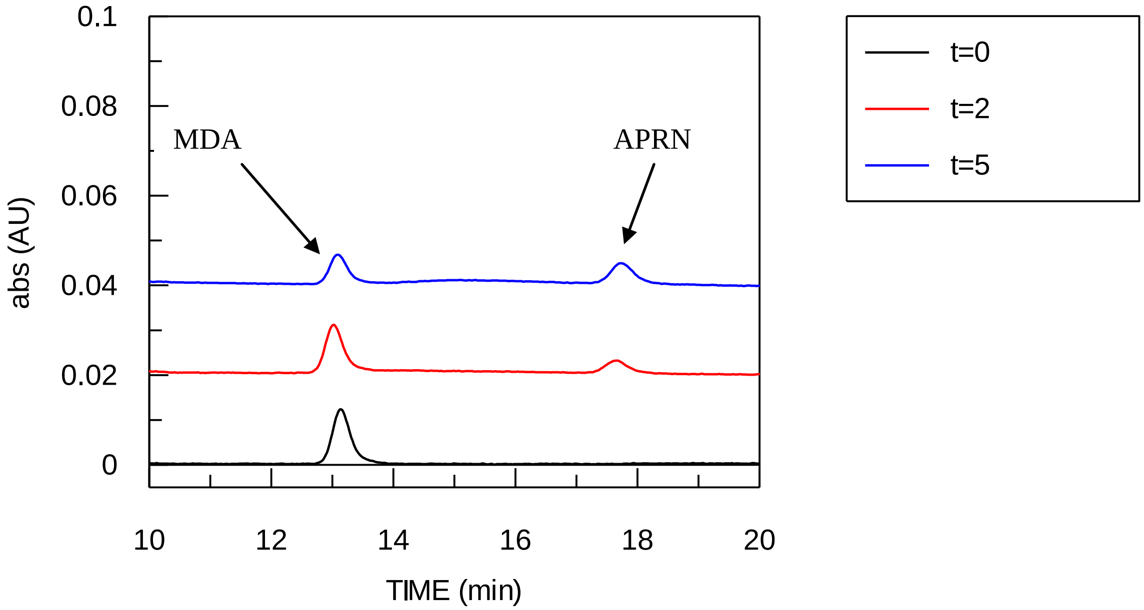

Figure 3.13 HPLC chromatography of aliquots obtained from the *in vitro PrnC* assay for 5 minutes. MDA has r.t. = 13.1 min and APRN has r.t. = 17.2 min.

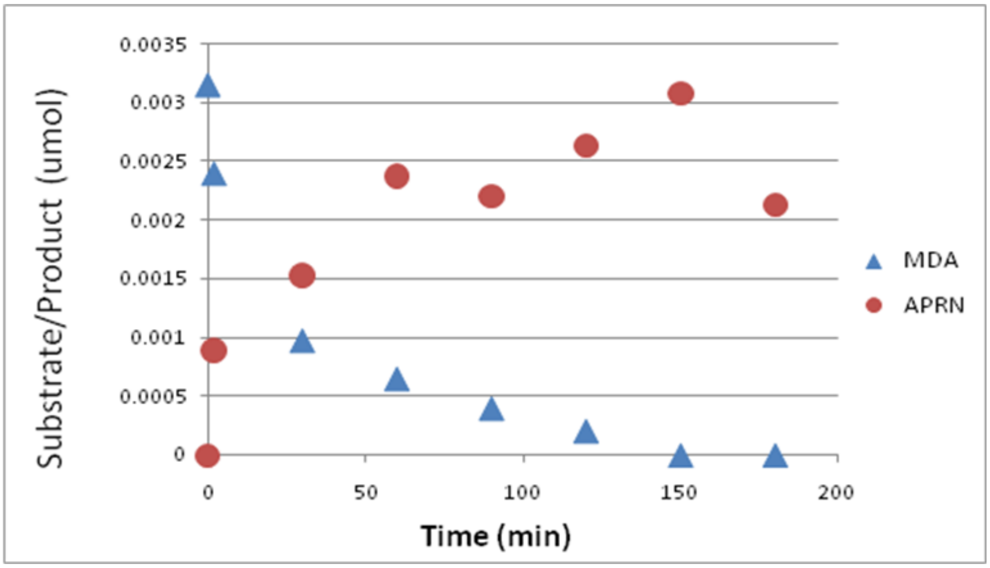

Figure 3.14 Time course for the reaction of MDA with PrnC, yielding APRN. Assay conditions described in the Methods section.

3.4.7 Determining k_{cat} and K_M for PrnC

A plot of reaction velocity, normalized for changes in total enzyme concentration, as a function of substrate concentration is shown in Figure 3.15. When the data were fit to the scheme for Michaelis-Menton kinetics, Eq. 3.2, v_{max} = 0.0765 min^{-1} and K_M = 23.6 µM with a standard error of 0.0053 min^{-1} and 3.7 µM, respectively. The data used for the fit is the first four points ([MDA] = 0, 20, 30, 40 µM) and the reduced chi^2 value is 5.8e-007.

$$v = \frac{v_{max} S}{K_M + S} \qquad \text{Eq. 3.2}$$

The data were also fit to the general scheme for substrate inhibition, Eq. 3.3, which showed a $v_{\max} = 0.0608\ \mathrm{min}^{-1}$, $K_{\mathrm{M}} = 11.2\ \mu\mathrm{M}$ and $K_{\mathrm{inh}} = 226.4\ \mu\mathrm{M}$ with standard error of $0.02\ \mathrm{min}^{-1}$, 9.0 μM and 145.4 μM, respectively. The data used to plot included all eight data points and the reduced chi^2 value is 0.0077.

$$v = \frac{k_{cat}[E]_T[S]}{K_M + [S] + [S]^2 / K_I} \qquad \text{Eq. 3.3}$$

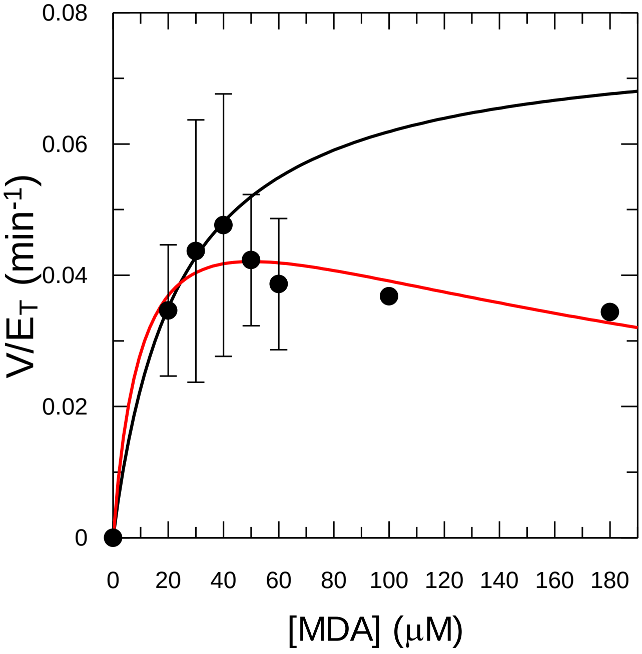

Figure 3.15 Kinetic analysis of reconstituted PrnC activity, fit to the Michaelis-Menten equation (Eq. 3.2, black) and the substrate inhibition equation (Eq. 3.3, red).

3.5 Discussion

The expression, isolation and purification of the enzymes of the pyrrolnitrin biosynthetic pathway in *E. coli* has been performed in this study. It is known that proteins tend to be largely insoluble in our hands, at least in the *E.coli* BL21 (DE3) strain that we used for over-expression, and may likely be the reason that the original work with the pyrrolnitrin biosynthetic gene cluster,[95] as well as the previous biochemical work with PrnA[148], was carried out in *Pseudomonas*. It should be pointed out that while recombinant protein expression in *E. coli* is largely carried out because of the low cost, ease of genetic manipulation and growth conditions, and the availability of vast amounts of literature which thoroughly characterizes its capabilities and limitations,[154] it is quite common that efforts lead to insoluble proteins. Insoluble proteins are basically misfolded proteins, and the aggregates of these misfolded proteins are commonly referred to as inclusion bodies. As shown in Figure 3.5 (B) and Fig. 3.6 (B) for PrnA and PrnC, respectively, a significant fraction of the protein remained in the cell pellet following cell lysis and centrifugation as inclusion bodies. PrnA and PrnC are, of course, not native *E. coli* proteins, but instead are native to the organism from which we cloned them, *P. fluorescens* Pf-5.[155] The difference in the cell species may also cause misfolding of the proteins. Because of the tendency of misfolding, it brought some difficulties to the purification process and harvesting larger amount of pure protein. Regardless, we were able to obtain sufficient quantities in sufficient purity to carry out preliminary investigations of their reconsitituted activities. Compared to the yield of 5 mg/litre by van

Pée, et al[156] from *P. fluorescens*, our yield of PrnA from expression in *E. coli* was 7 – 10 mg/L is comparable.

As shown in Figure 3.16 (A) our original attempt at the purification of PrnA isolated from cell culture was not overly successful. Besides the PrnA band, shown close to the 66 kDa of the marker, other proteins were expressed and co-eluted due to unoptimized expression conditions and unspecific protein binding to the Ni-NTA column.

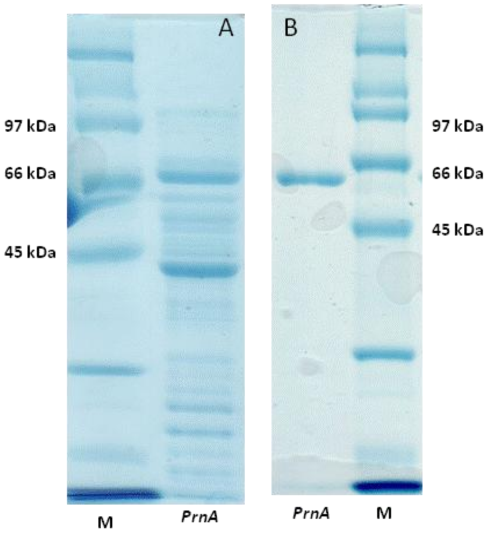

Figure 3.16 SDS-PAGE gel of purified PrnA from the past expression, isolation and purification method in this past study (A) and the optimized purification method (B) as described in the text.

Prompted by these results, we attempted to increase the expression of native proteins of *E. coli* by altering the expression conditions, i) cooling the cell culture in ice before inducing expression by adding IPTG, and ii) reducing temperature to 15 ºC for protein expression after IPTG induction. Low temperature growth slows recombinant protein expression and induces expression of folding chaperones, both of which can enhance soluble expression. IPTG, an analogue of lactose, is used as the repressor protein allosteric inhibitor. Prior to IPTG induction, cooling the cell culture at 0 ºC is to stop any cell activity, including cell propagation and plasmid propagation and induce chaperone expressionso so that it ensures that induction by IPTG happens after the completion of producing plasmids for the desired protein. This subsequently reduces the chance of inducing any non-desired protein expression. After IPTG was added, as the temperature drops to 15 ºC, it slows down the translation of mRNA to amino acid sequence, as well as the folding of the polypeptide. As the folding slows down, the secondary sequence has enough time to explore its favored tertiary structure rather than quickly folding to a structure at a higher temperature. When the folding of protein slows down, it could be problematic because hydrophobic region, which is supposed to be buried inside of protein, is exposed, subsequently increasing the chance of interacting with RNA, DNA and the neighbor polypeptides present in cells. *E. coli* native chaperones are upregulated when cells are under stress that leads to protein misfolding. They assist protein folding by stabilizing the partially folded protein, refolding unfolded proteins, dissolving aggregates and decomposing irreversible denatured peptides.[154]

Not only were the expression conditions modified, but also the purification protocol was modified based our previous attempts of PrnA purification. In order to decrease the amount of proteins co-eluting with PrnA, an immediate increase of imidazole concentration from 10 mM to 51 mM (10% of 500 mM imidazole) was achieved within 2 column volumes (CVs) after washing and was kept at 51 mM for another 6 CVs before starting PrnA elution with further increased imidazole concentration. Furthermore, the increase of CV for the final gradient from 51 mM to 500 mM to 20 CV slowed down the elution, allowing further washing off the non-specifically bound proteins from the resin in the first few collecting fractions. With the three modifications from expression and purification, indeed, the outcome of PrnA elution was highly pure (Figure 3.17 (A)) comparing to the final PrnA purity from the original method (Figure 3.17 (B)).

PrnC expression and purification methods were in the same way as PrnA's method based on our first few attempts of purification. However, due to the problematic co-elution of the unspecific binding proteins, shown in Fig. 3.18 (A), Ni-NTA purification protocol for PrnC had to be further revised.

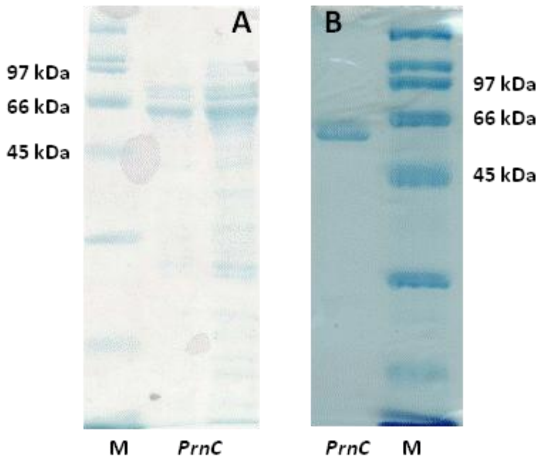

Figure 3.17 SDS-PAGE gel of purified PrnC from the past expression, isolation and purification method in this current study (A) and the optimized purification method (B) as described in the text.

The proteins shown below PrnC band on SDS-PAGE, in particular, the one around 30 kDa and lower bands, were easily purified by gel filtration. However, the proteins of similar size to PrnC were more difficult to remove. The purification of PrnC was based on that which we described for PrnA, above, with two modifications. Imidazole concentration was increased in Buffer A from 10 mM to 40 mM to pre-equilibrate the column and to load the supernatant of cell lysate. The increase concentration of imidazole enhanced its ability in competing with the non-specific binding protein in binding to the resin-bound Ni ions. The same logic as increasing imidazole concentration in Buffer A, when elution started, an immediate increase of imidazole concentration from 40mM to 95 mM (12% of 500 mM imidazole) was achieved to further remove proteins which were bound non-specifically before eluting

PrnC. As shown in Fig. 3.18 (B), these adjustments of the expression and purification methods dramatically improved the purity of the PrnC, especially in the later fractions. Preliminary attempts to crystallize PrnC have been encouraging, and are being pursued by Kateryna Podzelinska of the Queen's University Department of Biochemistry.

Before carrying out kinetic studies on PrnC, we performed *in vitro* assays on PrnA using the conditions that were described by van Pée, et al for PrnA expressed in *P. fluorescens* BL 915.[148]. As demonstrated in Fig. 3.11 and 3.12, PrnA was able to cleanly convert L-Trp to 7-Cl-Trp, as evidenced by HPLC. While this qualitative observation is an important control experiment demonstrating that PrnA expressed in *E. coli* is indeed active, we cannot compare the activity of this enzyme to that reported by van Pée and co-workers[148] on the PrnA expressed in *Pseudomonas.* In order for such a comparison to be made, a response factor for 7-Cl-Trp has to be determined so that the exact number of moles of L-Trp consumed and 7-Cl-Trp generated can be evaluated and the reaction rate calculated. Unfortunately, the previously synthesized 7-Cl-Trp in our laboratory had degraded over time according to NMR spectroscopy and HPLC.

We next carried out preliminary assays of PrnC activity using the same reaction conditions that were effective in the reconstitution of PrnA activity discussed above. Unfortunately, no conversion of MDA to APRN was observed by HPLC over 6 hours. Since the kinetic parameters for another flavin-dependent halogenase, RebH, were reported only in the presence of the hydrogen peroxide decomposing enzyme catalase, we next attempted the assay wherein we included catalase in the reaction mixture. Indeed, one of the common problems with flavin-dependent, and other oxidative enzymes, is the oxidation of the enzyme by reactive oxygen species (ROS) formed during turnover. In the case of flavins, due to the intermediacy of flavin hydroperoxide, oxidation by H_2O_2 is most common. To avoid oxidation by H_2O_2 catalase is included in the assay to break down H_2O_2 into water and oxygen. Gratifyingly, activity of PrnC was observed once catalase was included in the reaction mixture, and 97% conversion of MDA to APRN was observed within 2 hours. As shown in Fig. 3.15, MDA was directly and completely converted to APRN with no intermediates observed during the enzymatic reaction – at least by HPLC-UV. It should be pointed out that rather than a smooth exponential decay, it appeared that the kinetics may be biphasic, with a fast initial consumption of MDA and concomitant formation of APRN, followed by a slower phase.

Our attempts to determine the kinetic parameters for the PrnC-catalyzed halogenation of MDA first utilized substrate concentrations of 20, 30, 40, 50, 60, 100 and 180 μM with a constant enzyme concentration of 3.46 μM. However, we encountered two practical difficulties, the first of which was alluded to above. First of all, we noticed that while product formation was initially linear in our assays, the rate of conversion slowed well ahead of full conversion (e.g. for 20 mM MDA and a 5 minutes reaction time, product formation was linear up to approximately 30% conversion and then dropped) suggesting enzyme inactivation, possibly by oxidation that could not be curtailed by catalase. While this behaviour still provided for linear product formation over the first 10% of reaction at low substrate concentrations, at the higher end of the assayed concentration range, the first 10% of reaction was not linear, precluding the determination of kinetic parameters. In an attempt to overcome this problem, we reduced the enzyme concentration.

Unfortunately, upon reducing the enzyme concentration, we observed significant reduction in observed rates, which we surmised was due to not enough $[E]_T$ or substrate inhibition (*vide infra*). Several assay conditions were then empirically surveyed before settling on those presented in Table 3.1, in which we were able to maintain substrate concentrations that were much greater than the enzyme concentration, and the observed reaction rates were always linear through the first 10% of the reaction. It should be noted that in order to do so, the enzyme concentration had to be varied from 1.8 μM to 7 μM, depending on substrate concentration.

The obtained initial rate for each MDA concentration is plotted in Figure 3.15. Each data point was repeated three times. Due to the relatively large error bars, it showed two possible ways fitting these data. Looking at the largest value for each data point, initial rate increased until [MDA] reached around 40 μM and the rate started to decrease as [MDA] was increasing until it was around 180 μM and flattened out. This kind of curve suggests substrate inhibition is occurring with PrnC. The kinetic parameters associated with fitting the data to the Michaelis-Menten equation (Eq. 3.2) are $k_{cat} = 0.08$ min^{-1} and $K_M = 23.6$ μM with errors of 0.0053 min^{-1} and 3.7 μM, respectively. The calculated reduced Chi^2 value for this fit was 5.8×10^{-7}. When the data were fit to the Michaelis-Menten equation incorporating substrate inhibition (Eq. 3.3), $k_{cat} = 0.06$ min^{-1},

K_M = 11.2 μM and K_i = 226.4 μM with errors of 0.0053 min^{-1}, 3.7 μM and 145.4 μM, respectively, and a reduced Chi^2 = 0.0077. Since the Chi^2 value for the latter fit is substantially larger, the kinetic parameters derived from the Michaelis-Menten fit are preferred. However, as we know for plotting the substrate inhibition, the initial rates for [MDA] before substrate inhibition begins and the initial rates for [MDA] within the substrate inhibition region need to be extensively studied, i.e more data points need to be collected so that sufficient information is provided for plotting a reasonable substrate inhibition plot. In our case, the initial rate at the region before substrate inhibition begins was the one for [MDA] = 20 μM only and an assumed [MDA] = 0. In our future studies, more data points will be collected in this region. However, as 10 μM MDA or less is a low concentration, shown on HPLC a small peak area close to the baseline. When trying to detect less than 10% conversions from HPLC, the tiny PA, along with the noise at the baseline, makes it is hard to integrate accurately. For M-M plot, although the errors were not as bad as the substrate inhibition ones, its reduced Chi^2 value indicated a not perfect fit. Similar situation as the substrate inhibition plot, M-M plot only included the first 4 data points including zero to generate the plot. Even though it predicted a K_M = 23.6 μM, it is not convincing because the trend of the first 4 data was pointing a continuously upwards direction. Since the initial rates at the saturation region of the plot has lower initial rates, they were excluded from the plot generation. And once again, more data points would help in this case and it will be included in our future studies for PrnC.

Comparing these kinetic parameters with those reported for PrnA (Table 3.2), which also exhibits kinetics complicated by substrate inhibition, PrnC has a comparable k_{cat}, but a K_M that differs by more than an order of magnitude. It means that PrnA requires a lot more substrate than PrnC to reach its maximum velocity. This makes sense evolutionarily because L-Trp is a natural abundant amino acid whereas MDA is only available after three enzymatic steps in a secondary metabolic pathway. RebH is a much faster halogenase compared to PrnA and PrnC, but it has a very small K_M. It means that RebH only requires a small amount of substrate to be saturated and the maximum velocity is reached at relatively low substrate concentrations,[140] or it is suggesting a potential mechanism for substrate inhibition.

Table 3.2 Comparison of the kinetic parameters (K_M in μM and k_{cat} in min^{-1}) determined for PrnC with those determined for the other kinetically-characterized flavin-dependent halogenases, PrnA and RebH.

	PrnC (M-M)	**PrnC (S-Inh)**	**PrnA[148]**	**RebH[140]**
K_M (μM)	24 ± 4	12 ± 9	160 ± 40	2
k_{cat} (min^{-1})	0.077 ± 0.005	0.061 ± 0.02	0.09 ± 0.03	1.4

As mentioned in section 3.1, PrnF,[102] a newly discovered enzyme expressed from a gene (*prnF*) that is located in close proximity to what was thought to be the complete *prn* operon, has been characterized as the flavin reductase component of PrnD, which catalyzes the unusual arylamine oxidation. It was found a larger $k_{\text{cat}} = 11.3\ \text{min}^{-1}$ for PrnD when PrnF was employed as the reductase, comparing to the case when SsuE was employed as a reductase ($k_{\text{cat}} = 6.8\ \text{min}^{-1}$). Because PrnA and PrnC are both enzymes from pyrrolnitrin synthetic pathway and require flavin reductase to function, it is interesting to see if they behave more efficiently in halogenations with PrnF as the flavin reductase.

It should be noted that it was noticed the fractions further purified by gel filtration had lower functional activity than the fractions that were pure straight off Ni-NTA column. Unfortunately, the PrnC we applied in these kinetic assays were the one needed to be further purified by gel filtration, hence the activity reported here is assumed to be lower than the PrnC with full activity. Thus performing kinetic studies with pure fractions of PrnC collected directly from N-NTA chromatography is also included in the future studies.

3.6 Conclusions and Outlook

The genes encoding PrnA and PrnC were successfully cloned and over-expressed in *E. coli* and the gene products were isolated and purified to homogeneity from the cell lysates. The activities of both PrnA and PrnC were reconstituted using the flavin reductase Fre from *E. coli.* The conversion of MDA to APRN by PrnC required the addition of catalase, which we suspect is necessary to prevent enzyme oxidation by flavin-derived oxidants. Our kinetic studies revealed that PrnC is inhibited by its substrate, MDA, and therefore a Michaelis-Menten analysis of the enzymatic reaction was complicated by this phenomenon. In order to further study the mechanism of PrnC-catalyzed halogenation of MDA, assays on a larger number of different concentrations of MDA need to be carried out. Furthermore, in order to accurately determine the activity of PrnA expressed in *E. coli* for comparison with PrnC, 7-Cl-Trp needs to be prepared for determining the response factors so that the amount of 7-Cl-Trp generated can be measured accurately. Since several other halogenases using L-Trp as substrate have demonstrated bromination activity, it is also interesting to investigate whether there is any bromination activity of PrnC, as well as PrnA. If there is, where on MDA or L-Trp the bromination occurs, whether or not there is still regioselectivity and what the activities are comparing to chlorination. Due to preliminary result showed PrnF reduces FAD to $FADH_2$ about 10 times faster than Fre, PrnF can be used instead of Fre to reduce the flavin necessary for PrnA or PrnC catalysis using NADH and FAD as co-factors.

References

[1] C. Leray. http://www.cyberlipid.org/perox/oxid0002.htm

[2] C. Engler, *Berichte der deutschen chemischen Gesellschaft* **1900**, *33*, 1090.

[3] E. H. Farmer, G. F. Bloomfield, A. Sundralingam, D. A. Sutton, *Transactions of the Faraday Society* **1942**, *38*, 0348.

[4] H. N. Stephen, *J Am Chem Soc* **1928**, *50*, 568.

[5] J. L. Bolland, *Quarterly Reviews, Chemical Society, 3,* 1.

[6] W. Lundberg, J. Chipault, M. Hendrickson, *Journal of the American Oil Chemists' Society* **1949**, *26*, 109.

[7] K. U. Ingold, *Science* **1967**, *158*, 248.

[8] K. U. Ingold, *Acc Chem Res* **1969**, *2*, 1.

[9] F. R. Mayo, *J. Am. Chem. Soc.* **1958**, *80*, 2497.

[10] F. R. Mayo, A. A. Miller, G. A. Russell, *ibid* **1958**, *80*, 2500.

[11] G. A. Russell, *J Am Chem Soc* **1957**, *79*, 2977.

[12] G. A. Russell, *Ange Chem Int Ed* **1957**, *69*, 688.

[13] M. Pierini, C. Punta, *Letters in Organic Chemistry* **2006**, *3*, 91.

[14] D. Voet, J. G. Voet, *Biochemistry*, 3rd ed., J. Wiley & Sons, Hoboken, NJ, **2004**.

[15] A. Nishikawa, R. Sodum, F.-L. Chung, *Lipids* **1992**, *27*, 54.

[16] J. Kanner, *Mol Nutr Food Res* **2007**, *51*, 1094.

[17] D. Harman, *J Gerontol* **1956**, *11*, 298.

[18] C. Behl, B. Moosmann, *Free Radic Biol Med* **2002**, *33*, 182.

[19] E. Maggi, R. Chiesa, G. Melissano, R. Castellano, D. Astore, A. Grossi, G. Finardi, G. Bellomo, *Arterioscler Thromb* **1994**, *14*, 1892.

[20] W. Palinski, V. A. Ord, A. S. Plump, J. L. Breslow, D. Steinberg, J. L. Witztum, *Arterioscler Thromb* **1994**, *14*, 605.

[21] D. P. Steinberg, *Lancet* **1995**, *346*, 36.

[22] E. Waddington, K. Sienuarine, I. Puddey, K. Croft, *Anal Biochem* **2001**, *292*, 234.

[23] J. R. McNamara, G. R. Warnick, G. R. Cooper, *Clin Chim Acta* **2006**, *369*, 158.

[24] N. A. Porter, *J. Am. Chem. Soc.* **1994**, *116*, 6690.

[25] N. A. Porter, B. A. Weber, H. Weenen, J. A. Khan, *J. Am. Chem. Soc* **1980**, *102*, 5597.

[26] Y. R. Luo, *Handbook of dissociation energies in organic compounds*, CRC press, **2003**.

[27] D. A. Pratt, J. H. Mills, N. A. Porter, *J. Am. Chem. Soc* **2003**, *125*, 5801.

[28] N. A. Porter, *Acc Chem Res* **1986**, *19*, 262.

[29] K. A. Tallman, C. L. Rector, N. A. Porter, *J. Am. Chem. Soc* **2009**, *131*, 5635.

[30] G. O. Schenk, O.-A. Neumuller, *Angew Chem* **1958**, *70*, 595.

[31] A. L. J. Beckwith, *J. Chem. Soc. Perkin. Trans. II* **1989**, *1989*, 10.

[32] S. L. Boyd, R. J. Boyd, L. R. C. Barclay, *J. Am. Chem. Soc* **1990**, *112*, 5724.

[33] S. L. Boyd, R. J. Boyd, Z. Shi, L. R. C. Barclay, N. A. Porter, *J. Am. Chem. Soc* **1993**, *115*, 687.

[34] W. E. Brill, *J. Chem. Soc. Perkin. Trans. II* **1984**, 621.

[35] N. A. Porter, J. S. Wujek, *J. Org. Chem.* **1987**, *52*.

[36] N. A. Porter, J. S. Wujek, *J Org Chem* **1990**, *52*, 5085.

[37] R. C. Murphy, K. M. Johnson, *J Biol Chem* **2008**, *283*, 15521.

[38] J. C. Walton, *Acc Chem Res* **1998**, *31*, 99.

[39] N. Porter, P. Zuraw, *J. Chem. Soc. Chem. Commun.* **1985**, *1985*, 2.
[40] J. R. Lowe, N. A. Porter, *J. Am. Chem. Soc* **1997**, *119*, 11534.
[41] N. A. Porter, J. S. Wujek, *J Org Chem* **1987**, *52*, 5085.
[42] N. A. Porter, J. K. Kaplan, P. H. Dussault, *J. Am. Chem. Soc* **2002**, *112*, 1266.
[43] S. Olivella, A. Sole, *J Am Chem Soc* **2003**, *125*, 10641.
[44] K. J. Laidler, *Chemical Kinetics*, 3rd ed. ed., Harper and Row, New York, **1987**.
[45] J. A. Howard, *Adv. Free Radical Chem.* **1972**, *4*, 49.
[46] N. A. Porter, D. G. Wujek, *J. Am. Chem. Soc.* **1984**, *106*, 2626.
[47] K. A. Tallman, D. A. Pratt, N. A. Porter, *J Am Chem Soc* **2001**, *123*, 11827.
[48] M. J. Pellerite, R. L. Jackson, J. I. Brauman, *J Phys Chem* **1981**, *85*, 1624.
[49] R. Zils, S. Inomata, T. Imamura, A. Miyoshi, N. Washida, *J Phys Chem A* **2001**, *105*, 1277.
[50] J. M. Mayer, D. A. Hrovat, J. L. Thomas, W. T. Borden, *J Am Chem Soc* **2002**, *124*, 11142.
[51] V. Vaidya, K. U. Ingold, D. A. Pratt, *Angew Chem* **2008**, *121*, 163.
[52] P. J. O'Malley, *Biochim Biophys Acta* **2002**, *1553*, 212.
[53] W. M. Fox, *J. Chem. Soc.* **1966**, 1503.
[54] M. C. R. Symons, *J. Chem. Soc.* **1965**, 2276.
[55] P. E. M. Siegbahn, L. Eriksson, F. Himo, M. Pavlov, *J. Phys. Chem. B* **1998**, *102*, 10622.
[56] C. A. Morgan, M. J. Pilling, J. M. Tulloch, R. P. Ruiz, K. D. Bayes, *J. Chem. Soc. Faraday Trans. 2* **1982**, *78*, 1323.
[57] J. A. Blake, D. A. Pratt, S. Lin, J. C. Walton, P. Mulder, K. U. Ingold, *J Org Chem* **2004**, *69*, 3112.
[58] M. I. de Heer, P. Mulder, H.-G. Korth, K. U. Ingold, J. Lusztyk, *J Am Chem Soc* **2000**, *122*, 2355.
[59] M. Lucarini, G. F. Pedulli, L. Valgimigli, *J Org Chem* **1996**, *61*, 4309.
[60] G. E. Davico, V. M. Bierbaum, C. H. DePuy, G. B. Ellison, R. R. Squires, *J Am Chem Soc* **1995**, *117*, 2590.
[61] D. A. Pratt, G. A. DiLabio, G. Brigati, G. F. Pedulli, L. Valgimigli, *J Am Chem Soc* **2001**, *123*, 4625.
[62] M. Wijtmans, D. A. Pratt, J. Brinkhorst, R. Serwa, L. Valgimigli, G. F. Pedulli, N. A. Porter, *J Org Chem* **2004**, *69*, 9215.
[63] M. Wijtmans, D. A. Pratt, L. Valgimigli, G. A. DiLabio, G. F. Pedulli, N. A. Porter, *Angew Chem Int Ed Engl* **2003**, *42*, 4370.
[64] T.-g. Nam, C. L. Rector, H.-y. Kim, A. F. P. Sonnen, R. Meyer, W. M. Nau, J. Atkinson, J. Rintoul, D. A. Pratt, N. A. Porter, *J Am Chem Soc* **2007**, *129*, 10211.
[65] S. J. Nara, M. Jha, J. Brinkhorst, T. J. Zemanek, D. A. Pratt, *J Org Chem* **2008**.
[66] M. Sjodin, S. Styring, B. Akermark, L. Sun, L. Hammarstrom, *J Am Chem Soc* **2000**, *122*, 3932.
[67] P. E. M. Siegbahn, M. R. A. Blomberg, R. H. Crabtree, *Theor Chem Acc* **1997**, *97*, 289.
[68] P. E. M. Siegbahn, L. Eriksson, F. Himo, M. Pavlov, *J Phys Chem B* **1998**, *102*, 10622.
[69] K. A. Campbell, J. M. Peloquin, B. A. Diner, X.-S. Tang, D. A. Chisholm, R. D. Britt, *J Am Chem Soc* **1997**, *119*, 4787.
[70] T. Maki, Y. Araki, Y. Ishida, O. Onomura, Y. Matsumura, *J Am Chem Soc* **2001**, *123*, 3371.
[71] P. J. O'Malley, *J Am Chem Soc* **1998**, *120*, 11732.

[72] D. A. Proshlyakov, M. A. Pressler, C. DeMaso, J. F. Leykam, D. L. DeWitt, G. T. Babcock, *Science* **2000**, *290*, 1588.
[73] C. Tommos, G. T. Babcock, *Acc Chem Res* **1998**, *31*, 18.
[74] G. W. Burton, K. U. Ingold, *Acc Chem Res* **1986**, *19*, 194.
[75] G. Litwinienko, K. U. Ingold, *Acc Chem Res* **2007**, *40*, 222.
[76] N. Singh, P. J. O'Malley, P. L. Popelier, *Phys Chem Chem Phys* **2005**, *7*, 614.
[77] G. A. DiLabio, E. R. Johnson, *J Am Chem Soc* **2007**, *129*, 6199.
[78] G. Litwinienko, K. U. Ingold, *J Org Chem* **2003**, *68*, 3433.
[79] M. Jha, D. A. Pratt, *Chem Commun (Camb)* **2008**, 1252.
[80] P. A. MacFaul, K. U. Ingold, J. Lusztyk, *J Org Chem* **1996**, *61*, 1316.
[81] D. W. Snelgrove, J. Lusztyk, J. T. Banks, P. Mulder, K. U. Ingold, *J Am Chem Soc* **2001**, *123*, 469.
[82] L. Valgimigli, J. T. Banks, K. U. Ingold, J. Lusztyk, *J. Am. Chem. Soc.* **1995**, *117*, 9966.
[83] V. Luca, A. Riccardo, P. Silvia, P. Gian Franco, H. Di, J. H. Jason , A. P. Derek *Angew Chem* **2009**, *121*, 8498.
[84] D. V. Avila, C. E. Brown, K. U. Ingold, J. Lusztyk, *J. Am. Chem. Soc.* **1993**, *115*.
[85] D. V. Avila, K. U. Ingold, J. Lusztyk, W. H. Green, D. R. Procopio, *J. Am. Chem. Soc.* **1995**, *117*, 2929.
[86] J. H. B. Chenier, E. Furimsky, J. A. Howard, *Can. J. Chem.* **1974**, *52*, 3682.
[87] M. Lingwood, J. R. Hammond, D. A. Hrovat, J. M. Mayer, W. T. Borden, *J Chem Theory Comput* **2006**, *2*, 740.
[88] M. Lucarini, V. Mugnaini, G. F. Pedulli, *J Org Chem* **2002**, *67*, 928.
[89] K. Arima, H. Imanaka, M. Kousaka, A. Fukuda, G. Tamura, *Agric. Biol. Chem.* **1964**, *28*, 575.
[90] R. P. Elander, J. A. Mabe, R. H. Hamill, M. Gorman, *Appl Microbiol* **1968**, *16*, 753.
[91] M. Nose, K. Arima, *J. Antibiotic (Tokyo) Ser.* **1969**, *22*, 135.
[92] Y. Homma, Z. Sato, F. Hirayama, K. Konno, H. Shirahama, T. Suzui, *Soil. Biol. Biochem.* **1989**, *21*, 723.
[93] C. R. Howell, R. D. Stipanovic, *Phytophathology* **1979**, *77*, 480.
[94] W. J. Janisiewicz, J. Roitman, *Phytophathology* **1988**, *78*, 1697.
[95] S. Kirner, P. E. Hammer, D. S. Hill, A. Altmann, I. Fischer, L. J. Weislo, M. Lanahan, K. H. van Pee, J. M. Ligon, *J Bacteriol* **1998**, *180*, 1939.
[96] C. J. Chang, H. G. Floss, D. J. Hook, J. A. Mabe, P. E. Manni, L. L. Martin, K. Schroder, T. L. Shieh, *J Antibiot (Tokyo)* **1981**, *34*, 555.
[97] R. Hamill, R. Elander, J. Mabe, M. Gorman, *Antimicrob Agents Chemother (Bethesda)* **1967**, *7*, 388.
[98] R. L. Hamill, R. P. Elander, J. A. Mabe, M. Gorman, *Appl Microbiol* **1970**, *19*, 721.
[99] D. H. Lively, M. Gorman, M. E. Haney, J. A. Mabe, *Agents Chemother.* **1966**, *1966*, 462.
[100] P. Zhou, U. Mocek, B. Siesel, H. G. Floss, *J Basic Microbiol* **1992**, *32*, 209.
[101] L. L. Martin, C. J. Chang, H. G. Floss, J. A. Mabe, E. W. Hagaman, E. Wenkert, *J AM Chem Soc***2002**, *94*, 8942.
[102] J. K. Lee, H. Zhao, *J Bacteriol* **2007**, *189*, 8556.
[103] M. D. Morrison, J. J. Hanthorn, D. A. Pratt, *Org Lett* **2009**, *11*, 1051.
[104] F. H. Vaillancourt, E. Yeh, D. A. Vosburg, S. Garneau-Tsodikova, C. T. Walsh, *Cheml Rev* **2006**, *106*, 3364.
[105] G. W. Gribble, *J. Chem. Educ.* **2004**, *81*, 1441.

[106] D. Kahne, C. Leimkuhler, W. Lu, C. Walsh, *Chem Rev* **2005**, *105*, 425.
[107] M. Piraee, R. L. White, L. C. Vining, *Microbiology* **2004**, *150*, 85.
[108] M. J. Ryan, J. A. Lotvin, N. Strathy, S. E. Fantini, *U.S.Patent No. 5,866,410, 1999*.
[109] C. Sanchez, I. A. Butovich, A. F. Brana, J. Rohr, C. Mendez, J. A. Salas, *Chem Biol* **2002**, *9*, 519.
[110] B. Nowak-Thompson, N. Chaney, J. S. Wing, S. J. Gould, J. E. Loper, *J Bacteriol* **1999**, *181*, 2166.
[111] C. Dong, F. Huang, H. Deng, C. Schaffrath, J. B. Spencer, D. O'Hagan, J. H. Naismith, *Nature* **2004**, *427*, 561.
[112] H. Deng, S. L. Cobb, A. R. McEwan, R. P. McGlinchey, J. H. Naismith, D. O'Hagan, D. A. Robinson, J. B. Spencer, *Angew Chem Int Ed Engl* **2006**, *45*, 759.
[113] M. Sundaramoorthy, J. Terner, T. L. Poulos, *Chem Biol* **1998**, *5*, 461.
[114] L. P. Hager, D. R. Morris, F. S. Brown, H. Eberwein, *J Biol Chem* **1966**, *241*, 1769.
[115] D. R. Morris, L. P. Hager, *J Biol Chem* **1966**, *241*, 1763.
[116] A. Taurog, E. M. Howells, *J Biol Chem* **1966**, *241*, 1329.
[117] K. H. van Pee, E. P. Patallo, *Appl Microbiol Biotechnol* **2006**, *70*, 631.
[118] A. Butler, J. N. Carter-Franklin, *Nat Prod Rep* **2004**, *21*, 180.
[119] W. Wiesner, K. H. van Pee, F. Lingens, *FEBS Lett* **1986**, *209*, 321.
[120] W. Burd, O. Yourkevich, A. J. Voskoboev, K. H. van Pee, *FEMS Microbiol Lett* **1995**, *129*, 255.
[121] K. H. van Pee, *Annu Rev Microbiol* **1996**, *50*, 375.
[122] M. Weng, O. Pfeifer, S. Krauss, F. Lingens, K. H. van Pee, *J Gen Microbiol* **1991**, *137*, 2539.
[123] N. Itoh, Y. Izumi, H. Yamada, *J Biol Chem* **1987**, *262*, 11982.
[124] T. Dairi, T. Nakano, K. Aisaka, R. Katsumata, M. Hasegawa, *Biosci Biotechnol Biochem* **1995**, *59*, 1099.
[125] T. W. Yu, L. Bai, D. Clade, D. Hoffmann, S. Toelzer, K. Q. Trinh, J. Xu, S. J. Moss, E. Leistner, H. G. Floss, *Proc Natl Acad Sci U S A* **2002**, *99*, 7968.
[126] A. Messerschmidt, R. Wever, *Proc Natl Acad Sci U S A* **1996**, *93*, 392.
[127] Z. Chang, P. Flatt, W. H. Gerwick, V. A. Nguyen, C. L. Willis, D. H. Sherman, *Gene* **2002**, *296*, 235.
[128] J. P. Jones, K. R. Korzekwa, A. E. Rettie, W. F. Trager, *J Am Chem Soc* **2002**, *108*, 7074.
[129] R. P. Hausinger, *Crit Rev Biochem Mol Biol* **2004**, *39*, 21.
[130] K. D. Koehntop, J. P. Emerson, L. Que, *J Biol Inorg Chem* **2005**, *10*, 87.
[131] E. Guenzi, G. Galli, I. Grgurina, E. Pace, P. Ferranti, G. Grandi, *J Biol Chem* **1998**, *273*, 14403.
[132] J. H. Zhang, N. B. Quigley, D. C. Gross, *Appl Environ Microbiol* **1997**, *63*, 2771.
[133] S. A. Sieber, J. Tao, C. T. Walsh, M. A. Marahiel, *Angew Chem Int Ed Engl* **2004**, *43*, 493.
[134] L. C. Blasiak, F. H. Vaillancourt, C. T. Walsh, C. L. Drennan, *Nature* **2006**, *440*, 368.
[135] S. Keller, T. Wage, K. Hohaus, M. Holzer, E. Eichhorn, K. H. van Pee, *Angew Chem Int Ed Engl* **2000**, *39*, 2300.
[136] E. Yeh, S. Garneau, C. T. Walsh, *Proc Natl Acad Sci U S A* **2005**, *102*, 3960.
[137] S. Lin, S. G. Van Lanen, B. Shen, *J Am Chem Soc* **2007**, *129*, 12432.

[138] C. Seibold, H. Schnerr, J. Rumpf, A. Kunzendorf, C. Hatscher, T. Wage, A. J. Ernyei, C. Dong, J. H. Naismith, K.-H. Van PÃ©e, *Biocatalysis and Biotransformation* **2006**, *24*, 401
[139] S. Zehner, A. Kotzsch, B. Bister, R. D. Sussmuth, C. Mendez, J. A. Salas, K. H. van Pee, *Chem Biol* **2005**, *12*, 445.
[140] E. Yeh, L. J. Cole, E. W. Barr, J. M. Bollinger, Jr., D. P. Ballou, C. T. Walsh, *Biochemistry* **2006**, *45*, 7904.
[141] B. Galan, E. Diaz, M. A. Prieto, J. L. Garcia, *J Bacteriol* **2000**, *182*, 627.
[142] K. Otto, K. Hofstetter, M. Rothlisberger, B. Witholt, A. Schmid, *J Bacteriol* **2004**, *186*, 5292.
[143] D. Thibaut, N. Ratet, D. Bisch, D. Faucher, L. Debussche, F. Blanche, *J Bacteriol* **1995**, *177*, 5199.
[144] J. Valton, L. Filisetti, M. Fontecave, V. Niviere, *J Biol Chem* **2004**, *279*, 44362.
[145] V. Massey, *J Biol Chem* **1994**, *269*, 22459.
[146] C. Bergt, X. Fu, N. P. Huq, J. Kao, J. W. Heinecke, *J Biol Chem* **2004**, *279*, 7856.
[147] D. I. Pattison, M. J. Davies, *Biochemistry* **2005**, *44*, 7378.
[148] C. Dong, S. Flecks, S. Unversucht, C. Haupt, K. H. van Pee, J. H. Naismith, *Science* **2005**, *309*, 2216.
[149] E. Yeh, L. C. Blasiak, A. Koglin, C. L. Drennan, C. T. Walsh, *Biochemistry* **2007**, *46*, 1284.
[150] M. Fontecave, R. Eliasson, P. Reichard, *J Biol Chem* **1987**, *262*, 12325.
[151] M. Fontecave, R. Eliasson, P. Reichard, *J Biol Chem* **1989**, *264*, 9164.
[152] M. Fontecave, A. Graslund, P. Reichard, *J Biol Chem* **1987**, *262*, 12332.
[153] T. Nishizawa, C. C. Aldrich, D. H. Sherman, *J Bacteriol* **2005**, *187*, 2084.
[154] F. Baneyx, M. Mujacic, *Nat Biotechnol* **2004**, *22*, 1399.
[155] P. E. Hammer, D. S. Hill, S. T. Lam, K. H. Van Pee, J. M. Ligon, *Appl Environ Microbiol* **1997**, *63*, 2147.
[156] C. Dong, A. Kotzsch, M. Dorward, K. H. van Pee, J. H. Naismith, *Acta Crystallogr D Biol Crystallogr* **2004**, *60*, 1438.